Helsinki University of Technology Laboratory of Computational Engineering
Teknillisen korkeakoulun Laskennallisen tekniikan laboratorion julkaisuja
Espoo 2006 REPORT B58

MOLECULAR MODELING OF CHARGED MEMBRANE SYSTEMS

Wei Zhao

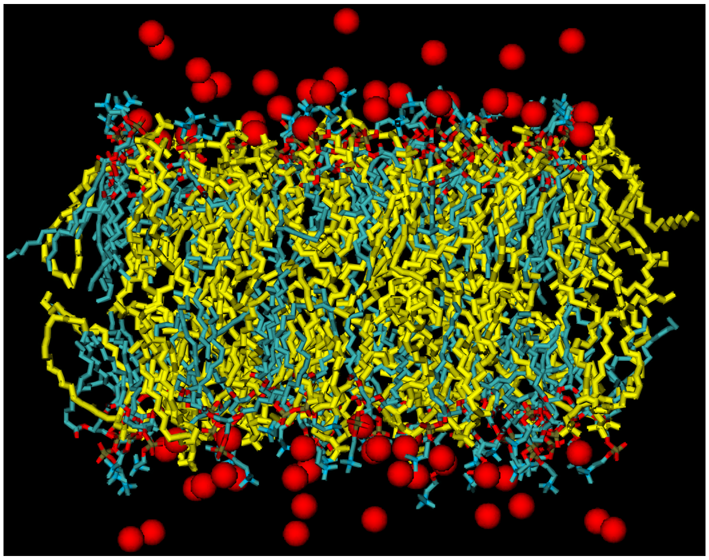

TEKNILLINEN KORKEAKOULU
TEKNISKA HÖGSKOLAN
HELSINKI UNIVERSITY OF TECHNOLOGY
TECHNISCHE UNIVERSITÄT HELSINKI
UNIVERSITE DE TECHNOLOGIE D'HELSINKI

Helsinki University of Technology
Laboratory of Computational Engineering
Espoo 2006 REPORT B58

Molecular modeling of charged membrane systems

Wei Zhao

Dissertation for the degree of Doctor of Science in Technology to be presented with due permission of the Department of Electrical and Communications Engineering, Helsinki University of Technology, for public examination and debate in Auditorium S4 at Helsinki University of Technology (Espoo, Finland) on the 11th of November, 2006, at 12 o'clock noon.

Helsinki University of Technology
Department of Electrical and Communications Engineering
Laboratory of Computational Engineering

Teknillinen korkeakoulu
Sähkö- ja tietoliikennetekniikan osasto
Laskennallisen tekniikan laboratorio

Distribution:
Helsinki University of Technology
Laboratory of Computational Engineering
P. O. Box 9203
FI-02015 TKK
FINLAND
Tel. +358-9-451 4826
Fax. +358-9-451 4830
`http://www.lce.hut.fi/`

Online in PDF format: `http://lib.tkk.fi/Diss/2006/isbn9512284669/`

E-mail: `zhaowei@lce.hut.fi`

ISBN 951-22-8465-0 (printed)
ISBN 978-951-22-8465-8 (printed)
ISBN 951-22-8466-9 (PDF)
ISBN 978-951-22-8466-5 (PDF)
ISSN 1455-0474
PicaSet Oy
Espoo 2006

Abstract

We have performed molecular modeling of membrane systems by employing the classical molecular dynamics method and force field parameterizations. In this thesis, our main interest is on the structural and dynamic properties of charged model membrane systems. This thesis consists of four related projects.

The first project focuses on cationic DMPC (dimyristoylphosphatidylcholine) / DOTAP (dimyristoyltrimethylammonium propane) lipid bilayers in the presence of chloride ions. We study the electrostatic interactions involving the dipolar headgroups of DMPC, the cationic headgroups of DOTAP, anionic counterions, and water molecules in the hydration zone of the membranes. We also investigate the effects of longer and unsaturated hydrocarbon chains of DOTAP on the structural properties of the mixed DMPC/DOTAP bilayers.

In the second project, we consider an anionic POPG (palmitoyloleolyphosphatidylglycerol) lipid bilayer in the presence of sodium ions as counterions. We study the electrostatic interactions between the sodium ions and different groups in POPG molecules. We find that the sodium ions tend to bind strongly to the carbonyl oxygens instead of the phosphodiester oxygens. This kind of binding results in the formation of extensive lipid clusters, in which the lipids are bridged via sodium ions. The hydrogen bonds are also investigated as well as other properties such as the ordering of water molecules near the lipid bilayer.

Then, using the POPG model developed in the previous study, we have investigated a bacterial model membrane consisting of 75% zwitterionic POPE (palmitoyloleolyphosphatidylethanolamine) and 25% anionic POPG. The intra- and inter-molecular hydrogen bonds between the POPE and POPG molecules are analyzed and compared to separate simulations of pure POPE and pure POPG bilayers. We find that the hydrogen bonds contribute considerably to the interfacial properties of the mixed POPE/POPG bilayer. Another important observation is the formation of ion-lipid bridges and lipid clusters, which have not been found in other studies. We propose that as possible mechanism how bacteria may be able to control their permeability against solvents.

In the fourth project we study the dynamic behavior of water molecules in the vicinity of different lipid bilayer surfaces. In this work, we have analyzed the interface effects of three different lipid bilayers – POPC, POPE, and POPG on water dynamics.

Preface

This thesis for the degree of Doctor of Technology has been prepared in the Laboratory of Computational Engineering in Helsinki University of Technology during the years 2001-2006. I would like to thank Prof. Mikko Karttunen for his excellent supervision. During my PhD studies, Mikko has been teaching me not only the art of computational biophysics, but also the secrets of scientific writing as well as generating attractive applications. More importantly, he has taught me the importance of diligence and integrity in becoming an outstanding scientist by being such a model himself. I also thank Prof. Kimmo Kaski for his funding for my PhD study, and his efforts in providing excellent computing resources. Kimmo has also shown his leadership in creating a highly active and international research environment in our laboratory of which I have benefited a lot.

I also wish to thank all the co-authors of the publications related to this thesis. Many thanks belong to Prof. Ilpo Vattulainen, Dr. Andrey Gurtovenko, and Dr. Krzysztof Murzyn for fruitful discussions and effective collaborations. I also wish to thank Prof. Tapio Ala-Nissila for his advice and interesting statistical mechanics lectures. Special thanks also belong to my thesis pre-examiners, Prof. Mikko P. Haataja and Prof. Apichart Linhananta, for their excellent suggestions and comments. I thank the Finnish Academy of Science and Letters and Helsinki Institute of Physics for financial support.

I have been fortunate to meet many nice and interesting people during these years. I want to thank Tomasz Róg, Lorna Stimson, Petri Nikunen, Markus Miettinen, Riku Linna, and Lei Dong for being good friends and for providing advice for my research. In particular, Tomek has also been an invaluable collaborator in my research projects. Michael Patra and Marco Patriarca have given me a plenty of help on computational problems and mathematics. I also thank Emma Terämä for being good friend and generous host. Special thanks also belong to Eeva Lampinen and Kaija Virolainen for their kind help with my study and life in Finland.

Finally, I thank all of my family members for their support and understanding. Last but not the least, I would like to thank my wife Xin Xin for her support, patience, and love all through these years.

Contents

Author's research contribution

This thesis is a monograph and thus the work has been solely done by the author. The author has played an active role in all the research projects reported in this thesis, which has been split into the following four publications:

I W. Zhao, T. Róg, A. Gurtovenko, I. Vattulainen, and M. Karttunen, *Atomic-scale structure and electrostatics of anionic POPG lipid bilayers with* Na^+ *counterions*, Biophys. J., in press.

II W. Zhao, T. Róg, A. Gurtovenko, I. Vattulainen, and M. Karttunen, *Role of Phosphatidylglycerols in the Stability of Bacterial Membranes*, submitted to Biochim. Biophys. Acta.

III W. Zhao, A. Gurtovenko, I. Vattulainen, and M. Karttunen, *Molecular dynamics study of cationic DMPC/DOTAP lipid bilayers: Interfacial properties and the effect of chain length and unsaturation*, to be submitted to J. Phys. Chem. B in Nov 2006.

IV K. Murzyn, W. Zhao, M. Karttunen, M. Kurdziel, and T. Róg, *Dynamics of Water at Membrane Surfaces: Effect of Headgroup Structure*, Biointerphases, in press.

In these publications, the author has been involved in planning the research projects, developing model systems and force field parameters, and performing computer simulations. The author has also written the first drafts for publications I-III, based on data analysis and interpreting the results. He also actively participated the writing of publication IV.

List of Abbreviations

AMBER	Assisted Model Building with Energy Refinement
AVACF	Angular Velocity-Autocorrelation Function
CHARMM	Chemistry at HARvard Molecular Mechanics
DMPC	dimyristoylphosphatidylcholine
DMTAP	dimyristoyltrimethylammonium propane
DNA	deoxyribonucleic acid
DOTAP	dioleoyloxytrimethylammonium propane
DPD	dissipative particle dynamics
DPPC	dipalmitoylphosphatidylcholine
GROMACS	GROningen MAachine for Chemical Simulations
GROMOS	GROningen Molecular Simulation
FFT	Fast Fourier Transformation
fs	femto-second
LINCS	LINear Constraint Solver (for molecular simulations)
MC	Monte Carlo
MD	Molecular Dynamics
MRSA	Methicillin-Resistant *Staphylococcus Aureus*
MSD	Mean Square Displacement
NCC	Nieser, Corongiu, and Clementi water model
nm	nano-meter
NMR	Nuclear Magnetic Resonance
NPT	systems of constant particle Number, Pressure and Temperature
ns	nano-second
NVT	systems of constant particle Number, Volume and Temperature
OPLS	Optimized Potentials for Liquid Simulations
P^3M	Particle-Particle Particle-Mesh
PC	phosphatidylcholine
PE	phosphatidylethanolamine
PG	phosphatidylglycerol
PME	Particle Mesh Ewald

POPC	palmitoyloleolyphosphatidylcholine
POPE	palmitoyloleolyphosphatidylethanolamine
POPG	palmitoyloleolyphosphatidylglycerol
PPC	Polarizable Point Charge
ps	pico-second
PS	phosphatidylserine
QM	Quantum Mechanics
RCF	Reorientational Correlation Function
RDF	Radial Distribution Function
RNA	Ribonucleic Acid
SETTLE	an analytic version of SHAKE (see below)
SHAKE	a method for constraining motion
SPC	Simple Point Charge
SPC/E	Simple Point Charge - Extended
ST2	a water model based on the revised pair potential
TAP	trimethylammonium propane
TIP3P	a 3-Point water model based on Transferable Intermolecular Potential
TIP4P	a 4-Point water model based on Transferable Intermolecular Potential
TIP5P	a 5-Point water model based on Transferable Intermolecular Potential
TRC	Twin-Range Cutoff
VACF	Velocity-Autocorrelation Function

Chapter 1

Introduction

1.1 Membranes: nature's most important structures?

Cells are the structural and functional units of all living organisms found in nature. The smallest organisms such as bacteria consist of single cells while larger organisms are multicellular and composed of different number of cells that have a complex organization. In general, cells can be divided into two general categories: eukaryotes (see Fig. 1.1) and prokaryotes (see Fig. 1.2) depending on whether the nucleus of the cell is enveloped by a double-membrane shell [1]. In nature, there is a great variety of cells varying in size, shape, and biological functions. Despite this variation, cells share many common structural features that have been revealed by extensive theoretical and experimental studies [3–9]. The plasma membrane (see Fig. 1.1) defines the periphery of the cell, serving as a barrier that separates the contents of the cell from its surroundings. The basic structure of the plasma membrane is a flexible lipid bilayer (see Fig. 1.1) in which proteins of differing biological function, such as transporters, receptors, and enzymes, are embedded dynamically (see Fig. 1.3). Inside the cell is the cytoplasm where the cytosol provides an aqueous environment dissolving biomolecules such as enzymes, messenger RNA, amino acids, nucleotides and metabolites. Furthermore, almost all non-bacterial cells contain a variety of membrane-bound organelles. These can include, in animal cells, *nucleus*, *endoplasmic reticulum*, *Golgi complexes*, *lysosomes* and *mitochondria* (see Fig. 1.1). Next, let us briefly discuss some of these membrane-enclosed organelles.

The nucleus is an organelle in which the genome is stored and replicated. Surrounding the nucleus is the rough endoplasmic reticulum. The synthesis of proteins are performed by thousands of ribosomes that are attached to the

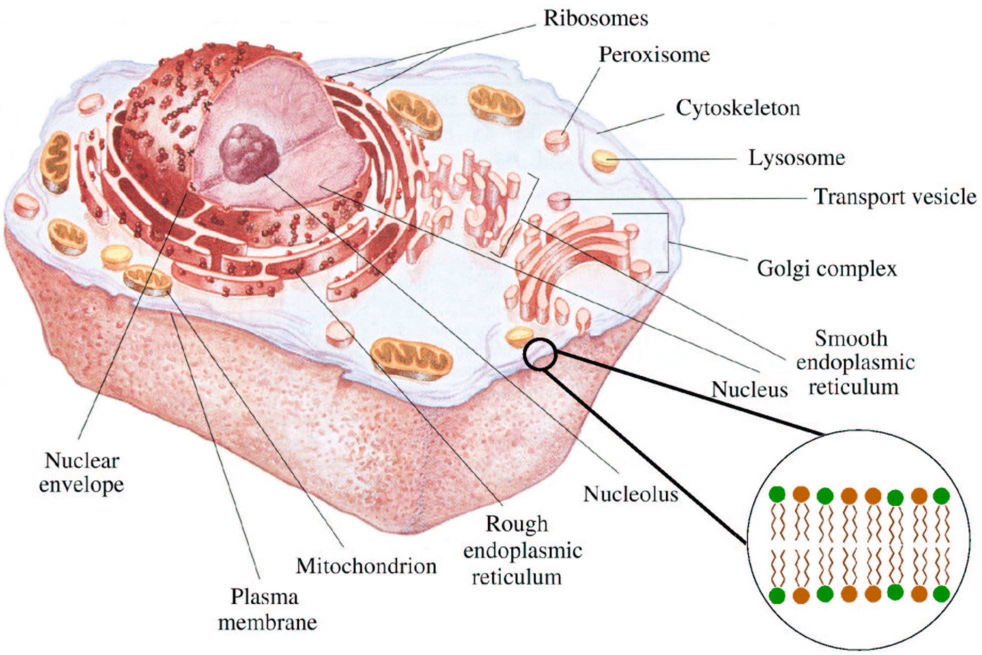

Figure 1.1: Schematic illustration of an animal cell containing various organelles, all of which are surrounded by different biomembranes. The figure is taken from Ref. [2]

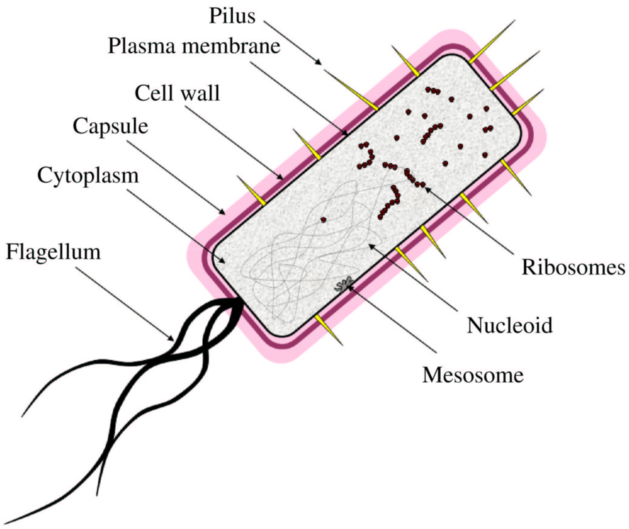

Figure 1.2: An illustration of a prokaryotic cell (bacteria), in which the nucleoid (DNA) is not confined in a specific region like in an eukaryotic cell (see Fig. 1.1). The figure is taken from website of Flu Wiki company (http://www.fluwikie.com).

rough endoplasmic reticulum. Smooth endoplasmic reticulum is physically continuous with the rough endoplasmic reticulum and is responsible for the synthesis of lipids and other important processes.

The Golgi complex is an asymmetric, structural and functional organelle whose *cis* side faces the rough endoplasmic reticulum. The proteins from the rough endoplasmic reticulum are transported by membrane vesicles to the Golgi complex, fusing with the *cis* side and being modified by the enzymes within the Golgi complex. One of the functions of this modification of newly synthesized proteins is to address them to their specific destinations as they are transported from the Golgi complex in a vesicle budding from the *trans* side.

Lysosomes, spherical vesicles bounded by a single membrane bilayer, are the sites where degradative processes take place. They serve as cellular recycling centers. There, the materials inside the cytosol or those brought into the cell by endocytosis enter the lysosome selectively by fusion of the lysosomal membrane, and are degraded to simpler molecules and released into new cellular components or further catalyzed.

The energy needed by all of the above organelles is provided by mitochondria, which generates adenosine triphosphate (ATP), the major energy-carrying molecule in cells [10]. Each mitochondria has two membranes. The smooth outer membrane which provides the integrity of mitochondria while the inner membrane has many foldings that give it a large surface area which is related to its energy-yielding metabolism.

The plasma membrane and other membrane-enclosed organelles within a cell are generally called biomembranes, referred to as membranes in the following. From the above brief description of cells, we can see that membranes play essential roles in almost all biological processes and structures in cells. Membranes not only define the boundaries of cells and divide the volume into discrete functional compartments but also regulate the molecular traffic across the boundaries as well as other communications between cells and organelles [8]. Membranes have remarkable physical properties of being flexible, self-sealing, and selectively permeable to specific polar solutes [2, 11]. Their flexibility permits shape changes essential to cellular processes such as cell growth. Also, due to their ability to rupture and reseal without inducing gross leaks, two membrane systems can fuse, as in exocytosis, and a membrane system can be formed through budding from another one, as in endocytosis and cell division.

The selective permeability of membranes guarantees that certain compounds and ions can be retained within cells or specific membrane-enclosed organelles while other species are excluded [12]. Furthermore, membranes are not just passive barriers and define the peripheries but also actively take part in various cellular processes due to the proteins embedded within membranes through hydrophobic interactions. For example, anesthetics are suggested to interact with membrane and therefore affect the activity of membrane proteins which is sensitive to their lipid environment [13]. Transporters and ion channels [7, 8] move organic species and inorganic ions across membranes. Receptors sense external signals and thereafter induce molecular changes in the cell. Membranes also organize many cellular processes such as the synthesis of lipids and certain proteins, the energy transduction in mitochondria and chloroplasts, and the cellular self-destruction (apoptosis) [14].

From above description, we can see that membranes are crucial to the life of cells. In the following section, we will review briefly the history of studies of membrane structure.

1.2 Historical background

The name "cell" is due to Robert Hooke as he named the small compartments he observed in cork tissue in 1665 [15]. In 1855, Carl Nägeli realized the existence of semipermeable layer around plant cells and then called it the plasma membrane. Between 1895 and 1902, Ernest Overton managed to measure cell membrane permeability for many compounds and found a relationship between the ability of these compounds to penetrate through membranes and their solubility in lipids. He then proposed that it is the lipids that form the thin film of membrane through which substances from surrounding solution pass to cells. This observation led to the famous *Meyer-Overton rule* which states that the permeability of molecules through cell is governed by their solubility.

In 1917, Irving Langmuir found that a monolayer film of fatty acids could be formed at an air-water interface, in a *Langmuir trough*, with the hydrophilic carboxylic acid groups pointing to water and hydrophobic methyl tails oriented to the air. The benchmark experiment started the research of Langmuir-Blodgett monolayer systems, which have been used extensively in many fields.

In 1925, Evert Gorter and F. Grendel[1] performed their famous experiment in which they extracted lipids from erythrocyte membranes with acetone and dispersed the sample in water in a Langmuir trough so as to form a thin layer at the surface of water. Then a thin thread was drawn across the surface to compress the lipid molecules at the air-water interface to form a lipid monolayer. In the measurement, the area of the lipid monolayer was

---

[1] F. Grendel was Evert Gorter's research assistant. For some reason, his first name seems not to be documented in publications or research records

found to be two times larger than the computed area of the erythrocytes from which the lipids were extracted. Based on this observation, Gorter and Grendel proposed that lipids in the erythrocyte membrane are arranged in the form of a bimolecular leaflet, or a lipid bilayer.

The structure of biomembranes was further elaborated in 1935 by James Danielli and Hugh Davson in the *Davson-Danielli* or "paucimolecular" model, in which it was postulated that the surfaces of the lipid bilayer were coated by proteins. The Davson-Danielli model was a remarkably successful model, which was supported by extensive experiments, such as observations from electron microscopy [12]. However, although it could explain the organization of the lipids, it could not account for numerous properties of membrane proteins.

The rapid development leading to our current view of membranes has largely been due to the progress in new experimental techniques that are used to characterize the structure of membranes and membrane proteins. For example, it was revealed by freeze-fracture electron microscopy that globular proteins are embedded within membranes [16, 17]. Spectroscopic evidence also indicated that membrane proteins have an appreciable amount of α-helix and they are likely to be globular rather than spread out in a monolayer on the lipid bilayer surface as suggested by the *Robertson's unit membrane* model [18], which is a modified version of the Davson-Danielli model and based on observations from electron microscopy. The non-polar characteristics of membrane proteins also indicated that membrane proteins interact with membrane lipids via hydrophobic forces. The studies done by David Frye and Michael Edidin, in 1970, suggested the fluid nature of biomembranes through examining of the dynamics of both mouse and human surface antigens by indirect fluorescent antibody method [19].

Based on the above experimental observation as well as a variety of biomembrane models, in 1972 S. Jonathan Singer and Garth L. Nicolson proposed the famous fluid mosaic model [3], which describes the membrane as a fluid-like lipid bilayer in which embedded globular proteins diffuse freely. The fluid mosaic model proved to be a very useful hypothesis in explaining many phenomena taking place in biomembranes such as the rapid diffusion of protein measured by Frye. This model implies that the lipid bilayer component of cell membranes is a structureless fluid characterized by disorder and randomness in which proteins can float freely. The fluid mosaic model is a remarkably successful model, which still gives insight into the structural and dynamic properties of membranes.

However, new experimental findings tell us that the lipids are ordered and that the freedom of protein mobility is far from being unrestricted. As Jacobson *et al.* have argued, "Most membrane proteins do not enjoy the

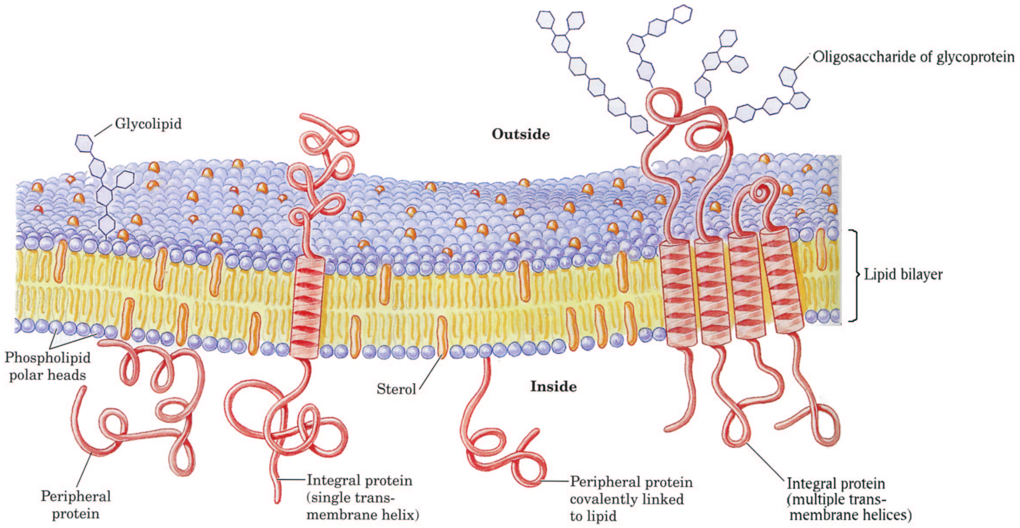

Figure 1.3: Fluid mosaic model for membrane structure. The membrane lipids form a fluid $2D$ solvent where the integral proteins float laterally in the plane of the bilayer. The figure is taken from Ref. [1].

continuous unrestricted lateral diffusion" [20]. Instead, proteins diffuse in a more complicated way that indicates considerable lateral heterogeneity in membrane structure, at least on a nanometer scale. As revealed by single-particle tracking technique [21], the cytoskeletal elements and intracytosolic molecules with functional connections to cell surface receptors have the capacity either to slow down or completely stop the lateral motion of transmembrane proteins. Meanwhile, electron microscopy and scanning-force microscopy [22] have also revealed submicrometer clusters of membrane receptors. These studies showed that the average sizes were in the range of 400 – 800 nm for various receptors. Also, numeral experimental observations [23] have provided evidence for the existence of distinct lipid domains, so-called lipid rafts (see Fig. 1.4), within biomembranes [24].

Combining these new experimental observations, Vereb *et al.* proposed a modified version of the fluid mosaic model of Singer and Nicolson: *dynamically structured mosaic model* [25], in which "emphasis is shifted from fluidity to mosaicism". In this model, nonrandom co-distribution patterns of specific kinds of proteins are supposed to form small-scale clusters at the molecular level and large-scale clusters at the submicrometer level. The cohesive force that maintain these clusters are suggested to come from lipid-lipid, protein-protein, and protein-lipid interactions, as well as supra-membrane effectors such as the cytoskeleton and extracellular matrix. Compared to the fluid mo-

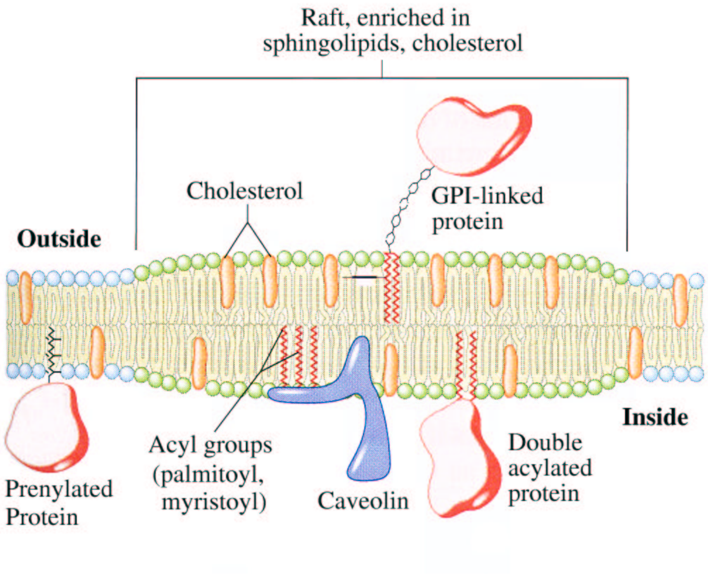

Figure 1.4: An illustration of a typical constitution within a lipid raft domain, which is slightly thicker than other membrane region. The figure is taken from Ref. [1].

saic model, the dynamically structured mosaic model gives a more realistic description of the structural and functional properties of biomembranes.

Despite the variety of their functions, all biomembranes have a common general structure: a lipid bilayer in which membrane proteins are embedded. Also, lipids are the main components in widely used synthetic protein-free membrane systems such as liposomes. In the following section, we will describe briefly the common components and the structural properties of lipid bilayer.

1.3 Lipid bilayer: a two-dimensional fluid

The structural characteristics of a lipid bilayer are determined by its lipid constituents as well as other molecular components. Lipids constitute about 50% of the mass of membranes in an animal cell while the rest of mass is contributed mainly by proteins [2]. The number of lipids can go up to 10^9 in the plasma membrane of an animal cell. Most lipids in cell membranes are amphiphilic since they have a charged or non-charged hydrophilic headgroups and one or two hydrophobic tails.

In an aqueous environment, the hydrophilic headgroup tends to interact with water molecules to form hydrogen bonds which are energetically favorable since the strength of hydrogen bonds is typically 10 – 40 kJ/mol [26], larger than thermal energy (~4 kJ/mol at room temperature). In comparison, the hydrophobic tails prefer to avoid the water molecules and to form a hydrocarbon core in which the van der Waals interactions are maximized with the presence of entropic motion. Depending on their shape, lipids can either form spherical micelles, with tails inward, or they can form a bilayer, which is the preferable structure for lipids with a cylindrical shape.

As mentioned in previous section, it was not until the studies by Frye and Edidin that researchers recognized that individual lipids can diffuse freely within the lipid bilayer. Various techniques can be used to investigate the motion of individual lipids and their different parts in a given lipid bilayer system. In electron spin resonance (ESR) spectroscopy, lipids with unpaired electrons within their headgroup are synthesized to serve as "spin labels", which generate a paramagnetic signal that can be detected by ESR.

Studies show that, in general, there are four kinds of motions that an individual lipid can take. The first kind of motion is known as "flip-flop" which describes the process of a lipid flipping from one side of the bilayer to the other. This process is uncommon and occurs on macroscopic time scales (10^3 sec) [27] for any individual lipid. However, this kind of "flip-flop" can be greatly enhanced by presence of membrane-bound enzymes called *phospholipid translocators* which catalyze the rapid flip-flop of newly-synthesized phospholipids from one monolayer of the endoplasmic reticulum to the other monolayer [2]. In contrast to flip-flops, lipids rapidly exchange their positions with their neighbors within a monolayer at a high rate ($\sim 10^7$ times per second), which gives rise to a lateral diffusion coefficient of about $10^{-7} - 10^{-8}\,\mathrm{cm}^2/\mathrm{sec}$.

The third motion is characterized by the rotation of lipids along their long axis, with relaxation times at nano-seconds [28]. The hydrocarbon tails also undergo entropic motions leading to local disordering. This is the fourth kind of motion within a lipid bilayer. The frequent thermal motion of lipids guarantee the fluidity of a lipid bilayer which is essential to cellular processes such as transport processes and enzymes activities. The fluidity, as well as other structural and permeability properties of lipid bilayer, depend on not only temperature but also its composition. In the following section, we will discuss the common constituents of lipid bilayers.

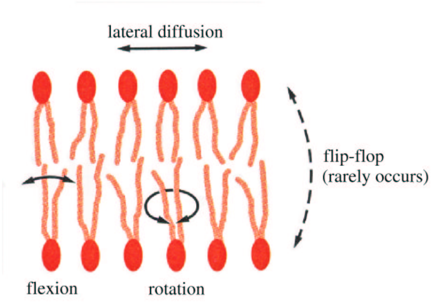

Figure 1.5: Different types of motion of lipids within a lipid bilayer. The figure is taken from Ref. [29]

1.4 Different kinds of lipids

The chemical structure of different kinds of lipids differs in both head groups and hydrocarbon tails, which greatly affects the fluidity of cell membranes [29]. As indicated by the experimental observations in model membranes, a lipid bilayer undergoes a *phase transition* from a liquid state to a two-dimensional rigid crystalline (or gel) state at a characteristic temperature, called phase transition temperature, which will be discussed in Chapter 2. This kind of phase transition takes place at lower temperature for lipids with short or unsaturated hydrocarbon chains (for lipids with the same head-group). The existence of short or *cis*-double bonds reduce the tendency for the hydrocarbon chains to interact with one another, so that the membrane remains fluid at lower temperatures. It is known that some organisms such as bacteria are able to maintain a relatively constant fluidity by adjusting their lipid components in response to temperature changes in their environment. Also, it is known that the cell membranes of a deep sea fish (living in cold water) contain more unsaturated lipids, which guarantee the activities of the membranes at low temperature.

Lipids can be generally divided into different categories, according to the chemical compositions of their headgroups [2]. Phospholipids are the abundant membrane lipids. The lipid compositions of several biological membranes are shown in Tab. 1.1. In the plasma membranes of many mammalian cells, there are four kinds of phospholipids that predominate: phosphatidylcholine (PC), phosphatidylethanolamine (PE), phosphatidylserine (PS), and sphingomyeline (see Fig. 1.6 for their chemical structures). In the plasma membranes of bacterial cells, PE and phosphatidylglycerol (PG) are the major lipid components. Among these lipids, PS and PG are negatively charged while others are neutral but having dipolar headgroup and hence often called

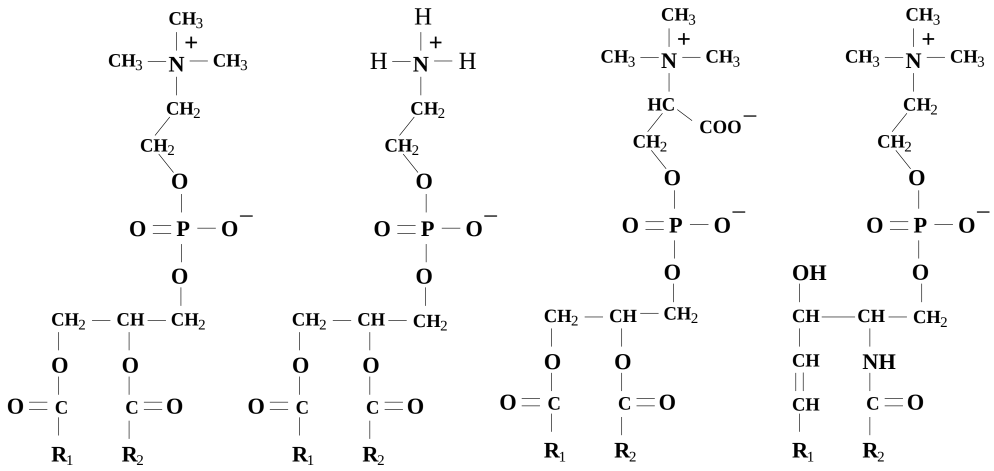

phosphatidylcholine phosphatidylethanolamine phosphatidylserine sphingomyelin

Figure 1.6: Four major phospholipids in mammalian plasma membranes.

zwitterionic. The amount of cationic lipids in cell membranes is very small and only two natural cationic lipids, namely sphingosine [30] and oleamide [31], have been identified in cell membranes. In the synthetic liposomes that are used in drug-delivery and gene therapy, cationic lipids such as synthetic DOTAP and DMTAP, and naturally occurring sphingosine, are used as the lipid components. All of these components are of biological significance in different cellular or synthetic membrane systems.

Lipid	Liver cell plasma membrane	Red blood cell plasma membrane	Myelin	Endoplasmic reticulum	E. Coli bacterium
cholesterol	17	23	22	6	0
PE	7	18	15	17	70
PS	4	7	9	5	trace
PC	24	17	10	40	0
Sphingomyelin	19	18	8	5	0
Glycolipids	7	3	28	trace	0
Others	22	13	8	27	30

Table 1.1: Approximation lipid compositions of different cell membranes. The number is shown in percentage. The table is adopted from Ref. [29]

Just like water acts as a good solvent for ions, the lipid bilayer serves as a two-dimensional solvent for various membrane proteins, some of which can function in the presence of specific phospholipid headgroups. Some cytosolic enzymes bind to specific lipid headgroups exposed in the cytosolic side of a membrane and therefore concentrate at a specific site on a membrane surface. Also, some lipids such as sphingolipids can concentrate in certain areas and hold the neighboring molecules together due to the strong van der Waals interactions resulting from their long and saturated hydrocarbon chains, forming specific zones known as lipid rafts which have been mentioned in previous section about the dynamically structured mosaic model [25]. These rafts are domains that are thicker than other parts of membrane and can accommodate certain membrane proteins, which therefore tend to accumulate in such area. In such a way, lipid rafts have been suggested to help organize these proteins, either by concentrating them in small vesicles for transport or enabling them to function together. However, the structures and functions of rafts in *in vivo* systems are still not fully understood [24, 32].

Lipids also have other biological functions such as cellular signaling. In apoptosis of animal cells, PS lipids, which are usually confined within the cytosolic side of plasma membrane, rapidly retranslocate to the noncytosolic monolayer. This gives a signal to neighboring cells such as macrophages to phagocytes that the cell is dead and they can digest it. Another type of lipid called ceramides, the key intermediates in the bio-synthesis of all sphingolipids, although of trace amount in cell membranes, act as a “second messenger” in cellular signaling cascades for the induction of a series cellular processes such as apoptosis and cell growth [33].

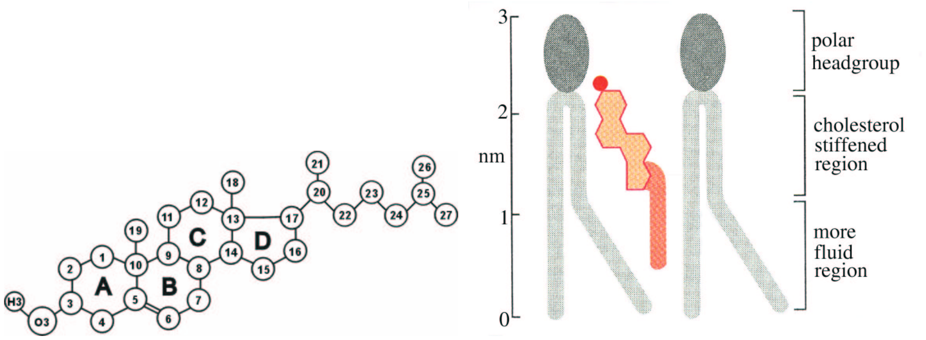

Figure 1.7: (1) Chemical structure of cholesterol molecule (left). (2) Schematic illustration of a lipid bilayer containing cholesterol (right). The second picture is taken from Ref. [29].

Cholesterol and glycolipids are also important components in membranes. Eukaryotic plasma membranes usually contain large amounts of cholesterol. Cholesterol concentration in cell membranes is typically about 20 – 30 mol%, but in red blood cells it may be up to 50 mol% and in ocular lens membranes even as high as 70 mol%. As shown in Fig. 1.7, cholesterol has a polar hydroxyl group, a rigid steroid ring as its middle part and a non-polar hydrocarbon tail. In a lipid bilayer, the hydroxyl groups of cholesterol molecules stay close to the headgroups of lipid molecules with hydrocarbon tails within the hydrocarbon core of the lipid bilayer. With such an orientation, their rigid steroid structures partly immobilize the upper parts of their neighboring lipids so that this region of lipid bilayer is less deformable and permeable to small water-soluble molecules. Although cholesterol tends to reduce the fluidity of membranes, at high concentrations, it also prevents the hydrocarbon chains in lipid components from packing together and undergoing phase transition to gel phase. In this way, it inhibits possible phase transitions and regulates the fluidity of membranes [2].

Glycolipids are lipids that contain sugar groups in their headgroups. In membranes, glycolipids tend to self-associate through both the hydrogen bonds between their sugar groups and van der Waals interactions between their long and mainly saturated hydrocarbon tails. Therefore, they are suggested to be good candidates to form lipid rafts. In an animal cell, glycolipids are found mainly in the outer monolayer of plasma membrane, constituting about 5% of the total weight of all lipid components [2]. Glycolipids have various important biological functions. In the plasma membrane of epithelial cells, for example, glycolipids, confined to the exposed apical membrane surface, are thought to protect the membrane against the harsh environment such as low pH value and degradative enzymes. Glycolipids are also suggested to play an important role in cell-recognition processes [2].

The lipid compositions of the two monolayers in biomembranes are usually different. For example, in the human red blood cell plasma membrane, almost all of the lipids with a choline group in their headgroups (such as PC) are in the outer monolayer, whereas all of the other lipid species containing a terminal primary amino groups (such PE and PS) are found in the inner monolayer. Lipid asymmetry is related to various cellular processes and is of biological importance. For example, many cytosolic proteins bind to specific lipid headgroups within the cytosolic side of membranes. The enzyme *protein kinase C* is activated in response to various extracellular signals, requiring the presence of concentrated PS within the cytosolic side of the plasma membrane, which it binds to, since negatively charged PS is indispensable to its activities. However, further discussion of this asymmetry is beyond the scope of this thesis.

1.5 Lipids, membranes, and their technological applications

The understanding of biomembranes has led to a rapid development in membrane technology that has been applied in various industrial fields. In general, the applications of membrane technology can be divided into two main categories [34, 35]. First, due to their selective permeabilities to different species, membranes have been designed as bio-filters to remove salts, unwanted particles, micro-organisms, and other chemical substances in various industrial processes, such as seawater desalination, recycling of waste water, food-processing, as well as other separation processes in petrochemical, refining, and natural gas industries. Also, various membrane-based apparatus have been widely applied in clinical trials. Second, membrane technology has also been widely applied in pharmaceutical and medical industry where membrane systems, especially liposomes, are used as bio-compatible carriers of drugs, peptides, plasmic DNA, antisense oligonuleotides, for different pharmaceutical and biochemical purposes [37].

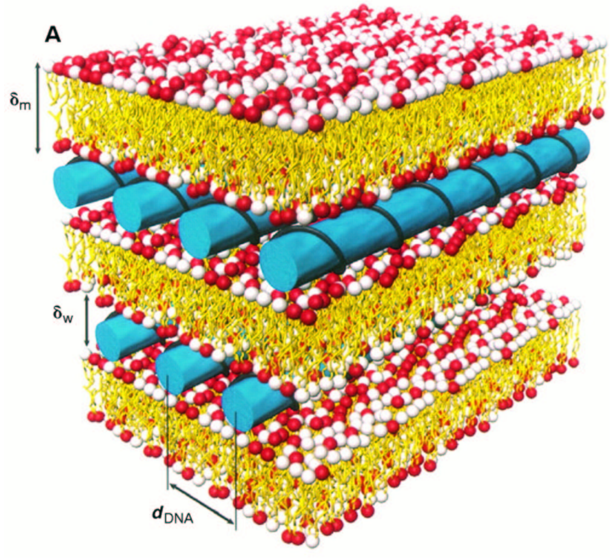

Figure 1.8: Schematic picture of the local arrangement in the interior of a lipid-DNA complexes (lipoplex). The figure is taken from Ref. [36]

In the traditional treatment of carcinoma, the standard chemotherapy is well known to have serious side effects since the anticancer agents are not specifically targeted upon the cancer cells and always cause widespread cell death. Then a question emerges: can we design some kinds of “magic bullets" which can be delivered to where they should go, as suggested by the Nobel Laureate Paul Ehrlich already about 100 years ago? In molecular biology, it is known that an abnormal genetic code leads to certain disorders. Scientists have already mapped the whole human genome which has supplied us essential knowledge that can be used for so-called *gene therapy.* This process involves in replacing the aberrant genetic code with a good one.

Compared to other kinds of drug carriers such as virus carriers that could cause severe side effects or even cancer, liposomes are thought to be good carrier candidates for gene transfer vectors due to their low toxicity. It is known that cationic liposomes can interact with DNA under certain conditions, forming so-called *lipoplexes* (see Fig. 1.8 for a illustration). The delivery of DNA in form of these lipoplexes has been studied extensively due to their great potential in gene therapy [38–40]. Although these techniques based on liposomes as the delivery vectors are still at experimental stages, some scientists are very optimistic about the prospects of the approaches [41].

1.6 Molecular modeling of biological systems: a multi-scale problem

In this thesis, we study membranes using molecular modeling methods. What is molecular modeling? As stated by Tamar Schlick [42], "molecular modeling is the science and art of studying molecular structure and function through model building and computation". In molecular modeling, the evolution of a molecular system in space and time is found through computation based on a simplified description (model) of both the internal interactions within the system as well as the external conditions. Nowadays, molecular modeling is invariably associated with computer simulation, since except for a few simple molecular systems for which modeling can be handled with paper and pencil, the modeling of more complex physical, chemical, or biological molecular systems can only be performed with computers. As early as in 1957, the molecular dynamics approach based on computer was first applied to study a simple system of hard spheres by Alder and Wainwright [43]. That turned out to be a landmark study demonstrating the power and usefulness of computer simulations in studies of many-body systems and the phenomena occurring in them.

Nowadays, various modeling methods have been developed, such as *ab initio*, molecular mechanics, classical molecular dynamics, Monte Carlo, dissipative particle dynamics, etc (see Ref. [45, 46] for a review). Among these methods, *ab initio* is the only approach in which the freedom of electrons are

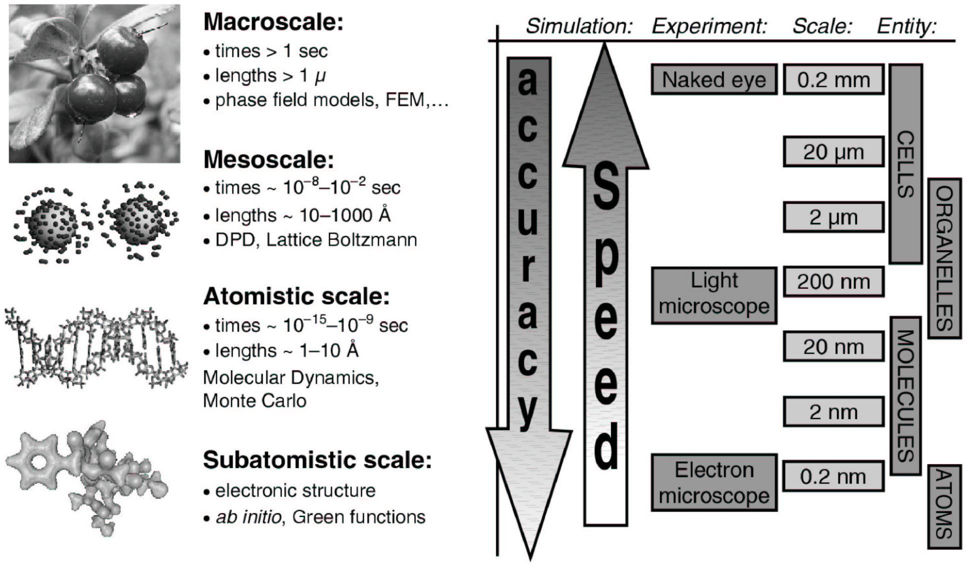

Figure 1.9: An illustration of different time and length scales involved in biological systems, in relations to various experimental and computational techniques. The figure is taken from Ref. [44].

considered while the other approaches are classical.

In spite of the abundance of different modeling methods, a molecular modeling study normally contains three steps. First, a model is selected to describe the intra- and inter-molecular interactions (see Fig. 1.10) in the system, determining how the energy of the system varies as the positions of the atoms and molecules change in time. In practice, the two most commonly used models are quantum mechanics and molecular mechanics. Second, computation based on the selected model system is performed after the initial configuration of the system is provided. The last stage is data analysis which gives a series of system properties and provides a check if the simulation is done correctly.

Molecular modeling of biological systems often involves handling a great number of molecules of different types. In addition, different biological processes take place at different time and length scales. For example, water molecule, having a radius of about 10^{-10} m, is one of the smallest molecules present in biological systems. Its two O–H bonds vibrate at a characteristic time of 10^{-15} s. The *trans-gauche* transition (see Fig. 1.11) time of the hydrocarbon chains of lipids is of the order of 10^{-10} s [47]. At an even larger scale, the biological process of protein folding can take from 1 μs up to 1000 s

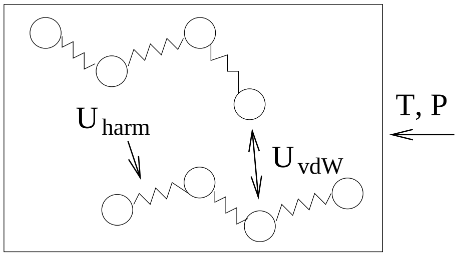

Figure 1.10: An illustration of a molecular system in computer simulation. $\mathrm{U_{harm}}$ represents the harmonic potential which is often employed to model the bond interaction. $\mathrm{U_{vdW}}$ is the van der Waals interactions between atoms. T and P are denoted, respectively, the temperature and pressure imposed externally.

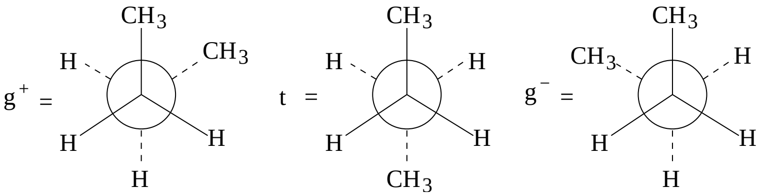

Figure 1.11: An illustration of the Newman projection diagram of *gauche* and *trans* configurations of alkane (butane): g^+, g^-, and t. Adapted from Ref. [12].

depending on the size of the protein. As for length scales, the thickness of a lipid bilayer is about 5 nm while the size of a cell goes up to tens of micrometers. Some biological molecules such as proteins are long polyampholytes (see Fig. 1.12), possessing different spatial substructure at different scales. Human DNA molecule has a length of about one meter and large persistence length which is about 50-100 nm. From the above discussion, we can see that modeling of biological systems is a multi-scale problem. We are not able to solve this problem by using one single method due to both limited computer power and intrinsic deficiency of specific modeling methods. For example, the calculation of folding of even the smallest protein by using *ab initio* methods would take thousands of CPU-years on the most powerful computer at the moment [44]. Therefore, according to the size of the system and properties of interest, we can select specific modeling methods. For example, if we are interested in the electronic structure of an active site of an enzyme, *ab initio* could be the best choice. On the other hand, if we want to investigate the formation of liposomes, dissipative particle dynamics becomes a good candidate. Furthermore, through a procedure called coarse-graining [44], it is possible to bridge these length and time scale gap, although applying this approach is a tough and challenging task and it is currently one of the most studied topics in molecular modeling [48–50].

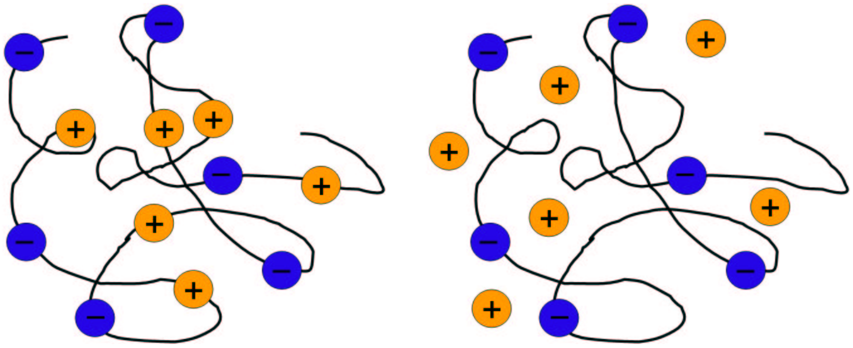

Figure 1.12: Schematic illustration of polyampholytes (left) which contain both negative charges and positive charges, and polyelectrolytes (right), which only contain one type of charges, in balance with counterions.

1.7 Structure of this thesis

In this thesis, we studied a series of membrane/water systems by employing atomistic molecular dynamics method. We aimed to understand the structural and dynamic phenomena in these membrane system at microscopic level. In the first part, we studied cationic DMPC/DOTAP mixture bilayers, which serve as model membranes for cationic liposomes. This is the first computational study of model membranes containing DOTAP lipids. In the second and third parts, we studied anionic pure POPG and POPE/POPG mixture lipid bilayers, respectively. These two studies on the anionic PG membranes were undertaken to elucidate the properties of model bacterial membranes. In the fourth part of this thesis, we analyzed the water dynamics at the membrane/water interfacial region.

This thesis is organized as follows. Chapter 1 and Chapter 2, respectively, give introductions to the biological and physical background of membranes. In Chapter 3, the numerical methods including the molecular dynamics method and other computational techniques are discussed. Chapter 4 presents the original research of this thesis. First, the simulation parameters and the force fields, including the ones developed here, are described. The new force fields are also available on the Internet at www.softsimu.org/downloads.shtml. The rest of the chapter presents the results from studies of charged lipid bilayers and lipid-water interfacial properties. Finally in Chapter 5 we summarize our conclusions and observations.

Chapter 2

Physical Background

2.1 Statistical mechanics

Atomistic molecular dynamics (MD) simulations generate information about a system on a microscopic level, such as atomic and molecular positions and velocities. To calculate the macroscopic properties based on this detailed information, one has to employ the statistical mechanical approach. In this section, we will briefly review the most relevant ideas of statistical mechanics, on which the MD approach and analysis are based. For a broader discussion of statistical mechanics see for example the books by K. Huang [51] and R. K. Pathria [52].

2.1.1 Thermodynamic equilibrium

In thermodynamics, a system is said to be in *thermodynamic equilibrium* if it is in *thermal*, *mechanical*, and *chemical equilibrium* with its environment. Thermal equilibrium implies that there is no net heat exchange between the systems in contact. Thermal equilibrium can be reached when the temperatures of the system and its environment become the same:

$$T_{\text{system}} = T_{\text{environment}}. \tag{2.1}$$

Mechanical equilibrium states that the net forces $\vec{F}_i$ and torques $\vec{\tau}_i$ must be zero,

$$\sum_i \vec{F}_i = 0 \tag{2.2}$$

$$\sum_i \vec{\tau}_i = 0 \tag{2.3}$$

which implies a subtle balance between all interactions. Chemical equilibrium means that the chemical potentials of all substances μ_i in the systems are constant in time and space,

$$\mu_i = const, \tag{2.4}$$

which is commonly characterized by dynamic chemical balance:

$$A + B \rightleftharpoons C + D, \tag{2.5}$$

as illustrated in Fig. 2.1.

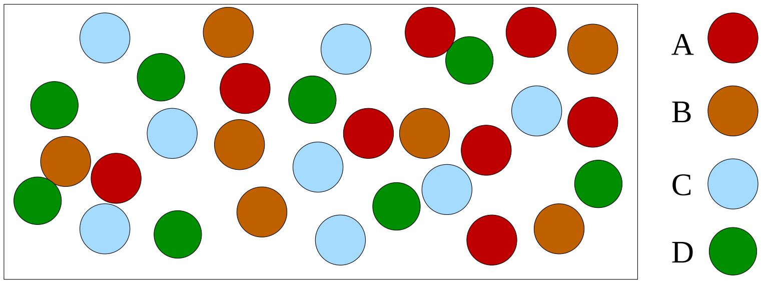

Figure 2.1: An illustration of a system consisting of components A, B, C, and D in chemical equilibrium. The concentrations and chemical potentials of of all components A, B, C, and D do not change in time.

When a thermodynamic system is in equilibrium under a given set of conditions, it is said to be in a definite *state*. For a system in a certain state, its properties of the system can be described by a series of relationships between its extensive and intensive variables. More specifically, in thermodynamic equilibrium, the thermodynamic potential of a given state is minimized. For example, for a system at constant temperature and volume, the Helmholtz free energy

$$F = U - TS, \tag{2.6}$$

is at its minimum. The variables U, T, and S are, respectively, the total energy, temperature, and entropy of the system.

In a MD simulation, a molecular system with a given initial state will evolve into thermodynamic equilibrium through a process called thermalization. To judge whether the system has reached thermodynamic equilibrium, one can measure some intensive variables such as temperature or pressure. More specifically, in the case of membrane-water systems, such as those described in this thesis, one can measure the value of the area per lipid or the number of hydrogen bonds. This is exactly the approach we have followed in our simulations, which will be described in Chapter 4.

2.1.2 Ensemble theory

Consider a classical many-body system in thermodynamic equilibrium with its environment. It consists of N particles of which the coordinates and momenta are denoted, respectively, as $q_1, q_2, \cdots, q_{3N}$ and $p_1, p_2, \cdots, p_{3N}$, which evolve in time within a $6N$ dimensional phase space. Each point in the phase space corresponds to a specific set of $\{q_i, p_i\}$, called a *microstate.* The *ensemble* consists of all possible microstates available to the system.

In statistical mechanics, two most commonly studied ensembles are the *microcanonical* and *canonical ensemble.* In the microcanonical ensemble, the macrostate of the system is defined by the number of particles N, volume V, and energy E. This ensemble describes an isolated system that does not exchange energy/matter with its environment. By the fundamental postulate of thermodynamics, each microstate corresponding to the same energy is equally probable, i.e., the distribution function of microstates is

$$\rho\left(q,p\right) = \frac{1}{\Omega}\delta\left(H\left(q,p\right) - E\right), \tag{2.7}$$

where δ is the Dirac delta function, $\rho\left(q,p\right)$ is the probability for the system to be in the microstate $\{q,p\}$, Ω is the microcanonical partition function, and H is the Hamiltonian.

The canonical ensemble describes a closed system in contact with a heat reservoir at a constant temperature T. The macrostate of the system is defined by the number of particles N, volume V, and temperature T. The distribution function is given by

$$\rho\left(q,p\right) = \frac{1}{Z}\exp\left[-H\left(q,p\right)/k_{\mathrm{B}}T\right], \tag{2.8}$$

where Z is the canonical partition function, and k_{B} is the Boltzmann constant.

For a physical quantity A, each microstate gives a particular value of A. Then, the mean of A can be given as a function of all microstates, according to the distribution of the microstates in this ensemble. For a canonical system, $\langle A\rangle$ is given by

$$\langle A\rangle = \langle A\rangle_{\mathrm{ens}} = \frac{\int Ae^{-H(q,p)/k_{\mathrm{B}}T}d\tau}{\int e^{-H(q,p)/k_{\mathrm{B}}T}d\tau} \tag{2.9}$$

where $\langle A\rangle_{\mathrm{ens}}$ is called the *ensemble average* and $d\tau$ is the volume element of the classical phase space.

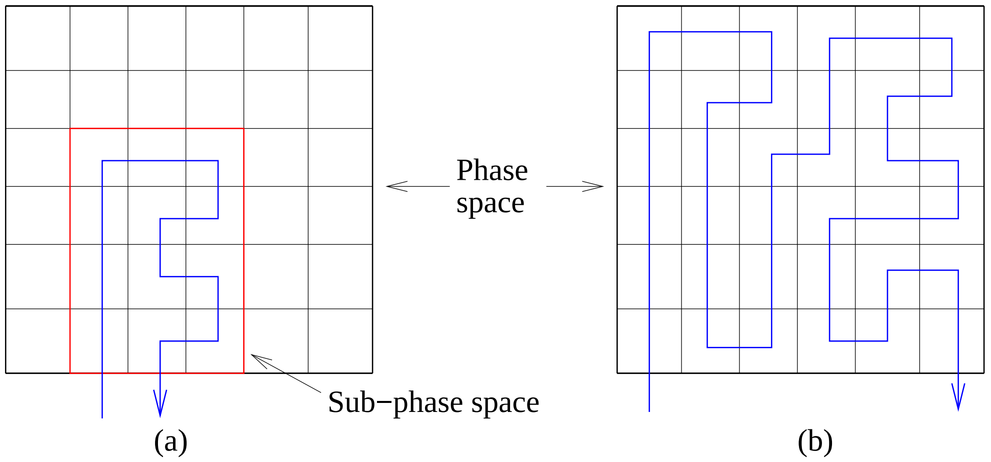

Figure 2.2: (a) A non-ergodic trajectory which does not pass through all possible states in phase space. (b) An ergodic trajectory which passes through all possible states in phase space.

2.1.3 Ergodicity

In a MD simulation, the evolution of a system in time is determined by the Hamilton's equations:

$$\frac{dq_i}{dt} = \frac{\partial H(q,p)}{\partial p_i} \tag{2.10}$$

$$\frac{dp_i}{dt} = -\frac{\partial H(q,p)}{\partial q_i}, \tag{2.11}$$

where $H(q,p)$ is the Hamiltonian of the system. Let us denote a particular point on the trajectory in phase space by Γ. The trajectory itself is denoted by $\Gamma(t)$. Suppose we can measure the instantaneous value of quantity A as a function $A(\Gamma(t))$, which also evolves in time. If the simulation time is relatively short, then only a small part of the phase space, which is a subset of the ensemble, is explored. Then the average $\langle A(\Gamma(t))\rangle$ is said to be biased since it depends on the initial conditions and the length of the simulation, i.e., the subset of microstates. On the other hand, the trajectory of the system will pass through all the relevant region of the phase space over a sufficient long time (see Fig. 2.2). In other words, over a sufficiently long period of time, the trajectory will pass through all possible states according to the distribution function of this ensemble, "without fear or favor" [52]. This statement is called as the *ergodic hypothesis*. Under the ergodic hypothesis, the resulting averages of any physical quantities will no longer depend on the initial or final conditions.

In a MD simulation, the relevant phase space can never be fully explored due to the limited computational power and, in practice, infinite number of possible states. However, provided the simulation time is long enough, it is then reasonable for us to assume that all the relevant states in phase space have been explored. Under this assumption, the mean of quantity A is, instead of an ensemble average, the time average

$$\langle A\rangle = \langle A\rangle_{\mathrm{time}} = \langle A\left(\Gamma\left(t\right)\right)\rangle_{\mathrm{time}} = \lim_{t\to\infty}\frac{1}{t}\int_0^t A\left(\Gamma\left(t'\right)\right)dt'. \tag{2.12}$$

For an ergodic system, the time average and the ensemble average are equal if the time t for measurement is taken as infinite. This is another way to state the ergodic hypothesis.

In MD, the Newton's equations of motion are realized numerically by using a finite difference method. The time for measurement cannot be taken as infinite. The desired quantity of the system is usually measured once every certain number of time steps. The average of this quantity is approximated by:

$$\langle A\rangle = \frac{1}{n_{\mathrm{meas}}} = \sum_{\mathrm{n=1}}^{n_{\mathrm{meas}}} A\left(\Gamma\left(n\right)\right), \tag{2.13}$$

where n_{meas} is the total number of measurements.

According to the ergodic hypothesis, the properties of a system in equilibrium do not depend on its initial conditions provided that this system is ergodic. However, from the practical point of view, the time it takes for a system to reach equilibrium may depend on the choice of initial conditions. Sometimes, to obtain good statistics of the desired properties, one has to average over a number of independent trajectories starting from different initial conditions.

2.2 Phase behavior of model membranes

Under physiologically relevant conditions, membranes are usually in the disordered liquid crystalline or so-called L_α phase, which is characterized by the rapid translational and rotational diffusion of lipids and a highly disordered hydrocarbon core of the membranes. Membrane systems exhibit complex phase behavior under different experimental conditions.

Aligned lipid multi-bilayers are some of the most studied model membrane systems. The structure of these lipid multi-bilayers is characterized as a stack of lipid bilayers and is usually deposited on a solid substrate such as glass or silicon. The hydration level is then controlled by exposing the sample to water vapor to create different relative humidities [53]. This results in a constant

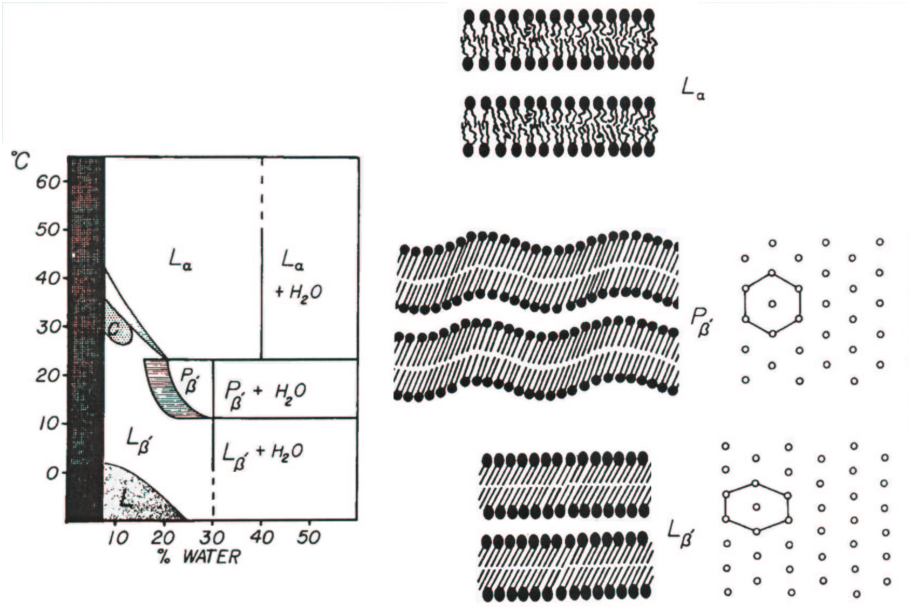

Figure 2.3: Temperature-composition phase diagram of hydrated DMPC multi-bilayers. The structures of different phases L_α, $L_{\beta'}$, and $P_{\beta'}$ are shown in the middle. The packing lattice (viewed from the top) is hexagonal for the $P_{\beta'}$ and distortedly hexagonal for the $L_{\beta'}$ phase. The picture is taken from Ref. [54].

spacing between the neighboring lipid bilayers. At a high temperature and high hydration level, the lipid multi-bilayers are usually in a lamellar fluid phase, like their biomembrane counterparts. As temperature is lowered, a first-order phase transition from the lamellar fluid phase (L_α) to the so-called *gel phase* ($L_{\beta'}$) will occur. This is also called the *main transition* and usually denoted by T_m. For dimyristoylphosphatidylcholine (DMPC), this transition from L_α to $L_{\beta'}$ takes place around $T_\mathrm{m} = 23.5\,^\circ\mathrm{C}$ [55]. Figure 2.3 shows the phase diagram of a hydrated DMPC multi-bilayer system. When other lipids, such as cholesterol, are present, the phase diagram becomes much more complicated. In the gel phase, the hydrocarbon chains of the lipids in the bilayer are frozen in the all-*trans* conformation and are highly ordered (see Fig. 2.3).

Besides these two phases, another major phase $P_{\beta'}$, which is known as the *rippled phase* exists in the middle zone between the L_α and the $L_{\beta'}$ phases and has been identified for many multi-bilayer systems [54]. This phase is characterized by nearly frozen hydrocarbon chains of lipids more highly ordered than in the L_α phase, and the long-wavelength ($10-20\,\mathrm{nm}$) in plane undulation of the bilayers [56], as shown in Fig. 2.3.

In addition to these three major phases, many more *sub-phases* have been identified [57]. For DMPC, x-ray measurements have revealed the existence of three distinct sub-gel phase within the major $L_{\beta'}$ phase [56]. These sub-gel phases are distinguished by the direction of the chain tilt with respect to the position of the neighboring lipids within the same layer. In general, the multi-bilayers in the L_β and $P_{\beta'}$ phases usually develop hexagonal or distorted hexagonal symmetry depending on the amplitudes of the tilt angles of lipid chains.

2.3 Thermodynamics of membranes

The lipid bilayer structure of membranes is essentially stabilized by the hydrophobic effects resulting from the poor solubility of the hydrocarbon tails. In other words, membranes maintain their integrity because of the free energy cost of exposing the non-polar oily interior to polar water molecules. At macroscopic length scale ($> 100\,\mathrm{nm}$), membranes can be considered as two dimensional objects, the thermodynamics of which are governed by their elastic energy and surface tension [58]. Let us next review some basic thermodynamics of membranes. For a comprehensive review, see Ref [58, 59].

In thermal equilibrium, for a fluctuating membrane patch consisting of $2N$ lipids, there are two independent thermodynamic variables: (i) the total membrane area $A = a_\mathrm{m}N$, where a_m is the area per lipid in the equilibrium state; (ii) A_p which is the projection of A on a planar frame that confines the membrane patch. The total area A only depends on the number of molecules N, based on the assumption that the membrane is nearly incompressible. The area A_p can only vary through boundary conditions of the membrane patch.

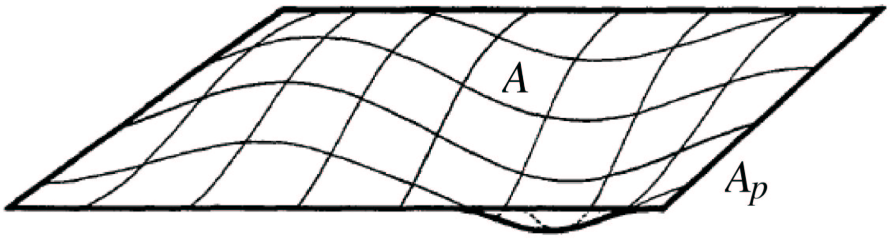

Figure 2.4: A fluctuating membrane spanning a rectangular planar frame of area A_p. $A = a_\mathrm{m}N$ is the total curved surface with a_m being the lateral area per lipid.

As one can see, A and A_p are extensive thermodynamic variables. There are also two corresponding intensive variables: the *area coefficient* γ, conjugate to A, is for incompressible films directly proportional to the chemical potential μ.The *surface tension* τ (τ means surface tension unless otherwise mentioned), conjugate to A_p, corresponds to the physical *surface tension* [58].

With these extensive and intensive variables, one can define four different thermodynamical ensembles for membranes:

i (A, A_p)-ensemble: isolated, framed membranes
ii (A, τ)-ensemble: isolated, unframed membranes
iii (γ, A_p)-ensemble: open, framed membranes
iv (γ, τ)-ensemble: open, unframed membranes.

Experimentally, the most important situations are the (γ, A_p) ensemble, which can be realized in lipid membranes, and the (A, τ) ensemble, which corresponds to the case of lipid vesicles in aqueous solutions (as long as exchange of lipids between the vesicles and the surrounding solution can be neglected).

2.3.1 Open, framed systems

In this ensemble the energy is given by:

$$\mathcal{H} = \gamma A + \mathcal{H}_{el}, \tag{2.14}$$

where $\mathcal{H}_{el}$ contains the contribution of elastic internal forces such as bending energy [58]. The partition function is given by the sum over all configurations $\mathcal{C}$ with A_p being fixed:

$$Z_O = \sum_{\mathcal{C}} \exp\left\{-\frac{\mathcal{H}(\mathcal{C})}{k_\mathrm{B}T}\right\}. \tag{2.15}$$

The free energy in this ensemble is then

$$G_0(\gamma, A_\mathrm{p}) = -k_\mathrm{B}T \ln Z_O(\gamma, A_\mathrm{p}), \tag{2.16}$$

and the film tension is defined as the free energy per unit projected area in the thermodynamic limit,

$$\tau_0 = \lim_{A_\mathrm{p}\to\infty} \frac{G_0(\gamma, A_\mathrm{p})}{A_\mathrm{p}}. \tag{2.17}$$

2.3.2 Isolated, unframed systems

In this ensemble the total membrane area A is fixed while the projected area A_p may fluctuate. The thermodynamic potential is obtained by applying Legendre transforms (the definition of Legendre transform is given in Appendix A) stepwise: first a transform from the (γ, A_p) to the (A, A_p)-ensemble, where both A and A_p are fixed. Then from the (A, A_p)-ensemble to the (A, τ)-ensemble. The first transform is given by:

$$F_l(A_\mathrm{p}, A) = G_0(\gamma, A_\mathrm{p}) - \gamma A, \quad A = \left.\frac{\partial G_0}{\partial \gamma}\right|_{A_\mathrm{p}} . \tag{2.18}$$

The second Legendre transform is defined as:

$$G_l(\tau, A) = F_l(A_\mathrm{p}, A) - \tau A_\mathrm{p}, \tag{2.19}$$

where the film tension τ is defined by

$$\tau = \left.\frac{\partial F_l}{\partial A_\mathrm{p}}\right|_A = \left.\frac{\partial G_0}{\partial A_\mathrm{p}}\right|_\gamma . \tag{2.20}$$

We can now analyze the meaning of the tension τ for isolated, unframed systems with fixed total area A. Let us assume that the projected area fluctuates around its mean value $\langle A_\mathrm{p} \rangle$. This mean value can be obtained by minimizing $F_l(A_\mathrm{p}, A)$ with respect to A_p while keeping A fixed. In the thermodynamic limit it is useful to consider the free energy density $f = F_l/A$ as a function of the area ratio $a_\mathrm{p} = A_\mathrm{p}/A$. In general, two situations are possible, as shown in Fig. 2.5. First, if $f(a_\mathrm{p})$ has its minimum at a non-zero ratio $0 < a_\mathrm{p} < 1$, then the membrane is said to be nearly flat, since, although exhibiting thermal fluctuations, it still keeps the global structure as a two-dimensional surface. At this minimum, the film tension defined in Eq. 2.20 vanishes. This tells us that the surface tension of membranes can be very small.

Secondly, if $f(a_\mathrm{p})$ has its minimum at $a_\mathrm{p} = 0$, the membrane is then said to be *crumpled*. In this case, the membrane is so shrunk by striking thermal fluctuations that its spanning in space does not scale linearly with its internal tension [59–61].

We hereby only consider membrane systems which are locally planar and free of topological changes. In the next section, we will discuss conformations of membranes based on the well-known spontaneous curvature (SC) model and then discuss the general elastic properties of membranes.

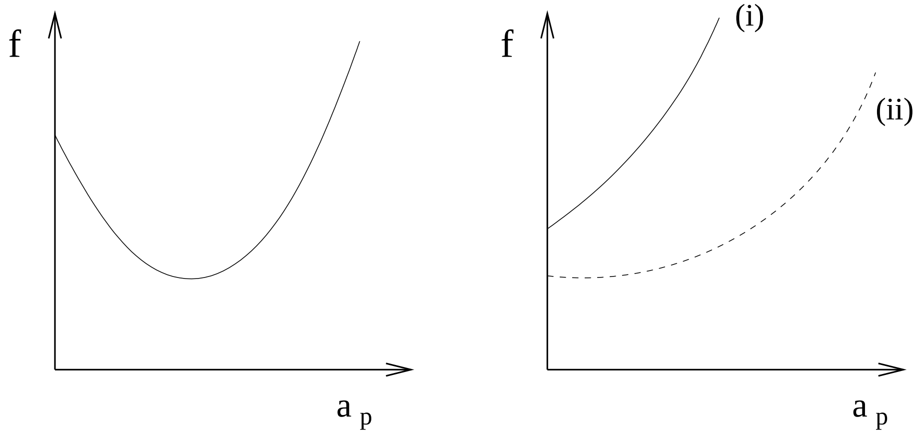

Figure 2.5: The free energy density f as a function of the area ratio a_p. (a) f has a minimum for $a_\mathrm{p} > 0$ and the tension τ vanishes. (b) f has its minimum at $a_\mathrm{p} = 0$ and the tension τ may either be positive (i) or zero (ii).

2.3.3 Conformation of membranes

On the microscopic length scale, lipids, confined to a bilayer, undergo thermal motion characterized by both lateral diffusion and out-of-plane protrusions with respect to the average lipid/water interface. At the mesoscopic or up to the macroscopic level, the thermal fluctuations of membrane do not decay but develop into striking shape fluctuations, which dominate the conformation as well as the mechanical properties of membranes. Experiments have shown that these thermally excited fluctuations can lead to shape transformations in membrane systems [60] (see Fig. 2.6).

At the macroscopic level, membranes act as highly flexible two-dimensional materials. The conformational behavior can be understood in terms of theoretical concepts such as bending elasticity and surface curvature. Theoretical models [62–64], though simple, have provided insight into the understanding of the diversity of structural conformations of membranes. Here we will discuss the elastic free energy of membranes based on the spontaneous curvature model proposed by Canham [62] and Helfrich [63].

2.3.4 The Helfrich free energy

Let us first recall the assumptions of the spontaneous curvature model (SC) [62, 63], which has been discussed by Peliti [59].

In the SC model, a membrane is described as a two dimensional surface embedded in three dimensional space. This model is based on the following assumptions of the free energy of the membrane:

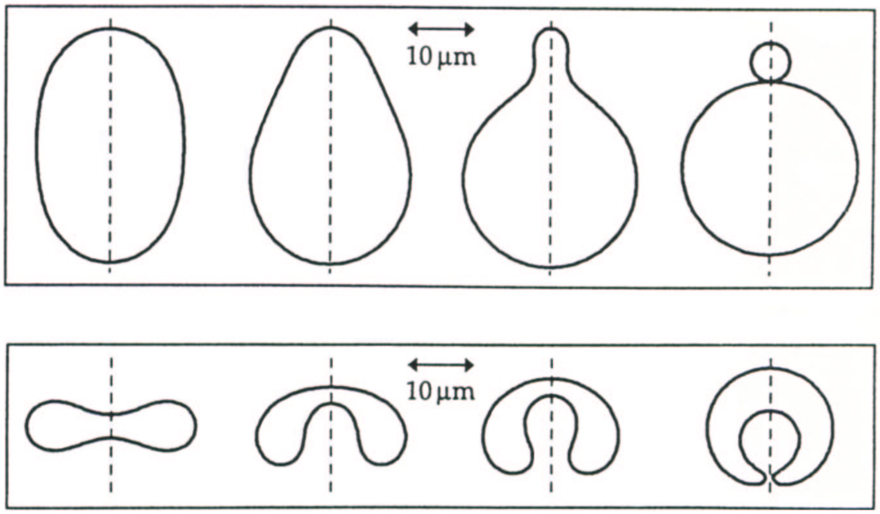

Figure 2.6: Shape transformations of vesicles induced by a change in temperature. These shapes are axisymmetric with respect to the broken line. The figure is taken from Ref. [60].

- The membrane surface is smooth and can be locally represented by the parametric equation $\vec{r} = \vec{r}(\underline{\sigma})$, where $\vec{r}$ denotes a point in three dimensional space, and $\underline{\sigma} = (\sigma^1, \sigma^2)$ are local coordinates of the surface. The function $\vec{r}(\underline{\sigma})$ is infinitely differentiable.

- The free energy density can be described as a local functional of $\vec{r}\,(\underline{\sigma})$ and its derivatives. This assumption rules out the effects of the interaction of the membrane with itself, such as the cases when a part of the membrane folds on the rest.

- The free energy must be invariant under Euclidean transformations applied to $\vec{r}$ and under reparametrization transformations like $\underline{\sigma} \to \underline{\sigma}^{'} = \underline{\sigma}^{'}(\underline{\sigma})$.

Based on the above assumptions, considering only the contributions of derivatives of $\vec{r}$ up to the second order, the so-called *Helfrich free energy* [59] of a membrane is given by

$$F = \int_S \mathrm{d}A \left[\gamma + \frac{1}{2}\kappa \left(H - H_0\right)^2 + \bar{\kappa} K \right], \tag{2.21}$$

where $\mathrm{d}A$ is the area element and γ is area coefficient. The integral is extended over the membrane surface S. The coefficients κ and $\bar{\kappa}$ are known as

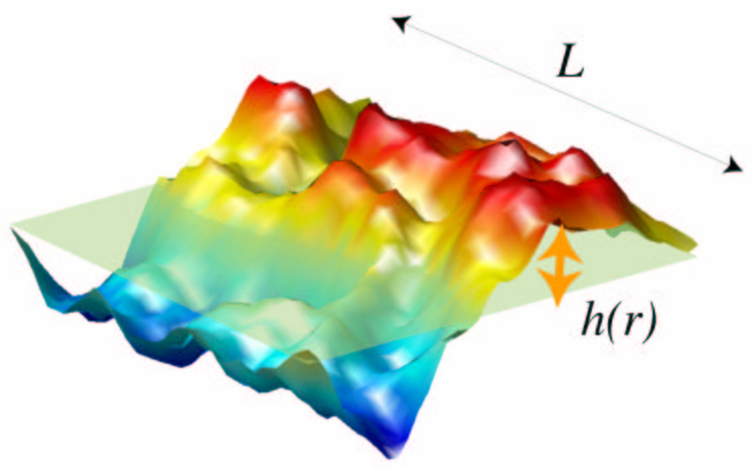

Figure 2.7: In the spontaneous model, the membrane is considered as a two dimensional surface. The picture is taken from Ref. [65].

the *bending rigidity* and *Gaussian rigidity*, respectively. The quantity H_0 is called the *spontaneous curvature*.

The second term in the integral represents the change in energy if the average curvature of the film deviates from the spontaneous curvature, which is a property of a specific membrane system. The third term represents the part of energy which depends on the *Gaussian curvature* (for mathematical definitions of H and K, see Appendix B).

The spontaneous curvature model can be used to describe the configurations of different membrane systems. It can be even applied to investigate complex transformations of membranes when a few more realistic parameters are introduced [64].

In cases when phase transformation of membranes is not considered, as shown by Lipowsky [60], according to the Gauss-Bonnet theorem of differential geometry [60], the free energy contribution from the Gaussian curvature remains constant for a membrane system which does not undergo a topological change. For such systems, Eq. 2.21 becomes

$$F = \int_S \mathrm{d}A \left[\gamma + \frac{1}{2}\kappa \left(H - H_0\right)^2\right]. \tag{2.22}$$

which can be simplified further to

$$F = \int_S \mathrm{d}A \left[\frac{1}{2}\kappa \left(H - H_0\right)^2\right]. \tag{2.23}$$

when surface tension is negligible as in the case of a vesicle.

Based on the Helfrich free energy description of membranes, general conformational properties can be derived [60]. Below, we briefly review some elastic properties of membranes in the frame of the SC model.

In the absence of surface tension, the shape conformation of a fluid membrane is determined by the bending rigidity κ, and the shape fluctuations consisting all existing bending modes. At certain temperature T, for a membrane patch of linear size L, the roughness of the membrane is characterized by spatially anisotropic bumps (see Fig. 2.7 for examples of bumps) of transverse extension $L_\perp \sim (k_\mathrm{B}T/\kappa)\,L$ [66], which represents a boundary case [60], because the overall slope of the bumps, $L_\perp/L$, does not decay for large L.

In fact, the relation $L_\perp \sim (k_\mathrm{B}T/\kappa)\,L$ only holds for L which is smaller than the persistence length $\xi_\mathrm{p} = a\exp\left[c\kappa/k_\mathrm{B}T\right]$, where a is a microscopic length scale characterizing the distance between lipid molecules within the membrane and c is a dimensionless coefficient. As L is increased towards ξ_p, the bending rigidity is reduced by thermal fluctuations which lead to an effective bending rigidity $\kappa_\mathrm{eff} \approx \kappa - c^{'}k_\mathrm{B}T\ln\left(L/a\right)$ for small value of $k_\mathrm{B}T/\kappa$ [67,68]. On the length scale of $L \sim \xi_\mathrm{p}$, the effective bending rigidity of the membrane is of the order of $k_\mathrm{B}T$, which leads to strong shape fluctuations, the character of which is not understood [60]. On the other hand, if a lateral tension γ is applied to the membrane, its roughness is strongly reduced and $L_\perp \sim (k_\mathrm{B}T/\gamma)^{1/2}\left[\ln\left(L/a\right)\right]^{1/2}$.

As one can see, the spontaneous curvature model is a simplification of real membrane system. In a real membrane system, for example, the membrane bending rigidity turns out to depend on a number of factors such as pH, salt concentration, charge density [69], as well as multiplicity of lipid components [70]. Further discussion of such complicated situations are beyond the scope of this thesis.

In the following section, we will briefly discuss the membrane fluctuations at microscopic length scales, characterized by protrusions of lipids.

2.3.5 Microscopic fluctuations

On microscopic length scales, the main feature of membrane dynamics is seemingly random normal displacement of molecules out of the average surface where its neighbors are located, as shown in Fig. 2.8. In this scenario, the curvature energies are weak and do not affect the local properties of membranes [71]. The effective free energy related to these fluctuations is dominated by the interfacial tension, which is proportional to the surface area of contact between the lipids and water [72].

Here, we will briefly discuss the free energy of these lipid protrusions based on a simplified description given by Lipowsky *et al.* [73]. According to this model, the hydrophobic part of a single molecule is taken to have the shape of a small column with a constant cross-section; the area of this cross-section is denoted by A_0 and its circumference by a_0. It is assumed that the headgroup of the lipid is rather rigid and thus does not deform significantly as the lipid protrudes. The protrusion energy is then independent of the molecular shape of the headgroup.

First consider a protrusion of a single lipid. The free energy related to this protrusion is

$$\triangle E = \sigma a_0 l, \tag{2.24}$$

where σ represents the free energy of the interface between the non-polar part of the molecule and the polar solvent, and l is the distance that the lipid is displaced from its neighbors, as shown in Fig. 2.8.

The probability for such a fluctuation is $\sim \exp(-\triangle E/k_\mathrm{B}T) = \exp(-l/l_\mathrm{sc})$ with the length scale $l_\mathrm{sc} = k_\mathrm{B}T/a_0\sigma$. One can then estimate the typical protrusion amplitude of individual lipids for a general membrane. For a lipid molecule with circumference $a_0 \approx 3\,\mathrm{nm}$ and interfacial tension $\sigma = 0.02\,\mathrm{J/m^2}$, the typical length related to an individual protrusion is $l_\mathrm{sc} \approx 0.07\,\mathrm{nm}$ at room temperature with $k_\mathrm{B}T = 4.12 \times 10^{-21}\,\mathrm{J}$.

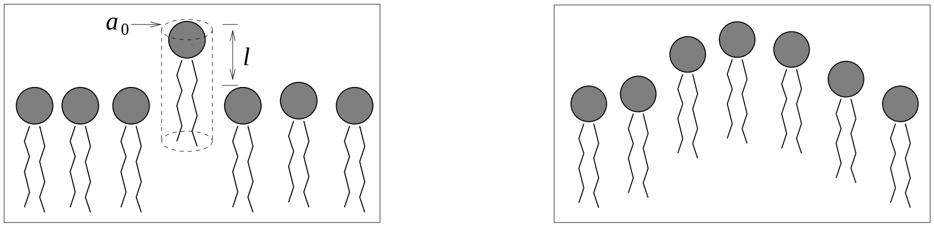

Figure 2.8: Cartoon of single (left) and collective (right) thermally excited protrusions.

Similarly, for the collective protrusion modes, consider a rough membrane in which all molecules can be displaced with respect to the average lipid/water interface. The separation of the protruding lipid i from the other lipids is now described by the local displacement field l_i which varies along the membrane surface. Each lipid is considered to interact with n nearest neighbors. The free energy of such a membrane configuration is given by

$$H\{l\} = \sum_{ij} (a_0 \sigma n)|l_i - l_j|, \tag{2.25}$$

and its statistical weight is given the Boltzmann factor $\sim \exp\left[-H\{l\}\right]/k_\mathrm{B}T$.

By comparing this model with a *Solid-on-Solid* model for wetting [74], Lipowsky *et al.* [73] noticed that Eq. 2.25 can be transformed into a continuum mathematical description

$$F_{\mathrm{prot}} = \int \mathrm{d}x\, \mathrm{d}y \frac{1}{2} \gamma_{\mathrm{prot}} | \bigtriangledown h(x,y)|^2, \tag{2.26}$$

where γ_{prot} is denoted as the protrusion tension [70]. From the above equation, it can be seen that the long-wavelength protrusions should be easier to excite than shorter ones since the area exposed to water will be smaller.

On mesoscopic length scales, the thermodynamic behavior is dominated by the thickness fluctuations, i.e., peristaltic motion which is defined as the antisymmetric motion of two monolayers of membrane. For a more thorough discussion related to the peristaltic fluctuations, see Ref. [75].

2.4 Membrane electrostatics

The majority of membrane systems found in nature, or designed for some purpose, are either negatively or positively charged. For example, most animal biomembranes are found to be negatively charged since about $10-20\%$ of their lipid components are anionic. In comparison, liposomes that are used in drug-delivery or gene therapy usually contain cationic lipids, which guarantee higher delivery efficiency of liposomes as carriers through anionic biomembranes [76].

Electrostatic interactions within membranes have great effects on a number of membrane properties, such as rigidity, structural stability and dynamics as well as phase behavior. Furthermore, the charges associated with the membrane surface induce an electrostatic membrane surface potential, which also influences the conformations of many molecules and thus participates in the intracellular and intercellular recognition [77].

Most of the membrane systems studied in this thesis are either negatively or positively charged, and their electrostatics produce some of their most interesting properties. In this section, we will briefly discuss different interactions of electrostatic origin within hydrated membrane systems.

2.4.1 Hydrogen bonding, hydrophobic effect, and hydrophilicity

Water is a vital substance in all living systems, providing an aqueous environment where the biological processes take place. Water has many unusual properties such as higher melting point, boiling point, and heat of vaporization than most other common solvents [2], which are consequences of electrostatic interactions.

A water molecule contains two hydrogen atoms and one oxygen atom, as shown in Fig. 2.9. According the *hybridization theory* [78] applied to a water molecule, the outer electrons of the oxygen atom adopt the *sp*^{3} hybridization, forming four orbitals arranged as a rough tetrahedron. Each hydrogen atom shares one electron pair with the oxygen atom. The H-O-H angle is 104.5° instead of 109.5° of a perfect tetrahedron because of crowding of the nonbonding orbitals of the oxygen atom [2] (see Fig. 2.9).

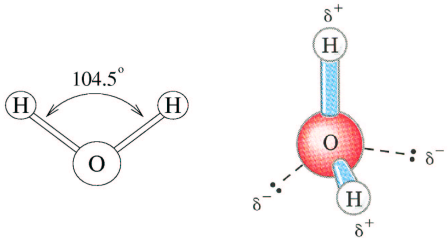

Figure 2.9: (a) Chemical structure of a water molecule (left). (b) The dipolar nature the water molecule is shown by ball-and-stick model (right). The two hydrogen atoms have localized partial positive charge (δ^+) and the oxygen atom has a negative charge $2\delta^-$. The second picture is taken from Ref. [2]

The oxygen atom is more electronegative than the hydrogen atoms. Therefore, the oxygen atom carries a net negative charge while the hydrogen atoms are positively charged (see Fig. 2.9), forming two electric dipoles within a water molecule, one along each of the O–H bonds. As a result, there is an electrostatic attraction between the oxygen atom of one water molecule and the hydrogen atom of its neighbor. This kind of interaction of electrostatic origin is called a *hydrogen bond*, as shown in Fig. 2.10. In pure liquid water, the strength of hydrogen bonds is about 20 kJ/mol, comparable to the

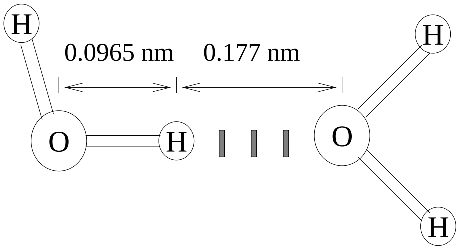

Figure 2.10: Schematic illustration of a hydrogen bond between two adjacent water molecules.

thermal energy in an aqueous solution. In an aqueous phase, "flickering clusters" of water molecules can be formed, as shown in Fig. 2.12. On average, a water molecule forms hydrogen bonds with 3.4 other water molecules at room temperature. The existence of enormous number of hydrogen bonds give rise to a high heat of vaporization of water. Not just limited to water, hydrogen bonds can also form between an electronegative atom, called the *hydrogen acceptor*, and a hydrogen atom covalently bonded to another electronegative atom, called the *hydrogen donor*, as shown in Fig. 2.11. The formation of these hydrogen bonds is energetically favorable. That makes water a good solvent for most biomolecules which are generally charged or polar compounds, examples being glucose and glycine. Compounds which easily dissolve in water are said to be *hydrophilic* (Greek, "water-loving").

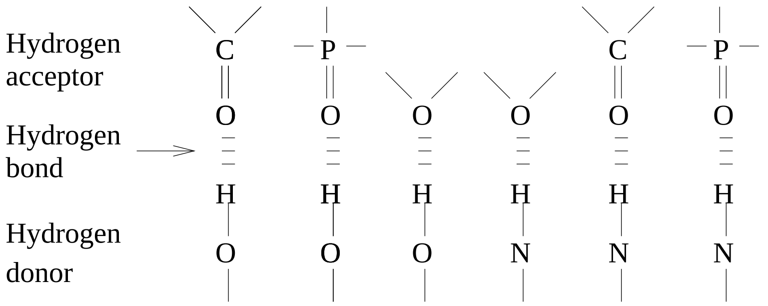

Figure 2.11: Common hydrogen bonds in membrane systems, which are strongest when the hydrogen acceptor, the hydrogen, and the hydrogen donor are along a straight line. The picture is adapted from Ref. [2]

On the other hand, most non-polar compounds such as alkanes are not able to form hydrogen bonds when dissolving in water. These compounds are said to be *hydrophobic* (Greek, "water-fearing"). When water molecules come in contact with hydrophobic molecules, they arrange themselves in such a way that they lose as few hydrogen bonds as possible. For example, for small non-polar molecules such as methane in an aqueous phase, the volume occupied by a methane molecule is so small that surrounding molecules form a "cage" to adopt the methane molecule, without breaking any hydrogen bonds. Similar effects can also be found for chain-like hydrophobic molecules dissolving in water, as shown in Fig. 2.12. Therefore, an individual hydrophobic molecule dispersing in an aqueous solution forces the surrounding water molecules to become highly ordered which leads to a decrease in entropy. However, for hydrophobic solutes which have a large surface area, it is impossible for the adjacent water molecules to maintain a complete hydrogen-bonding network. In these cases, water molecules will move away from the non-polar solutes and form interfaces around them [79].

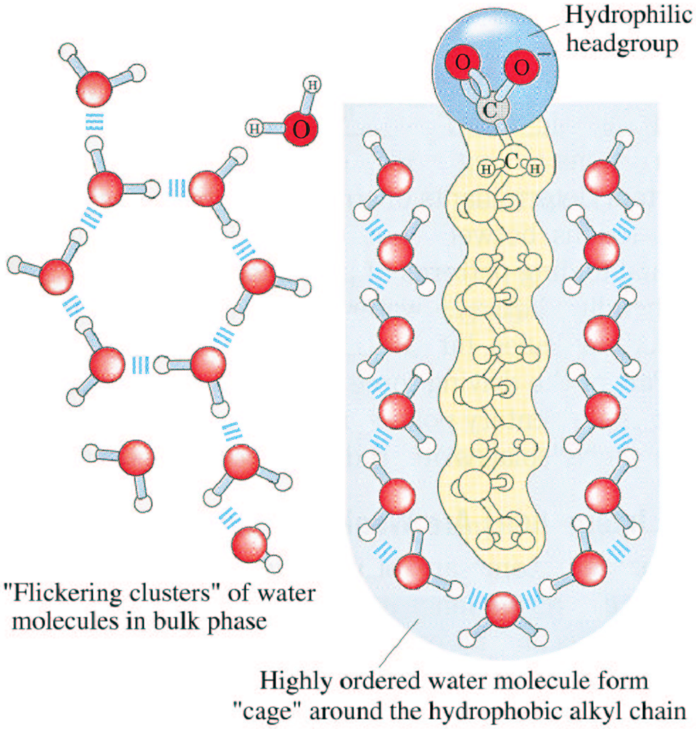

Figure 2.12: (a) Schematic illustration of a water cluster (left). (b) Individual fatty acid with long hydrophobic alkyl chain, dispersing in an aqueous environment, is surrounded by a layer of highly ordered water molecules (right). The figure is taken from Ref. [2].

The hydrophobic effects produce the driving force to stabilize the structures of membrane systems, in which the hydrocarbon lipid tails stay together to avoid contact with water whereas the hydrophilic headgroups interact favorably with water molecules.

2.4.2 Other electrostatic interactions

In membranes, besides forming hydrogen bonds with water molecules, lipids are also able to form charge pairs [80], i.e., electrostatic attractions between specific charged groups, of their neighbors, as shown in Fig. 2.13. Also, for membranes containing lipids with hydrogen donor groups, such as phosphatidylethanolamine (PE), intra- and inter-molecular hydrogen bonding is another kind of interaction that has important effects on the properties of membranes.

For charged membranes, the electrostatic behavior becomes much more

Figure 2.13: Schematic illustration of common charge pairs formed between adjacent lipids. (a) charge pair between choline methyl group and carbonyl group (left). (b) charge pair between choline methyl group and phosphate group (right).

complicated. For example, in a lipid bilayer containing cationic and zwitterionic lipid components, the electrostatic interactions between headgroups are usually characterized by re-orientations of the headgroup dipoles due to the charge-dipole interactions between neighboring cationic and zwitterionic lipid components. In these cases, counterions are present to balance the charges carried by the membrane surfaces where the interfacial structure is greatly effected by the strong electrostatic interactions between the lipid headgroups and counterions. For example, a great number of robust ion-lipid bonds are found in a pure POPG and to lead to cluster formation of lipids, which greatly contributes to the dynamic behavior of the bilayer system. These molecular interactions will be discussed in Chapter 4. Below, we will discuss the ion distribution near a membrane surface from a point of view of thermodynamics.

2.4.3 Ion distribution near to membrane: the Gouy-Chapman theory

Generally, in charged membrane systems, the interactions between membrane surface charges and counterions near the membrane surface result in a structure known as a *diffusive double layer* around the membrane/water interface [81]. There the counterions are not totally absorbed on the membrane surfaces due to their mobility. Instead, they are distributed in the aqueous phase in such a way that there is a balance between their entropic dispersion and the electrostatic attraction due to the charged membrane surface.

The diffuse double structure of membrane surfaces has been extensively studied using electrostatic surface models, most of which are based on the *Poisson equation.* In the following, we will briefly introduce one of the earliest and most studied theories: the *Gouy-Chapman theory.*

The Gouy-Chapman theory describes the effects of static surface charges of membranes on the distribution of counterions without the presence of additional salts. It was proposed by Gouy in 1910 and independently by Chapman in 1913 [12,81]. The Gouy-Chapman theory is based on the following four assumptions:

- i the charges carried by the membrane are smeared over the membrane surface uniformly instead of being treated as discrete charges.
- ii the counterions are considered as point charges and their finite size is ignored.
- iii the electrostatic repulsion between counterions at the dielectric interface is not considered.
- iv the solvent (water) is treated as a continuous medium described by a dielectric constant.

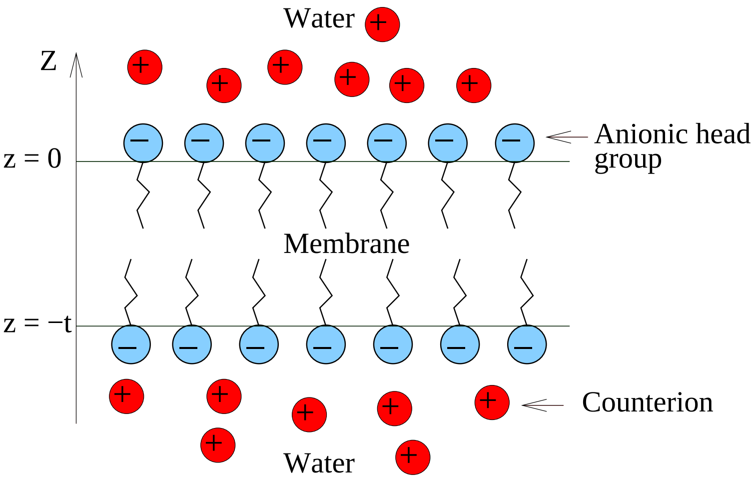

Figure 2.14: An illustration of an anionic membrane of thickness t.

The relation between the electric potential $\psi(\vec{r})$ and the charge distribution $\rho(\vec{r})$ at any point $\vec{r}$ is given by the *Poisson equation*

$$\nabla^2\psi = -\frac{4\pi}{\epsilon_{\mathrm{w}}}\rho(\vec{r}) = -\frac{4\pi e}{\epsilon_{\mathrm{w}}}(z_- n_- + z_+ n_+), \tag{2.27}$$

where z_+ and z_- are the valences, n_+, n_- are the concentrations of the positive and negative ions in the aqueous phase at $\vec{r}$, and ϵ_{w} is the dielectric constant of the aqueous solution.

In the aqueous phase, the electro-chemical potential μ_i of the ith ion is defined as $\mu_i = ez_i\psi + k_{\mathrm{B}}T\ln n_i$, where n_i is concentration of the ith ion. In thermal equilibrium, μ_i remains constant throughout the system. Therefore, the concentrations of the ions in the solution obey a Boltzmann distribution

$$n_i = n_0^i e^{-ez_i\psi/k_{\mathrm{B}}T}, \tag{2.28}$$

where n_0 is the concentration of the ith ion in the reservoir. Combining Eq. 2.27 and 2.28 gives the *Poisson-Boltzmann equation*

$$\nabla^2\psi = -\frac{4\pi}{\epsilon_\mathrm{w}}\rho\left(\vec{r}\right) = -\frac{4\pi e}{\epsilon_\mathrm{w}}\left(z_+ n_0^+ e^{-ez_+\psi(\vec{r})/k_\mathrm{B}T} + z_- n_0^- e^{-ez_-\psi(\vec{r})/k_\mathrm{B}T}\right). \quad (2.29)$$

The Gouy-Chapman theory considers the simpler case of a charged flat surface interacting with monovalent counterions in a salt-free aqueous phase for which $n_0^- = 0\,(n_0 = n_0^+)$. For this case, Eq. 2.29 can be simplified to:

$$\nabla^2\psi = -\frac{4\pi e n_0}{\epsilon_\mathrm{w}}e^{-e\psi(\vec{r})/k_\mathrm{B}T}, \quad (2.30)$$

which is a non-linear equation in the electric potential ψ and can be solved analytically for some boundary conditions. Here we consider two situations: (i) a single flat charged membrane; (ii) two flat charged membranes separated by a short distance.

A single flat membrane

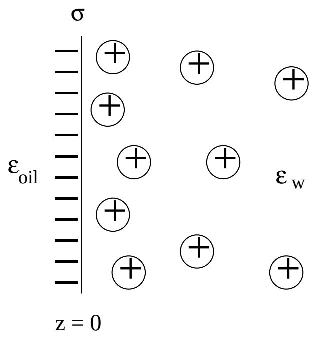

Figure 2.15: Schematic illustration of a single flat membrane treated by the Gouy-Chapman theory. ϵ_oil is the dielectric constant of the membrane hydrocarbon core whereas ϵ_w is the dielectric constant of water.

In this case, the charged membrane occupies the $z = 0$ plane and carries a uniform surface charge density σ, as shown in Fig. 2.15. The aqueous phase occupies the positive half space, $z > 0$. Next we set necessary boundary conditions. First, for large z, the electric field vanishes. At the membrane surface $z = 0$, we have

$$\left.\frac{\partial\psi}{\partial z}\right|_{z=0} = -\frac{4\pi}{\epsilon_\mathrm{w}}\sigma > 0. \quad (2.31)$$

For $z < 0$, the electric field is taken to be zero. This assumes that the electric field can be considered to be a reasonable approximation as long as the ratio of the two dielectric constants, $\epsilon_{\mathrm{oil}}/\epsilon_{\mathrm{w}}$, is much smaller than the ratio between the t/λ_{D}. Here t is the thickness of the membrane (see Fig. 2.14) and λ_{D} is the Debye-Hückel screening length, a characteristic length describing the exponential decay of the electric field due to screening effects of the electrolytes and solvent (λ_{D} is $\sim 1\,\mathrm{nm}$, in a 0.1 M aqueous solution, [26]).

Using the above boundary conditions, Eq. 2.30 can be integrated exactly. The electric potential and the distribution of the counterions are given by

$$\psi(z) = \frac{2k_{\mathrm{B}}T}{e}\ln(z+\lambda_{\mathrm{GC}}) + \psi_0, \tag{2.32}$$

$$n(z) = \frac{1}{2\pi\ell_{\mathrm{B}}}\frac{1}{(z+\lambda_{\mathrm{GC}})^2}, \tag{2.33}$$

where ψ_0 is a reference potential. In Eq. 2.32 and Eq. 2.33, two useful lengths are defined: the *Bjerrum length*, $\ell_{\mathrm{B}} = e^2/(\epsilon_w k_{\mathrm{B}}T)$, and the *Gouy-Chapman length*:

$$\lambda_{\mathrm{GC}} = e/(2\pi|\sigma|\ell_{\mathrm{B}}) = \epsilon_w k_{\mathrm{B}}T/(2\pi e|\sigma|). \tag{2.34}$$

The Bjerrum length is the distance below which the electrostatic interactions dominate the thermal motions for two charges, about 0.7 nm in aqueous solutions at room temperature. The Gouy-Chapman length characterizes the specific thickness of the diffusive double layer of counterions, half of which can be found in the layer between $z = 0$ and $z = \lambda_{\mathrm{GC}}$. This means that at the Gouy-Chapman length, half of the surface charges are balanced by the counterions.

Two flat membranes

The principles used for studying the single flat membrane can be employed to study two flat membranes (with the same surface charge density) separated by a distance d in an aqueous solution. As shown in Fig. 2.16, one membrane surface is located at the plane $z = -d/2$ and the other one occupies the plane $z = d/2$. The electric potential at the membrane surfaces are defined as $\psi_{\mathrm{s}} = \psi(z = \pm d/2)$ with the potential at the imaginary mid-plane $z = 0$ being $\psi_{\mathrm{m}} = \psi(z = 0)$.

The two membrane surfaces are symmetric about the plane $z = 0$. Therefore it is sufficient for us to solve the Poisson-Boltzmann equation only in the interval $[0, d/2]$, which considers the membrane surface on the right side only. Then the boundary conditions are defined as

$$\left.\frac{\partial\psi}{\partial z}\right|_{z=d/2} = \frac{4\pi}{\epsilon_{\mathrm{w}}}\sigma < 0 \tag{2.35}$$

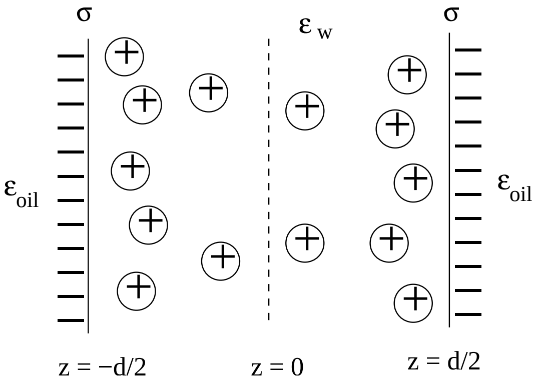

Figure 2.16: Schematic illustration of two flat membranes treated by the Gouy-Chapman theory.

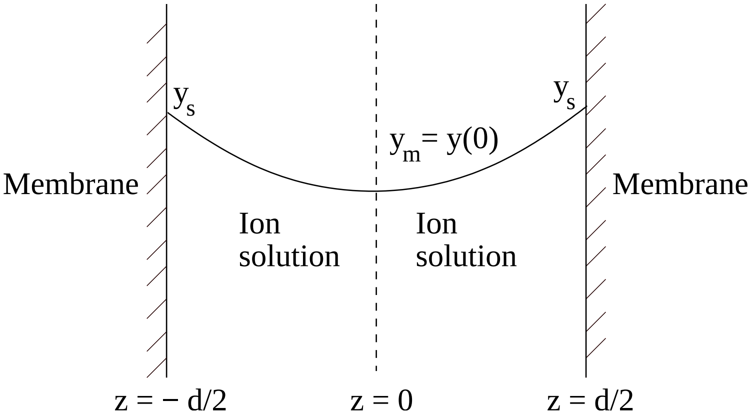

Figure 2.17: Schematic drawing of a potential profile $y\langle z\rangle$ (in reduced units) between two charged membranes separated by a distance d. The figure is adapted from Ref. [81].

and

$$\left.\frac{\partial \psi}{\partial z}\right|_{z=0} = 0. \tag{2.36}$$

Using the above boundary conditions, Eq. 2.30 can be solved analytically and the results for the electric potential and the distribution of counterions are given by:

$$\psi\left(z\right) = \frac{k_{\mathrm{B}}T}{e} \ln\left(\cos^2 Kz\right) < 0, \tag{2.37}$$

$$n\left(z\right) = n_{\mathrm{m}} e^{-e\psi(z)/k_{\mathrm{B}}T} = \frac{n_{\mathrm{m}}}{\cos^2 Kz}, \tag{2.38}$$

where the mid-plane ψ_m is taken as the reference potential, $n_m = n_m(z = 0)$ is the concentration of counterions in the mid-plane, and K is given by $K = \left(2\pi e^2 n_{\mathrm{m}}/\epsilon_{\mathrm{w}} T\right)^{1/2}$. There is an electrostatic pressure between the two opposite membrane surfaces which can be derived analytically based on the distribution of counterions. For its derivation, see Ref. [81].

From above discussion, one can see that the ion distribution of counterions near charged surfaces can be described analytically in an elegant way. That can also help us to understand electrostatics in membrane systems. However, like other continuum and mean-field theories, the Gouy-Chapman theory breaks down at microscopic scales where it does not faithfully describe the ion distribution [26].

This discrepancy comes from the approximations within the Gouy-Chapman theory. For example, in the Gouy-Chapman theory, the discrete membrane surface charges are replaced by an uniform charge density which is confined to an infinitely narrow plane. In real membrane systems, the charged or dipolar groups of membrane components protrude outwards or inwards dynamically within the membrane/water interface that not only induces changes in solvent medium (i.e. the water molecules are reorientated near the membrane) but also leads to direct interactions between the charged groups and counterions. Also, the counterions near the membrane surface are correlated due to their repulsive electrostatic interactions, which are not considered in the Gouy-Chapman theory.

In some modern electrostatic models, more realistic factors such the interionic correlations and other higher order effects, are incorporated into the Poisson-Boltzmann equations to describe membranes in a more natural manner [81]. To date, however, there does not exist a universal theory that works for all membrane electrostatics. Any model only applies to a specific membrane systems under various approximations.

2.4.4 Hydration of membrane surfaces

In a lamellar liquid-crystalline phase, membranes, depending on whether they consist of charged lipid components, exhibit different levels of ability to uptake water molecules. Membranes containing a certain amount of cationic lipids are observed to cause a strong, in practice unlimited, swelling (swelling refers to the case where a membranes absorbs water which leads to an increase in the distance between neighboring membranes), i.e., membranes prefer dilute solutions. For membranes consisting of zwitterionic lipids, the uptake number of water molecules per lipid is around 10 to 30, depending on the headgroup of the lipids [82].

Driving force of membrane hydration

In charged membranes, the repulsive double layer force is thought to be the reason for the extensive swelling. At higher hydration levels, the increase in the entropic contribution to the free energy by the counterions, due to increased available volume, exceeds the contribution from the attractive van der Waals forces.

This mechanism can also be described using the Poisson-Boltzmann theory, which implies that this kind of swelling is dominated by an increase in entropy resulting from the Coulomb interactions while the contribution from enthalpy is small [82].

For membranes mainly consisting of glyco- and zwitterionic lipids, the molecular mechanism behind the short-range repulsive force which causes the swelling is not well understood. Many possible suggestions for explaining this phenomenon have been proposed, and one can identify two basic models which help to explain the mechanism.

The first approach was initially proposed by Marcelja and Radic in 1976 [83]. The basic idea of this model is that the membrane electrostatics induce a polarization of water within the membrane/water interface and this polarization decays into the solution with an intrinsic decay length. As the distance between two membranes gets smaller than two times this decay length, the two polarization zones meet. This leads to a repulsive force that will be diminished if more water molecules are introduced. This model is essentially of energetic origin and the free energy related to the hydration is dominated by the enthalpy.

In the second model, as suggested by Israelachvili and Wennerström [84], the repulsive force between two membranes results from the protrusions of the headgroups, which are highly thermally excited, and which can lead to direct contact between the two membranes and thereafter reduce the con-

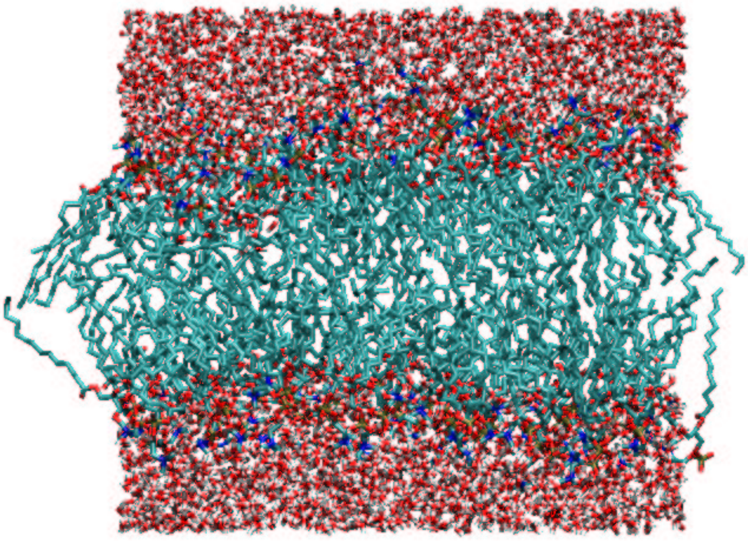

Figure 2.18: A configuration of a hydrated DMPC lipid bilayer, in which water molecules penetrate deeply into the lipid bilayer. The figure is made based on a structure in Ref. [86]

formational freedom. In this mechanism, the free energy is suggested to be dominated by an entropy contribution which increases as more water molecules are introduced between the two membranes.

Ordering of water

In hydrated membrane systems, the hydration layer is referred to as the membrane/water interfacial region in which the water molecules are highly ordered due to the interactions between water molecules and lipid headgroups. The behavior of water molecules within the hydration layer is strikingly different from the water in the bulk phase regarding properties such as hydrogen bonding, mobility, and polarization [85].

As shown in Fig. 2.18, water molecules can penetrate deep in the membrane/water interface and interact with charged groups of lipids such as the choline, phosphate, and carbonyl groups (in case of zwitterionic PC lipid bilayer). In this region, water molecules have fewer other water molecules as their neighbors for hydrogen bonding. However, the ability of water molecules to form hydrogen bonds is enhanced [85]. The limited number of water molecules arrange themselves to bind to each other, which is supposed to be energetically preferable. Experiments have shown that protons diffuse much faster within the hydration layer than in the bulk due to ordering of water molecules [87]. On the other hand, water molecules also form

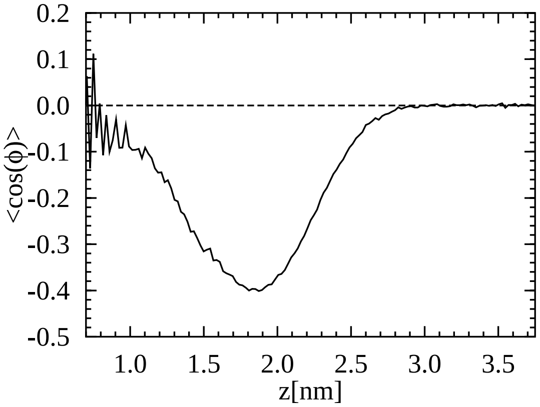

Figure 2.19: Orientational polarization profile of water molecules within the membrane/water interface, characterized by the average cosine of the angle ϕ between the water dipoles and the outward bilayer normal, with $z = 0$ corresponding to the center of the bilayer.

hydrogen bonds with charged lipid headgroups such as the phosphodiester and carbonyl oxygen atoms, as already discussed before. The latter kind of hydrogen bonds are found to be $5-8$ times longer than that of water-water hydrogen bonds [88]. Due to the confined geometry (limited space available within membrane/water interface) and interactions with lipid headgroups, the dynamic behavior of the water molecules in the hydration layer is different from those in bulk phase, characterized by restricted translational and rotational motion.

The ordering of water in the hydration layer is also characterized by a strong polarization, which is suggested [85], for zwitterionic phospholipid membrane, to decay into the bulk phase exponentially(see Fig. 2.19), with a certain decay length which depends on membrane composition. The polarization of water molecules contributes greatly to the electrostatic potential across the membrane/water interface [12], as suggested by MD simulations [85].

Chapter 3

Methods and Models

In this chapter, we will briefly review some of the most relevant computational methods and concepts that are applied in molecular dynamics simulations. We first give a brief introduction to the basic idea and the history of the molecular dynamics method. Then, several basic concepts such as force fields, integration methods, and techniques used to control ensemble properties will be addressed. Finally, we will briefly discuss different approaches applied for constraint dynamics and handling electrostatic interactions. For a more comprehensive discussion of these methods, the books *Computer simulations of liquids* by Allen and Tildesley [89] and *Understanding molecular simulation: from algorithm to application* by Frenkel and Smit [45] are excellent resources.

3.1 The molecular dynamics method

The molecular dynamics (MD) method is a computational approach for investigating equilibrium thermodynamic and dynamical properties of molecular systems by solving the classical Newton's equations of motion.

In MD, the trajectory of the system in phase space describing the dynamics of a given system is obtained by solving the differential form of Newton's second law:

$$\frac{d^2\mathbf{r}_i}{dt^2} = \frac{\mathbf{F}_i}{m_i}. \tag{3.1}$$

This equation describes the motion of a particle of mass m_i with $\vec{F_i}$ denoting the force applied on the particle.

In a typical MD scheme, the forces on the atoms are calculated at the present time step, and combined with the current coordinates and velocities to generate new coordinates and velocities at the next step. The force acting on each particle is assumed to be constant during the time interval and then the particles are moved to their new positions. This process (see Sec. 3.3 for reference) is repeated until the end of the simulation.

Depending on the method by which the forces within a given molecular system are calculated, the molecular dynamics method can be further divided into methodologies such as *classical molecular dynamics* [45] and *ab initio molecular dynamics* [90]. In the classical MD, the nuclear motions of the constituent particles are treated under the frame of classical mechanics. The effects of electronic structure are incorporated into the *force field*, in which the interaction potentials of the nuclei are described. In the *ab initio* MD, the trajectories are generated by using forces calculated from the electronic structure of the system. Therefore, this method can be used to study chemical reactions since it permits breaking and formation of chemical bonds. However, due to the large computational cost, the applications of this method are limited to systems consisting of some hundreds of atoms. For large biological systems such as lipid membranes, we have to resort to the classical MD, which can handle much larger systems, as discussed in Chapter 1. Next, we will briefly review the history of the classical MD (referred to as MD later in this thesis).

The molecular dynamics approach was first used for a system of hard spheres by Alder and Wainwright in 1957 [43]. In the 1960's, a more realistic description of liquid argon in terms of Lennard-Jones particles was achieved by Rahman [91]. After this groundwork, the MD simulations have been increasing in complexity and also applied to biomolecular systems. In 1971, Rahman and Stillinger performed the first simulation of molecular liquid water using the ST2 water model [92]. In 1977, McCammon studied, for the first time, the dynamics of a folded globular protein (bovine pancreatic trypsin inhibitor) in vacuum without electrostatics on a time scale of picoseconds [93]. Since then, MD simulations of ion channels [94], of bilayer membranes [95], and of ion channels in membranes [96, 97], have been performed at different time scales. Today, one is able to simulate transmembrane water channels and other integral proteins in fully hydrated lipid membranes with full electrostatic interactions over a time scale of several nano-seconds [98, 99].

In the next section, we will briefly review the force fields typically employed in MD simulations.

3.2 Force field

3.2.1 General features

A *force field* describes the potential energy part of the Hamiltonian for molecular models employed in computer simulations. It determines the internal energy of the system at any moment of time, and usually consists of a number of terms, each of which describes some physical interactions [44]. A characteristic feature of all current extensively used force fields is that they are pairwise additive. This means that the potential energy is a function of relative positions of pairs of atoms. In practice, a simple force field typically used for molecular systems can be given in the following form:

$$\begin{aligned} V = \quad & \textstyle\sum_{\text{bonds}} \frac{k_i^{\text{b}}}{2}\left(l_i - l_i^{\text{ref}}\right)^2 + \sum_{\text{angles}} \frac{k_i^{a}}{2}\left(\theta_i - \theta_i^{\text{ref}}\right)^2 \\ & + \textstyle\sum_{\text{torsions}} \frac{V_T}{2}\left(1 + \cos\left(n\phi - \gamma\right)\right) \\ & + \textstyle\sum_{i=1}^{N-1} \sum_{j=i+1}^{N} \left(4\varepsilon_{ij}\left[\left(\frac{\sigma_{ij}}{r_{ij}}\right)^{12} - \left(\frac{\sigma_{ij}}{r_{ij}}\right)^{6}\right] + \frac{q_i q_j}{4\pi\varepsilon_0 r_{ij}}\right). \end{aligned} \tag{3.2}$$

Here the first term in Eq. 3.2 models the interactions between pairs of bonded atoms. It is represented here by a harmonic potential with a spring constant k_i^{b} that gives the increase in energy as the bond length l_i deviates from the reference value l_i^{ref}. The second term describes the harmonic potential with a spring constant k_i^{a} related to bending terms which involve three consecutive atoms in the same chain-like piece of a molecule. The reference value of the valence angle is θ_i^{ref}. The third term involves four consecutive atoms, representing torsional interactions, which describe how energy changes when bonds rotate. There, V_{T} gives a quantitative indication of the energy barrier for rotation. Finally, the non-bonded term is usually modeled using a Coulomb potential term for electrostatic interactions and a Lennard-Jones potential for van der Waals interactions. For more technical details of Eq. 3.2, see Ref. [46] To define a force field, one must specify not only the set of po-

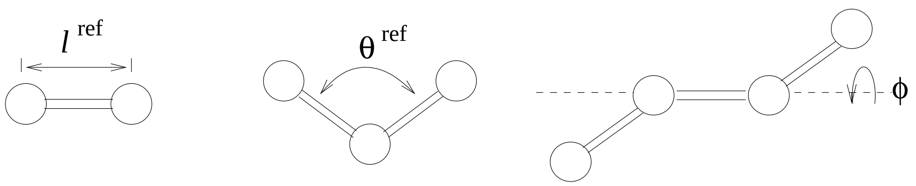

(a) (b) (c)

Figure 3.1: Illustration of bond stretching (left), bond bending (middle) and torsional terms appearing in Eq. 3.2.

tential energy functions in a force field but also the force-field parameters (as well as other practical details such as cutoff distances used in truncating electrostatic and van der Waals interactions). This is a subtle task, since if just one of the parameters is changed, the behavior of the force field can be strongly affected [44].

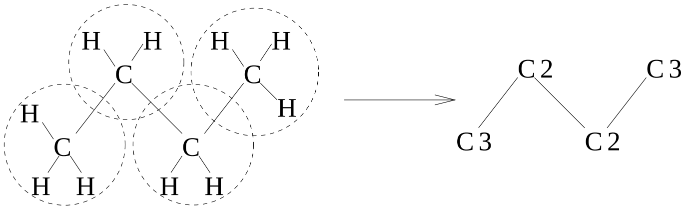

Figure 3.2: Schematic illustration of the united atom model for butane, where $C2$ and $C3$, respectively, represent a methylene and a methyl group.

One type of commonly employed force fields are the united atom force fields [46] typically designed for hydrocarbons, where the hydrogen atoms are incorporated into the carbon atoms to which they are bonded. This is shown in Fig. 3.2. In this way, a methyl or methylene group is considered as a "united atom". The van der Waals and electrostatic parameters will be adjusted to take account of the adjoining hydrogen atoms. Due to these simplifications, computational efficiency is greatly enhanced. This kind of treatment is generally acceptable for hydrogen atoms which are not highly polarized such as those in butane. For highly polarized hydrogen atoms such those in hydroxyl (-OH) groups, the hydrogen atoms must be modeled explicitly.

3.2.2 Force field development

Development and validation of a force field is nontrivial and time-consuming. Using Eq. 3.2 as an example, each of the terms has a clear physical meaning, and the parameters associated with a given term can be obtained either from theory or experiments. The theoretical approach is essentially based on quantum mechanical calculations through which the distribution of partial charges within a molecule can be determined. However, this approach is of limited use since fitting is not easy to perform and depends critically on the quality of the quantum mechanical computations, such as the basis set used in calculations. Thus, it is common to calibrate parameters in force fields by fitting them to empirical data. For example, the parameters for bond stretching and bending can be determined by spectroscopic techniques [100], and the parameters for the van der Waals potential can be derived by fitting parameters to crystal structures [101]. It is important to keep in mind, that there exists no force field that is perfect. The number of different parameter combinations is huge, and slight weaknesses in some of them can sometimes be compensated for by adjusting others. From the above, it is not surprising that there are many different force fields that are commonly employed in the field of biomolecular modeling and simulations.

This variation of force fields can be illustrated by examining the empirical models of liquid water. Despite the small size and simple structure of water, proper modeling of water has turned out to be a very challenging problem. In a liquid state, water molecules are all differing in various properties such as the precise geometry and molecular vibration, since, from a quantum mechanical point of view, the molecular orbitals of water molecules depend on the arrangement of their neighboring water molecules [102]. However, in molecular modeling of water, we are not able to build a water model that covers the whole range of physical behavior of real water molecules, but have to make various approximations to obtain a model that can be used for specific cases.

After the first water model proposed by Bernal and Fowler in 1933 [103], a great number of water models have been developed (see Ref. [104]). In them, different conformational properties, including the structural geometry, as well as different distributions of charges, are applied. In general, water models can be divided into three types. The first kind are characterized by rigid geometry and pairwise interactions including the electrostatic and Lennard-Jones interactions. The second class, so-called flexible models, permits internal conformational changes. In the third case, models have been developed to include the effects of polarization and many-body effects explicitly [46]. Generally, a typical model is developed to get a good fit to one particular physical property such as the density anomaly, radial distribution function, enthalpy of vaporization, and dielectric constant. Whether a model is adequate, depends on whether it gives reasonable results for other physical properties of water. By and large, the more fitting parameters that the model requires, the more precise the model is. However, we have to make a compromise between precision and efficiency because complex models are computationally very expensive.

In practice, the rigid water models are the most commonly used, examples being ST2 [91], TIP3P [105], TIP4P [106], TIP5P [107], SPC [108], SPC/E [109], and PPC [110], the conformations of which are shown in Fig. 3.3. These water models have between three and five interaction sites and a rigid internal geometry. As shown in Fig. 3.3, the SPC and TIP3P water models use three interaction sites involving electrostatic interactions. The two hydrogen atoms carry positive partial charges of equal amount which

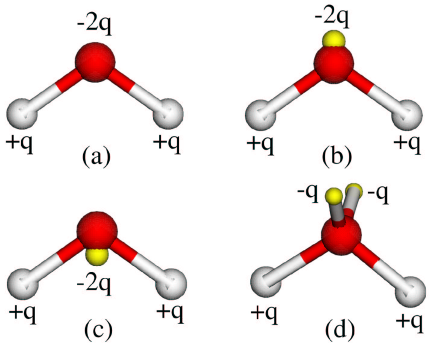

Figure 3.3: General configuration model for (a) SPC, SPC/E, TIP3P, (b) PPC, (c) TIP4P, (d) ST2, TIP5P. The water models belonging to same type of configuration may differ in geometry (bond length, bond angle, etc.) and parameters for charges. For technical details of these models, see related references.

are exactly balanced by the negative charge located on the oxygen atom. The van der Waals interaction between two water molecules is modeled using a Lennard-Jones potential between the oxygens without consideration of hydrogen atoms. For other models such as PPC and TIP4P models, the negative charge is moved away from the oxygen and towards or away from the hydrogen atoms in a planar geometry with other interaction sites. For the ST2 and TIP5P, there are two negative charge sites which form a tetrahedral geometry along with the hydrogen atoms.

The use of rigid internal geometry is, of course, an approximation, and it means that some properties of water, such as the vibrational spectrum, cannot be studied. Introducing more parameters, describing the flexibility and polarization, the performance of a water model can be greatly enhanced, example being the NCC model [111]. However, it is usually more feasible to employ simple water models in simulations of large biological systems considering the computational cost.

As for modeling of biomolecules, there are a number of force fields, each having different strengths. CHARMM force fields [112], for example, serve well for simulations of a number of DNA structures [113]. The force fields used in GROMACS [114], in turn, are likely a better choice for modeling of lipids [115, 116]. AMBER [117] is considered to be good at carrying out simulations for proteins or nucleic acids. Besides these force fields, many other force fields are commonly used and are suitable for different systems.

It is fair to say that all force fields have certain strengths as well as deficiencies. Besides, it is difficult to describe some physical processes such as phase transitions using most of the force fields. Therefore, there is an endless need for improvements on force fields, as comparisons of their results with experimental observations or quantum calculations reveal deviations. In the meantime, we can use the current force fields rather safely if we choose the suitable force fields for specific systems. Even if the results generated by certain force fields are not completely correct quantitatively, they can provide us with qualitative insights into the properties of the systems of interest.

3.3 Integration algorithms

The Verlet algorithm is one of the most commonly used algorithms for integrating the equations of motion in molecular dynamics. It was proposed by Verlet in 1967 [118]. The idea of the Verlet algorithm is based on Taylor expansion. Depending on the way in which the Verlet algorithm derives the positions and velocities, it can be implemented using many different forms, such as the *coordinate Verlet*, the *velocity Verlet*, and the *leap-frog* algorithms.

In the coordinate Verlet algorithm, the positions and accelerations at time t, and the positions from the previous step $\mathbf{r}_i(t - \Delta t)$, are used to calculate the positions $\mathbf{r}_i(t + \Delta t)$ at $t + \Delta t$. In this scheme, Taylor series are used for the time dependence of the coordinates $\mathbf{r}_i$ at the times $t - \Delta t$ and $t + \Delta t$:

$$\mathbf{r}_i\left(t - \Delta t\right) = \mathbf{r}_i\left(t\right) - \Delta t \frac{d}{dt}\mathbf{r}_i\left(t\right) + \frac{\left(\Delta t\right)^2}{2}\frac{d^2}{dt^2}\mathbf{r}_i\left(t\right) - \frac{\left(\Delta t\right)^3}{6}\frac{d^3}{dt^3}\mathbf{r}_i\left(t\right) + \mathcal{O}, \quad (3.3)$$

$$\mathbf{r}_i\left(t + \Delta t\right) = \mathbf{r}_i\left(t\right) + \Delta t \frac{d}{dt}\mathbf{r}_i\left(t\right) + \frac{\left(\Delta t\right)^2}{2}\frac{d^2}{dt^2}\mathbf{r}_i\left(t\right) + \frac{\left(\Delta t\right)^3}{6}\frac{d^3}{dt^3}\mathbf{r}_i\left(t\right) + \mathcal{O}. \quad (3.4)$$

Summing these two equations, one obtains

$$\mathbf{r}_i\left(t + \Delta t\right) \approx 2\mathbf{r}_i\left(t\right) - \mathbf{r}_i\left(t - \Delta t\right) + \frac{\left(\Delta t\right)^2}{m_i}\mathbf{F}_i. \quad (3.5)$$

Then one can approximate the velocity at time t as :

$$\mathbf{v}_i\left(t\right) \approx \frac{1}{2\Delta t}\left[\mathbf{r}_i\left(t + \Delta t\right) - \mathbf{r}_i\left(t - \Delta t\right)\right]. \quad (3.6)$$

Combining Eq. 3.5 and Eq. 3.6 gives the coordinate version of the Verlet algorithm. The truncation error introduced with the Verlet scheme is of the order $\left(\Delta t\right)^4$ for the new coordinates and $\left(\Delta t\right)^2$ for the velocities.

However, a practical problem with this approach is its sensitivity to numerical precision and round-off errors because the velocities are obtained as the difference of two coordinates of the same magnitude. In cases that this drawback is significant, one can use the velocity Verlet algorithm:

$$\mathbf{r}_i\left(t+\Delta t\right) \approx \mathbf{r}_i\left(t\right) + \Delta t \mathbf{v}_i\left(t\right) + \frac{1}{2}\left(\Delta t\right)^2 \frac{F_i\left(t\right)}{m_i}, \tag{3.7}$$

$$\mathbf{v}_i\left(t+\Delta t\right) \approx \mathbf{v}_i\left(t\right) + \Delta t \frac{F_i\left(t\right) + F_i\left(t+\Delta t\right)}{2m_i}, \tag{3.8}$$

which can be shown to be identical to the coordinate Verlet approach (see Ref. [45]). In this algorithm, the calculations of new velocities are performed after computing the new positions and, from these, the new forces.

A slightly modified but equivalent algorithm is the Leap-Frog scheme:

$$\mathbf{r}_i\left(t+\Delta t\right) \approx \mathbf{r}_i\left(t\right) + \Delta t \mathbf{v}_i\left(t+\frac{\Delta t}{2}\right), \tag{3.9}$$

$$\mathbf{v}_i\left(t+\frac{\Delta t}{2}\right) \approx \mathbf{v}_i\left(t-\frac{\Delta t}{2}\right) + \frac{\Delta t}{m_i}\mathbf{F}_i, \tag{3.10}$$

which is used in the GROMACS package [114]. In the Leap-Frog method one disadvantage is that the positions and velocities are not calculated at the same time, as shown in Fig. 3.4. Fortunately, this disadvantage has been circumvented, in GROMACS, by calculating the simultaneous velocities by averaging the velocities at plus and minus half a step, obtaining the same value as in the Verlet algorithm.

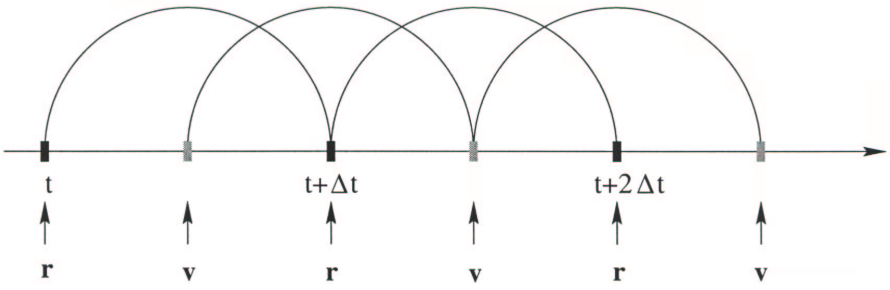

Figure 3.4: A schematic of the leap-frog scheme. Coordinates $\mathbf{r}_i$ and velocities $\mathbf{v}_i$ are calculated at alternating whole and half time steps. The figure is taken from Ref. [75].

There are also some other Verlet-like algorithms, examples being the *Beeman algorithm* [119] and the velocity-corrected Verlet algorithm [45]. For further discussion of these algorithms, see Ref. [45].

As shown by Tuckerman *et al.* [120], the Verlet algorithm can be formally derived using the Liouville formalism from classical statistical mechanics and the *Trotter theorem* [121].

For a classical many-body system, the *Liouville operator* is defined as

$$i\mathcal{L} = \dot{\mathbf{r}}\frac{\partial}{\partial \mathbf{r}} + \dot{\mathbf{p}}\frac{\partial}{\partial \mathbf{p}}, \tag{3.11}$$

where $\mathbf{r}$ and $\mathbf{p}$ denote the position and momenta respectively. Equation 3.11 can be further written as:

$$i\mathcal{L} = i\mathcal{L}_{\mathrm{r}} + i\mathcal{L}_{\mathrm{p}}, \tag{3.12}$$

where $i\mathcal{L}_{\mathrm{r}} = \dot{\mathbf{r}}\,(\partial/\partial\mathbf{r})$ and $i\mathcal{L}_{\mathrm{p}} = \dot{\mathbf{p}}\,(\partial/\partial\mathbf{p})$. The two terms $i\mathcal{L}_{\mathrm{r}}$ and $i\mathcal{L}_{\mathrm{p}}$ can be considered, respectively, as operators for position and velocity propagations, which are non-commuting. Then, based on the *Trotter identity*:

$$e^{(A+B)} = \lim_{P\to\infty}\left(e^{A/2P}e^{B/P}e^{A/2P}\right)^{P}, \tag{3.13}$$

the Liouville operator can be applied to the system as a sequence of exact propagations using either the kinetic or potential part of the Hamiltonian:

$$e^{i\mathcal{L}\Delta t} = e^{i\mathcal{L}_{\mathrm{p}}\Delta t/2}e^{i\mathcal{L}_{\mathrm{r}}\Delta t}e^{i\mathcal{L}_{\mathrm{p}}\Delta t/2}, \tag{3.14}$$

where Δt is the time step of the integration. Through applying Eq. 3.14, the Verlet algorithm is realized (for detailed information of the derivation, see Ref. [45, 120]).

In Eq. 3.14, either propagation is performed under symplectic conditions [45]. Therefore, the Verlet algorithm as a whole is a symplectic integrator, which means the Verlet algorithm conserves the volume in phase space, i.e., area-preserving, in the absence of round-off error. This is also consistent with the Liouville theorem, which states that the volume in phase space is preserved in Hamiltonian systems. This property guarantees the there is no severe energy drift in the Verlet scheme even in long time scales. This is a very important feature since we have to live with the Lyapunov instability [45], which states that the trajectories depend on initial conditions very sensitively. Due to Verlet's area-preserving feature, we can use it safely since the propagation of the phase space vector evolves in the phase space with a constant volume. This means we can have truncating and round-off errors which can lead to different trajectories but without changing ensemble behavior. In comparison, some higher order algorithms (i.e. algorithms that employ higher-order derivatives of the particle coordinates) have very good energy conservation for short times but overall energy drifts for long times. Those schemes are neither time reversible nor area-preserving.

In practice, multiple time scale integrators are commonly employed in MD simulations in which the slowly varying forces (such as the long-range part of electrostatic forces) are calculated less frequently than the rapidly varying forces (such as short-range strongly repulsive intermolecular interactions), based on the fact that different interactions have different intrinsic characteristic time scales. These integrators can also be given using the propagator formalism:

$$U_{\text{slow}}\left(\frac{1}{2}\Delta' t\right)\left[U_{\text{fast}}\left(\frac{1}{2}\Delta t\right)U_{\text{v}}\left(\Delta t\right)U_{\text{fast}}\left(\frac{1}{2}\Delta t\right)\right]^{n}U_{\text{slow}}\left(\frac{1}{2}\Delta' t\right), \quad (3.15)$$

where U_{slow} and U_{fast} are the propagators for the slow and fast varying forces,U_{v} is the velocity propagator [122], and $\Delta' t = n\Delta t$. These algorithms are also time-reversible and symplectic.

3.4 Temperature and pressure coupling

The isochoric and adiabatic molecular dynamics algorithms for solving Newton's equations of motion at constant volume cannot be used for studying dissipative non-equilibrium systems (e.g., to obtain transport properties). Also, the molecular dynamics method is not exact, and is full of numerical approximations such as various cutoffs for different molecular interactions as well as round-off errors. It can be imagined that unavoidable energy drifts will occur especially when long-range interactions such as electrostatic interactions are involved and multiple time-scale algorithms are used [123]. Therefore, to get stable and well-behaved systems, it is often more convenient to perform simulations in other ensembles (e.g., NVT or NPT), in which temperature or pressure coupling is applied.

To keep the temperature constant, it is common to couple the given system to a heat bath, which is commonly called thermostat. Various methods have been proposed for performing constant-temperature MD simulations. The velocity scaling scheme proposed by Woodcock [124] was the first attempt to realize constant temperature MD. In this method, the velocities are scaled according to $\mathbf{v}_i \to \sqrt{T_0/T}\mathbf{v}_i$, where the T_0 and T are the reference and actual temperature, respectively. However, this kind of isokinetic schemes cause problems when the quantities of interest depend on fluctuations.

In the *Andersen thermostat* [125], the desired temperature is achieved by imposing stochastic collisions on randomly selected particles in a Monte

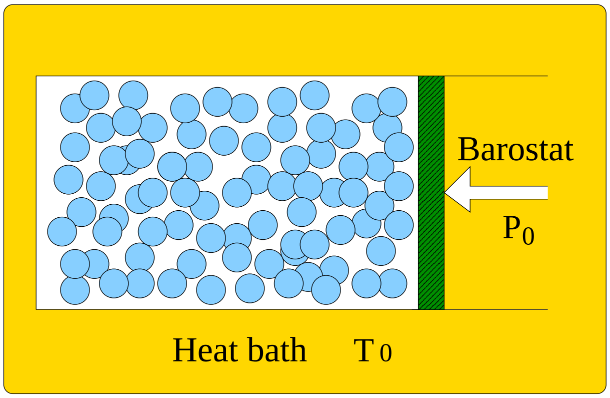

Figure 3.5: Schematic illustration of a molecular system imposed with temperature and pressure coupling.

Carlo-like fashion. The coupling strength depends on the frequency of the stochastic collisions. If a particle is selected to undergo a collision, its new velocity will be obtained from the Maxwell–Boltzmann distribution corresponding to the target temperature T while the velocities of unselected particles are not affected. The Andersen thermostat is very efficient for obtaining a desired temperature and generating a canonical ensemble. However, since it is a stochastic thermostat, the dynamics is disturbed by the stochastic collisions which lead to random uncorrelation of particle velocities. Therefore, the Andersen thermostat should be used with caution when the dynamics of the system is studied.

The same drawback is found with the *Langevin* thermostat [126]. In the Langevin method, the system is coupled to a global heat bath by adding a friction constant to the momentum of the particles. The particles are subject to Gaussian random noise related to the friction constant via the fluctuation dissipation theorem. Besides these two methods, there are also other local thermostat methods, such the *DPD thermostat* [127],and the *Lowe-Andersen thermostat* [128], which are often used in polymer simulations based on coarse-grained models.

Another temperature controlling method for deterministic MD is the *Nosé-Hoover* thermostat, in which the system Hamiltonian is extended by introducing extra variables describing the thermal reservoir and a friction term in the equations of motion:

$$H_{\mathrm{Nose}} = \sum_{i=1}^{N} \frac{\mathbf{p}_i^2}{2m_i} + U\left(\mathbf{r}^N\right) + \frac{\xi^2 Q}{2} + L\frac{\ln s}{\beta}. \tag{3.16}$$

Here, H_{Nose} is the extended Hamiltonian, Q is the parameter describing the coupling strength, and ξ is a thermodynamic friction coefficient related to an additional coordinate s. (For details of this method, see Ref. [45] This method aims to generate a canonical ensemble and is widely used. However, one drawback with the Nosé-Hoover thermostat is that it is not a symplectic algorithm. This problem has been corrected in a modified version of the Nosé-Hoover thermostat called the Nosé-Poincaré method, proposed in a recent study [129].

In the MD simulations presented in this thesis, the Berendsen algorithms [123] are used for coupling of both temperature and pressure. Below, we will briefly discuss the Berendsen temperature/pressure coupling scheme.

3.4.1 The Berendsen temperature coupling

In the Berendsen algorithm, temperature is controlled by rescaling the velocities of particles at each time step in a given system. To describe the basic idea of this algorithm, first consider a system consisting of N particles coupled to a heat bath with fixed reference temperature T_0. The instantaneous temperature is determined by the total kinetic energy:

$$T(t) = \sum_{i=1}^{N} \frac{m_i \mathbf{v}_i^2(t)}{k_\mathrm{B} N_\mathrm{f}}, \tag{3.17}$$

where $N_\mathrm{f} = 3N - 2$ is the number of degrees of freedom provided the total momentum of the system is fixed.

Different from the isokinetic scheme, the Berendsen algorithm applies a weak coupling with first-order kinetics to an external heat bath at desired temperature:

$$\left(\frac{dT}{dt}\right)_\mathrm{bath} = \frac{(T_0 - T)}{\tau_\mathrm{T}}, \tag{3.18}$$

where τ_T is a time constant describing the strength of the temperature coupling.

To achieve this, at each time step, a scale factor λ is given by

$$\lambda = \left[1 + \frac{\Delta t}{\tau_\mathrm{T}}\left(\frac{T_0}{T} - 1\right)\right]^{\frac{1}{2}}. \tag{3.19}$$

Then the velocities are rescaled and positions are updated (in a leap-frog integration frame):

$$\mathbf{v}_i\left(t + \frac{\Delta t}{2}\right) \leftarrow \left[\mathbf{v}_i\left(t - \frac{\Delta t}{2}\right) + \frac{\Delta t}{m_i}\mathbf{F}_i\right]\lambda, \tag{3.20}$$

$$\mathbf{v}_i\left(t\right) \leftarrow \frac{1}{2}\left[\mathbf{v}_i\left(t-\frac{\Delta t}{2}\right)+\mathbf{v}_i\left(t+\frac{\Delta t}{2}\right)\right], \tag{3.21}$$

$$\mathbf{r}_i\left(t+\Delta t\right) \leftarrow \mathbf{r}_i\left(t\right)+\Delta t\mathbf{v}_i\left(t+\frac{\Delta t}{2}\right). \tag{3.22}$$

This weak coupling scheme [123] will produce an exponential relaxation to the reference temperature. Although the Berendsen thermostat does not generate a canonical ensemble exactly, it is one of the most used thermostats due to its efficiency and stability in performing MD simulations.

3.4.2 The Berendsen pressure coupling

In cases where the pressure of a given system needs to be controlled, one can apply a so-called barostat to achieve the desired pressure. The basic idea of the Berendsen barostat is similar to that of the Berendsen thermostat. The coordinates of the particles as well as the length of the periodic boundary box are rescaled to achieve a pressure control:

$$\left(\frac{dP}{dt}\right)_{\mathrm{bath}} = \frac{\left(P_0-P\right)}{\tau_{\mathrm{P}}}, \tag{3.23}$$

where τ_{P} is a coupling constant describing the strength of the barostat.

For an isotropic system, the pressure is given by

$$P = \frac{2}{3V}\left(E_{\mathrm{k}}-\Xi\right), \tag{3.24}$$

where E_{k} is the kinetic energy and Ξ is the internal virial for pair-additive potentials:

$$\Xi = -\frac{1}{2}\sum_{i<j}\mathbf{r}_{ij}\cdot\mathbf{F}_{ij}, \tag{3.25}$$

$$\mathbf{r}_{ij} = \mathbf{r}_i-\mathbf{r}_j, \tag{3.26}$$

where $\mathbf{F}_{ij}$ is the force on particle i imposed by particle j.

The scale factor μ is given by

$$\mu = \left[1+\frac{\Delta t}{\tau_{\mathrm{P}}}\left(P_0-P\right)\right]^{\frac{1}{3}}. \tag{3.27}$$

For anisotropic systems, Eq. 3.27 becomes a tensorial equation with similar form given by the pressure tensor P (more details can be found in Ref. [123]).

There are also various other methods available for constant pressure MD, such as the *Andersen* approach [125] and the *Parrinello-Rahman* method [130].

In the Parrinello-Rahman method, the particles in a given system are described using an extended Lagrangian in a spirit similar to the Nosé-Hoover thermostat. The advantage of the Parrinello-Rahman method is that this method gives the correct pressure fluctuations, which makes it the best choice when fluctuations in pressure are important.

3.5 Constraint dynamics

In molecular dynamics, the time step must be small enough to correctly describe intra-molecular interactions, especially bonding vibrations, which have a relatively high frequency and low amplitude. If all the intra-molecular dynamics are included explicitly, the time step applied in the simulation must be shorter than the period of these bonding vibrations. This makes simulations of molecular systems computationally very expensive.

From a mathematical view, if specific motions occur in a high frequency range clearly separated from other motions, they can be considered as independent motions and can be treated with constraints without affecting the overall motion [122]. In other words, the time scales corresponding to different physical process are apparently separable. In these cases, the degrees of freedom of the fastest motions can be removed, which leads to a great increase in computational efficiency. In this spirit, the fast motions can be constrained by applying constraints. In MD simulations, holonomic constraints, i.e., constrains that do not depend on time, are commonly applied to constrain the bond lengths. Physically that means that the two bonded atoms are connected by a rigid rod with a fixed length. This is shown in Fig. 3.6.

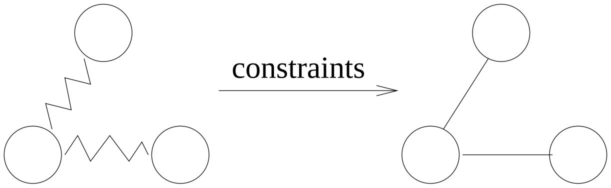

Figure 3.6: In bond length constraints, the two bonded atoms are considered to be connected by a rigid rod instead of a harmonic spring.

By applying holonomic constraints to the bond lengths, the time step in molecular dynamics can be increased by a factor of 4. Also, compared to a harmonic potential, constraints are believed to be more appropriate in representing the physical behavior of bond vibrations, which, at room temperature, are exclusively at their ground state [131].

In general, there are two common methods for applying holonomic constraints. The first involves the solution of a set of nonlinear equations iteratively. This is due to the fact that the connected bonds are coupled. An example is the SHAKE [132] algorithm. For systems containing a great number of rigid water, the SETTLE algorithm, which is an analytic version of the SHAKE algorithm, is much more efficient and suitable for parallelization since it is not iterative [133]. The second type, such as the LINCS [131] algorithm, applies the constraints by solving a matrix equation after linearization.

In this thesis, the LINCS algorithm is applied to constrain all the bond lengths for biomolecules while the SETTLE algorithm is used for constraining water molecules. Next,we will briefly discuss the SHAKE and the LINCS algorithms.

3.5.1 The SHAKE algorithm

In the SHAKE algorithm, a set of unconstrained coordinates are adjusted to a set of new coordinates that fulfill the pre-defined constraints, by solving a set of Lagrange multipliers in the constrained equations of motion in an iterative way.

Consider the equation of motion of a given system that is constrained by K holonomic constraints:

$$\sigma_k\left(\mathbf{r}_1\cdots\mathbf{r}_{\mathrm{N}}\right)=0;\qquad k=1\cdots K. \tag{3.28}$$

Then the total forces under constraints are defined as:

$$\mathbf{F}_i=-\frac{\partial}{\partial\mathbf{r}_i}\left(V+\sum_k\lambda_k\sigma_k\right), \tag{3.29}$$

where λ_k have to be solved to satisfy the constraints equation. The second term of this sum gives the *constraint forces* $\mathbf{G}_i$:

$$\mathbf{G}_i=-\sum_k\lambda_k\frac{\partial\sigma_k}{\partial\mathbf{r}_i}, \tag{3.30}$$

which determine the displacement of atoms involved in constraints.

The implementation of the SHAKE algorithm is an iterative process of three steps:

- Looping over all the constrained bonds to calculate the constraint force based on the deviation from the constrained bond length.

- After the corrections have been applied to all bonds in turn, every bond length is checked. The correction calculation will be repeated if the largest deviation found exceeds a desired tolerance (for example, 0.0001 nm).
- The above steps are repeated until all the constraints are satisfied within the desired tolerance.

The SETTLE algorithm [133] is an analytic version of the SHAKE algorithm. It is specially designed for constraining molecules consisting of three atoms and three constraints, such as water. The corrections to all the bonds are analytically solved such that no iterative process is needed.

3.5.2 The LINCS algorithm

The LINCS algorithm [131] is based on the idea that the applying of constraints can be reduced to solving linear matrix equations with velocity and length corrections. The implementation of the LINCS method includes projection operations and corrections for lengthening, as shown in Fig. 3.7.

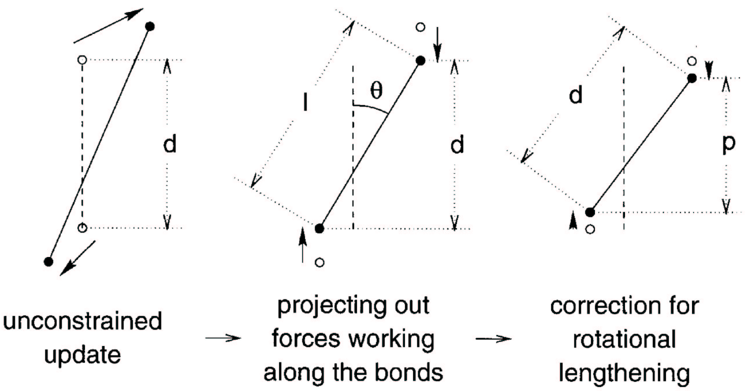

Figure 3.7: Schematic illustration showing the three position updates applied in one time step. The dashed line is the old bond of length d, the solid lines are the new bonds. $l = d/\cos\theta$ and $p = \sqrt{2d^2 - l^2}$. The figure is taken from Ref. [131].

At each time step, the LINCS constraints are applied after an unconstrained update, which consists of two steps. First, the projections of the new bonds on the old bonds are set to zero. The second step is correction applied for the lengthening of the bonds due to the rotation. This correction for rotational effects is actually an iterative process, but in practice, one iteration is usually sufficient for the accuracy required in MD simulations. A detailed derivation of this algorithm can be found in Ref. [131].

Compared to the SHAKE algorithm, LINCS is three to four times faster and has better convergence behavior [131]. More importantly, parallelization of LINCS is much easier to implement,

3.6 Long-range interactions

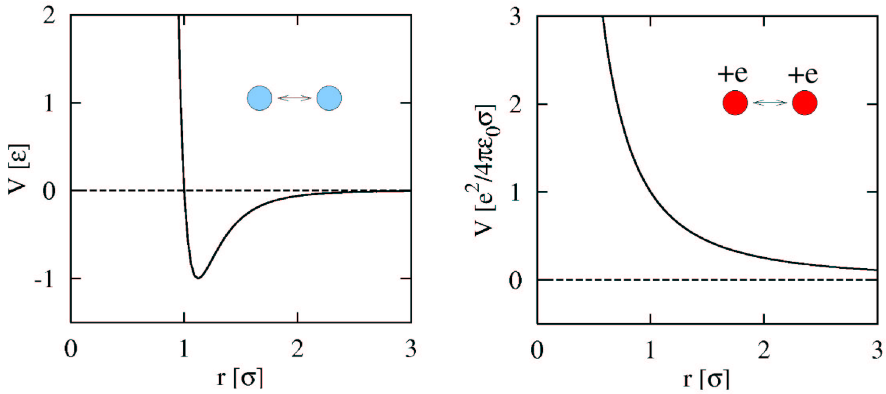

Figure 3.8: Schematic illustration showing the Lennard-Jones potential (left) and Coulomb potential (right). For the definition of relevant parameters, see Eq. 3.2.

Simulations of biological systems often require handling electrostatic interactions. Unlike the van der Waals interactions which are usually represented using a Lennard-Jones potential, the electrostatic interactions, represented by the Coulomb potential, are usually long-range and cannot be cut off at a certain distance, as is done with the Lennard-Jones interactions (see Fig. 3.8). Studies have shown that the cutoff treatments lead to severe unphysical behavior since it implies a delta-function in the force at the cutoffs [122, 134]. On the other hand, mean field treatments such as those including a reaction field can, in principle, only apply to homogeneous fluids [122].

In modeling of biological systems, the Ewald and P^3M (particle-particle particle-mesh) methods as well as their variants are the most commonly used methods. In these methods, the Coulomb potential is split into a short-range and a long-range contributions, chosen to be smooth functions of the distance. The short-range part converges at a certain distance and a cutoff can be applied. The computation of the long-range part involves solving the Poisson equation which describes the potential as a function of charge density. Next, we will briefly review the basic ideas of several commonly used methods. More information can be found in Ref. [45]. In the simulations, we have used the Particle-Mesh Ewald (PME) algorithm [135, 136], combined with the twin-range cutoff (TRC) algorithm [134] for calculations of electrostatic interactions.

3.6.1 Ewald summation

The Ewald summation [89] is one of the most commonly used techniques for calculating electrostatic interactions in a periodic system. This approach, originally designed for calculations of electrostatics in periodic systems such as ionic crystals, is only conditionally convergent.

In the Ewald scheme, each charged particle q_i is effectively neutralized (at large distance) by the superposition of a spherical Gaussian cloud with width $\sqrt{2/\alpha}$,

$$\rho_{\text{Gauss}}(r) = -q_i (\alpha/\pi)^{\frac{3}{2}} \exp\left(-\alpha r^2\right) \tag{3.31}$$

of opposite charge centered on the ion (see Fig. 3.9). The combined assembly of point ions and Gaussian charges become the real space parts of the Ewald summation, which are short-range and can be calculated easily. Then a second set of Gaussian charges centered on the point ions are imposed to nullify the effect of the first set of Gaussians. The potential due to these Gaussian charges is obtained from the Poisson equation and is solved as a Fourier series in the reciprocal space. The complete Ewald sum requires an additional correction, known as the self-energy correction, which arises from a Gaussian acting on its own site, and is a constant. The Ewald's method therefore replaces an infinite sum in real space by two finite sums: one in real space and one in reciprocal space, and the self energy correction.

The expression for the Coulomb energy U is then given by:

$$\begin{aligned} U_{\text{Coul}} &= \frac{1}{2V}\sum_{k\neq 0}\frac{4\pi}{k^2}|\rho(\mathbf{k})|^2 \exp\left(-k^2/4\alpha\right) - (\alpha/\pi)^{\frac{1}{2}}\sum_{i=1}^{N} q_i^2 \\ &+\frac{1}{2}\sum_{i\neq j}^{N}\frac{q_i q_j \operatorname{erfc}\left(\sqrt{\alpha} r_{ij}\right)}{r_{ij}}. \end{aligned} \tag{3.32}$$

The first term on the right-hand side of Eq. 3.32 is the sum of the Fourier contributions to the Coulomb energy. The sum of real space contributions are given by the third term. The second term is the self-interaction which has to be subtracted from the total energy. The derivation of the Ewald summation can be found in Ref. [45]. For molecular systems, however, as opposed to systems comprised simply of point ions, additional modifications are necessary to correct for the excluded (intra-molecular) Coulomb interactions. Unfortunately, the computational cost of the Ewald sum is N^2, or one can get $N^{3/2}$ with better implementation [137]. It is therefore not feasible for use in large systems. Based on the Ewald summation, many other schemes have been derived, such as the P^3M method and the PME method that we use, which will be discussed below.

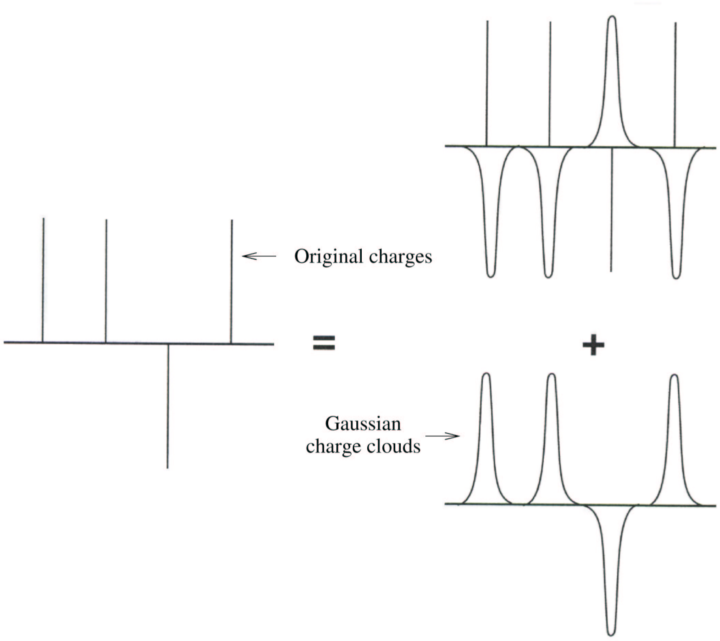

Figure 3.9: Illustration of splitting of point charges in Ewald summation.

3.6.2 P^3M and PME

The Particle-Particle Particle-Mesh (P^3M) method is the earliest particle-mesh scheme for molecular simulations, which was proposed by Hockney and Eastwood [138]. The basic idea of this method is to split the Coulomb potential into two parts by using the following identity:

$$\frac{1}{r} = \frac{f(r)}{r} + \frac{1 - f(r)}{r}, \tag{3.33}$$

in which the idea of using a switching function is similar to the splitting of the Ewald summation into a short-range and a long-range part. In the evaluation of the Fourier space contribution of energy using the above mentioned discrete fast Fourier transform, one has to perform three steps. First, the charges in the system are assigned to grid points using a charge assignment function [139] such as those based on different interpolation methods [136]. Second, the Poisson equation for the discrete charge distribution is solved via the fast Fourier transform technique. Third, after the electrostatic energy has been obtained from the solution of the Poisson equation, the forces are calculated and assigned back to the particles in the system. An in-depth analysis of the P^3M method with error estimation can be found in Ref. [139, 140]

The Particle-Mesh Ewald (PME) is a P^3M-based method proposed by Darden [135, 136]. Instead of directly summing wave vectors of the reciprocal sum, the charges are assigned to a grid using a cardinal B-spline interpolation. This grid is then Fourier transformed with a 3D FFT algorithm and the reciprocal energy term obtained by a single sum over the grid in the reciprocal space. The potential at the grid points is calculated by an inverse transformation, and by using the interpolation factors one obtain the forces on each atom. The PME algorithm scales as $N \log(N)$, and is substantially faster than the ordinary Ewald summation, although, on very small systems, it might still be better to use the Ewald to avoid the overhead in setting up grids and transforms. Compared with the P^3M method, one major advantage about the PME approach is that it gives a well-behaved long-range virial based on the fact that it applies differentiable cardinal B-spline interpolations for charge assignment, which makes the calculation of the long range forces easier.

In all the present simulations, the PME method has been employed to handle the electrostatic interactions within the membrane systems.

3.7 Limitations of molecular dynamics

The molecular dynamics method has a number of important limitations that should not be neglected.

First, each type of interaction term in a force field (see Eq. 3.2) is essentially empirical. The simplified treatment of molecular systems requires a large number of parameters for partial charges, van der Waals interactions, equilibrium values for bonds, angles, dihedrals and force constants. These parameters are usually obtained by *ab initio* calculations based on specific basis set, or by fitting to various experimental observations. However, the quantum calculations are usually performed for molecules in vacuum instead of a solution. Also, experimental parameters such as crystallized structures are obtained for solvent-free systems, which is not the case for biological systems in an aqueous environment. Therefore, the combination of these methods gives no guarantee that these parameters will give good results. On the other hand, in the commonly used force fields, atom polarizability is usually incorporated as an average effect while the detailed effects are not considered. Also, some parameters like the energy parameters related to the van der Waals interactions and the dihedral potentials are difficult to determine, which leads to an uncertainty in thermodynamic and statistical properties.

Second, another limitation is the maximum time step for which the integration of the equations of motion is still stable. We encounter this limitation because we are modeling at atomic length scales which means that the time step must be smaller than the time scale of fastest motion within our models, such as bond oscillations and bending. A typical value, in practice, is 2 fs (10^{-15} s). This means that 500 000 integration steps are necessary to calculate the dynamics of a system during a 1 ns simulation. This limits the duration of current simulations to a maximum of a few hundreds of nanoseconds [44]. Meanwhile, the same practical limitations on computer power dictate that the largest systems that currently can be handled are of the order of hundreds of thousands of particles.

To overcome some of the above limitations, coarse-graining has become an increasingly powerful approach. The idea is that the detailed molecular structural information is transformed into simplified descriptions with less degrees of freedom. This means averaging over some chosen properties of the microscopic entities, and formation of new larger basic units (coarse-grained particles). That enables considerable extensions of the time and length scales that can be reached.

The third major limitation of standard molecular dynamics is the classical treatment of the system, as already mentioned in the beginning of this chapter. This makes it impossible to consider chemical or enzyme reactions without describing at least part of the system quantum mechanically.

Fortunately, much progress has been made to overcome the above limitations. For example, polarizable force fields have been included in some MD packages in recent years, the most notable example being AMBER [117]. Including polarization is also commonly thought to be the trend of the new force field development. Furthermore, some MD packages, such as AMBER [117], have incorporated quantum mechanics based semi-empirical methods into classical molecular dynamics simulations, which makes it possible to consider quantum effects in large molecular systems.

Chapter 4

Molecular Modeling of Membrane Systems

In this chapter, the computational studies of all lipid bilayer systems investigated in this thesis are presented and discussed. We first give an introduction explaining the simulation parameters and physical quantities used for analysis. Then the molecular modeling studies of all membrane systems will be presented and examined in the order as: (i) cationic model membranes; (ii) anionic POPG membrane; (ii) model membrane for bacteria; and (iv) structural and dynamical properties of water near membranes.

Next, we first give a brief introduction to the general simulation setting applied in all systems.

4.1 General simulation setting

The united atom model description employed in our studies has been validated previously [115, 141]. All the parameters for the bonding, bending and improper dihedral terms were taken from the GROMOS force field. The Ryckaert-Bellemans potential [142, 143] was used for the dihedral of the hydrocarbon chains of lipid molecules. The non-bonded parameters for the lipid molecules were taken from the OPLS force field with corrections for the Lennard-Jones interactions between the united $\mathrm{CH_n}$ groups of acyl chains reproducing the experimental observed lipid density [144]. This force field is available online at http://moose.bio.ucalgary.ca/files/lipid.itp. The Lorentz-Berthelot combination rules [46] were applied for calculations of Lennard-Jones interactions. The fractional charges distributed in the headgroups for all the lipids were constructed based on an *ab initio* quantum mechanical calculation of DPPC [145], with adjustments to specific lipids, as will be addressed in the preparations of relevant systems. The SPC model [108] was used for water, while standard GROMACS force field parameters were employed for sodium and chloride ions.

All Lennard-Jones interactions were cut off at 1.0 nm without shift or switch functions. The neighbor list for non-bonded interactions was updated every 10 time steps. Lipid bonds were constrained using the LINCS algorithm [131], while the SETTLE algorithm [133] was used for water molecules. The electrostatic interactions were handled by the particle-mesh Ewald (PME) method [135, 136], combined with the twin-range cutoff (TRC) algorithm [134]. In this scheme, the short-range electrostatic interactions within a distance of 1 nm were calculated at each time step, while the long-range electrostatic interactions beyond this distance were updated every 10 time steps, during which the long-range electrostatic forces remain unchanged. This scheme has been tested by a number of MD simulations [115, 134].

All simulations were performed in the NPT ensemble with a time step of 2 fs using the GROMACS simulation package [43]. In all simulations, the temperature was kept constant using the Berendsen thermostat [123] with a coupling time constant of 0.1 ps. Lipid molecules and solvent (water molecules and ions) were separately coupled to a heat bath. The Berendsen barostat [123] with a coupling constant of 1.0 ps was employed to keep pressure constant (1 bar). The pressure coupling was applied semi-isotropically: the box size in the direction of the bilayer normal (z-axis) and the cross-sectional area (the x-y plane) were allowed to vary independently.

In total, all the MD simulations presented in this thesis took about 60 000 CPU hours on AMD Opteron 2.2 GHz computers.

4.2 General properties for analysis

Here we give definitions for some general physical quantities that will be analyzed in this chapter. Some other properties for analysis will be addressed in specific studies later in this chapter.

A. **Area per lipid**

Area per lipid is an important characteristic quantity of membranes that can be measured experimentally. In simulations, it usually provides a measure for equilibration. In our analysis, we define the area per lipid for all systems as the lateral area divided by the number of lipid molecules in one leaflet (i.e., 64) of lipid bilayers. Besides the area per lipid averaged over all the lipids, the Voronoi analysis [146] is applied in two dimensions to obtain the area for individual molecules at each time step, from which the dynamic behavior of area occupied by each molecule can be analyzed. In the Voronoi analysis

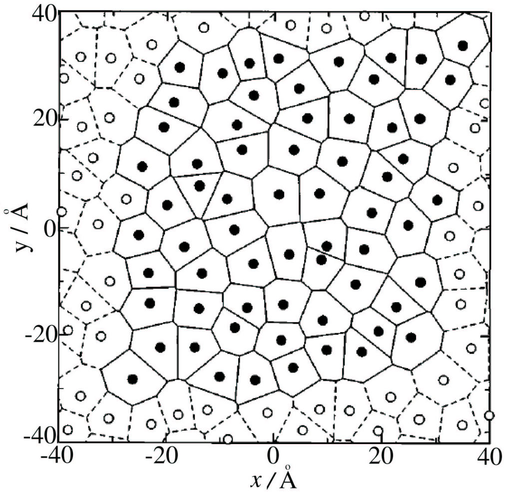

Figure 4.1: Schematic illustration of the two-dimensional Voronoi tessellation for x-y projection of the centers of mass of the lipids in one of the leaflets of the bilayer. The figure is taken from Ref. [146].

employed in this thesis, instead of centers of mass of the whole lipids, we applied the centers of mass of the lipid headgroups for projection of the molecules to the x-y plane. As shown in Fig. 4.1, each molecule belongs to a particular Voronoi cell, the area of which is taken as the area of the molecule. Based on the results from the Voronoi analysis, the area fluctuations for each lipid are calculated using the autocorrelation function

$$C_{\mathrm{A}}(t) = \frac{1}{N}\sum_{i=1}^{N} \frac{\langle A_i(t+t')\, A_i(t')\rangle - \langle A_i\rangle^2}{\langle A_i^2\rangle - \langle A_i\rangle^2}, \tag{4.1}$$

where $A_i(t)$ is the area of lipid $i\,(i = 1, \cdots, N)$ at time t, and $\langle\cdots\rangle$ represents time averages are taken over all configurations used for analysis.

B. **Density profile**

The mass or number density profiles are calculated by separately analyzing each frame of the simulations. At each frame, the bilayer center is determined by calculating the center of mass for the whole bilayer. The bilayer is then divided into many thin slices, in which the position of all atoms are then calculated with respect to the bilayer center.

C. **Electrostatic potential**

To calculate the electrostatic potential across the bilayer, the average charge density profile is first calculated with respect to the bilayer center for each frame. Since the bilayers exhibit mirror symmetry, the charge density profile is averaged over the two monolayers to reduce statistical error. Then electrostatic potential is calculated by integrating the charge density twice with $V = 0$ at the bilayer center ($z = 0$):

$$\phi(z) - \phi(0) = -\frac{1}{\epsilon_0}\int_0^z dz' \int_0^{z'} \rho(z'')dz'', \tag{4.2}$$

where ρ is the local excess charge density.

D. **Order parameters of lipid acyl chains**

The ordering of the lipid acyl chains is usually characterized using the order parameter tensor

$$S_{\alpha\beta} = \frac{1}{2}\langle 3\cos\theta_\alpha \cos\theta_\beta - \delta_{\alpha\beta}\rangle, \tag{4.3}$$

where $\alpha, \beta = x, y, z$, and θ_α is the angle between the α^{th} molecular axis and the bilayer normal (z-axis). The order parameter is then computed separately for all carbons along the acyl chain.

The experimentally relevant deuterium order parameter can be computed from the above as

$$S_{\mathrm{CD}} = \frac{2}{3}S_{xx} + \frac{1}{3}S_{yy}. \tag{4.4}$$

We therefore present our results in terms of S_{CD}. In practice, we used a united atom model and therefore had no explicit hydrogen positions, which had to be reconstructed assuming a perfect tetrahedral arrangement.

E. **Water ordering**

The ordering of water in the vicinity of the bilayerwater interface is described by calculating the time averaged projection of the water dipole unit vector $\vec{\mu}(z)$ onto the interfacial normal $\vec{n}$,

$$P(z) = \vec{\mu}(z) \cdot \vec{n} = \cos(z), \tag{4.5}$$

where z is the z-component of the center-of-mass of the water molecule and vector $\vec{n}$ points away from the bilayer center along the z-coordinate. A positive value of water dipole means that the water dipole points to the inner side of the lipid/water interface while the negative value means the opposite.

F. **Radial distribution function**

The radial distribution function (in three dimension) between particles A and B is defined as

$$\begin{aligned} g_{\mathrm{AB}}(r) &= \frac{\langle \rho_{\mathrm{B}}(r) \rangle}{\langle \rho_{\mathrm{B}} \rangle_{\mathrm{local}}} & (4.6) \\ &= \frac{1}{\langle \rho_{\mathrm{B}} \rangle_{\mathrm{local}}} \frac{1}{N_{\mathrm{A}}} \sum_{i \in A}^{N_{\mathrm{A}}} \sum_{i \in B}^{N_{\mathrm{B}}} \frac{\delta(r_{ij} - r)}{4\pi r^2}, & (4.7) \end{aligned}$$

where $\langle \rho_{\mathrm{B}}(r) \rangle$ denotes the density of particles B around particles A at a distance r, and $\langle \rho_{\mathrm{B}} \rangle_{\mathrm{local}}$ is the average density of particles B around particles A throughout the system. In practice, the density $\langle \rho_{\mathrm{B}}(r) \rangle$ is calculated by first dividing the spherical space of all particles A into many spherical slices and then the density at a specific slice is obtained by summing the number of particles B and divided by the volume of this slice.

Similarly, in two dimensions, the above equation becomes

$$g_{\mathrm{AB}}(r) = \frac{1}{\langle \rho_{\mathrm{B}} \rangle_{\mathrm{local}}} \frac{1}{N_{\mathrm{A}}} \sum_{i \in A}^{N_{\mathrm{A}}} \sum_{i \in B}^{N_{\mathrm{B}}} \frac{\delta(r_{ij} - r)}{2\pi r}, \tag{4.8}$$

where the density $\langle \rho_{\mathrm{B}}(r) \rangle$ can be obtained by dividing the number of particles B by the area of local slice at r.

G. **Coordination number**

In our analysis, the coordination shell of particles A around particles B is determined by the radial distribution of particles A around particles B, i.e., from 0, to the location of the first minimum r_{min} on the radial distribution function. Then the coordination number, i.e., number of particles A in the first coordination shell of particles B, is given by integrating the radial distribution function

$$n_{\mathrm{coord}} = \frac{4\pi}{V_{\mathrm{A}}} \int_0^{r_{\mathrm{min}}} dr r^2 g(r), \tag{4.9}$$

where V_{A} is the van der Waals volume of a particle A. The coordination number n_{coord} describes the number of particles A of interest in the first coordination shell around particles B.

H. **Hydrogen bond**

As mentioned in the beginning of this chapter, all the lipid molecules are represented using united atom descriptions in which only the polar hydrogen atoms are explicitly considered. To determine whether a hydrogen bond exists, we follow the generally accepted approach and define two geometrical parameters: the distance r between the hydrogen and the acceptor, and the donor-hydrogen-acceptor angle (zero extended) α . The conditions $r \leq 0.25\,\mathrm{nm}$ and $\alpha \leq 60^{\circ}$ were then used as criteria for a hydrogen bond to exist, as shown in Fig. 4.2.

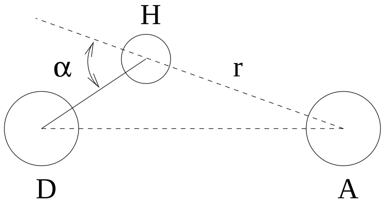

Figure 4.2: Geometrical hydrogen bond criterion. The hydrogen, donor, and acceptor are presented by H, D, and A, respectively.

I. **Self diffusion coefficient**

The self diffusion coefficient D_{A} (in three dimensions) for particle A is determined based on the mean square displacement of particle A given by the Einstein relation [89]

$$\lim_{t\to\infty}\langle|\mathbf{r}_i(t)-\mathbf{r}_i(0)|^2\rangle_{i\in A}=6D_{\mathrm{A}}t, \tag{4.10}$$

where $\mathbf{r}_i(t)$ is the position of particle i at time t.

Next, the computational studies will be presented. We first report our computer simulations on cationic model membranes.

4.3 Cationic model membranes

4.3.1 Introduction

Cationic liposomes have attracted great attention, both experimentally [147–149] and theoretically, due to their various biological applications in the field of pharmaco- and immuno-therapy [150].

In general, the cationic liposomes used for delivery contain at least two kinds of lipid molecules. The key components are the cationic lipids, which serve as the condensing agents of the negatively charged drugs or DNA strands. Also important are the neutral helper lipids, which play a crucial role in determining the structure of the composite condensates. However, despite important advances in both in vivo and in vitro studies on liposome systems, detailed understanding of the structure and nature of interactions within them is still lacking. This requirement goes beyond the scope of most experimental techniques and theoretical analysis [151]. Therefore, atomistic-based molecular dynamics simulations have been performed to elucidate the structural and other properties of cationic liposomes or lipoplex systems [152–154].

Based on these computer simulations, much insight has been gained into the electrostatic interactions within the zwitterionic headgroups of helper lipids and cationic headgroups of cationic lipids. However the role of acyl chains in determining the structural properties of these liposome systems has not been fully elucidated in those simulations since the acyl chains of these lipids are identical. In fact, the difference in the acyl chains of the helper and cationic lipids has been found to contribute to the structural properties of liposomes [155].

DOTAP is the most widely used cationic lipid. It is efficient both in vitro and in vivo applications [149]. It is surprising that there are no publications of simulations of pure or mixed DOTAP bilayer systems. In our study, we prepared cationic DMPC/DOTAP systems in which the helper lipids and the cationic lipids differ in their acyl chains. We aimed at investigating the effects of chain composition on the structural and electrostatic properties of the cationic lipid bilayers, which serve as microscopic models for liposome systems.

Below a brief description of the preparation of all systems will be given. Then, the simulation results will be shown and discussed.

4.3.2 System preparation

In this study, we prepared five cationic DMPC/DOTAP lipid bilayers at different DOTAP fractions of 0.06, 0.16, 0.25, 0.50, and 1.0, respectively. These bilayers consisted of 128 lipids, ~ 3600 water molecules, and Cl^- ions of equal number as DOTAP lipids to keep the charge neutrality. All initial configurations were built up based on an equilibrated hydrated DPPC lipid bilayer [156]. The initial configurations were prepared the following way: First, the desired number DPPC lipid molecules were selected randomly and replaced by DMPCs by cutting two ending carbon for each chain. Second, to build DOTAPs two extra hydrocarbons and two *cis* double bond at C9 (see Fig.4.3 for labeling) were added on both acyl chains of the remaining DPPCs, in which the phosphate groups were removed to obtain DOTAP lipids. The fractional charges within the DOTAP headgroups were taken from a study

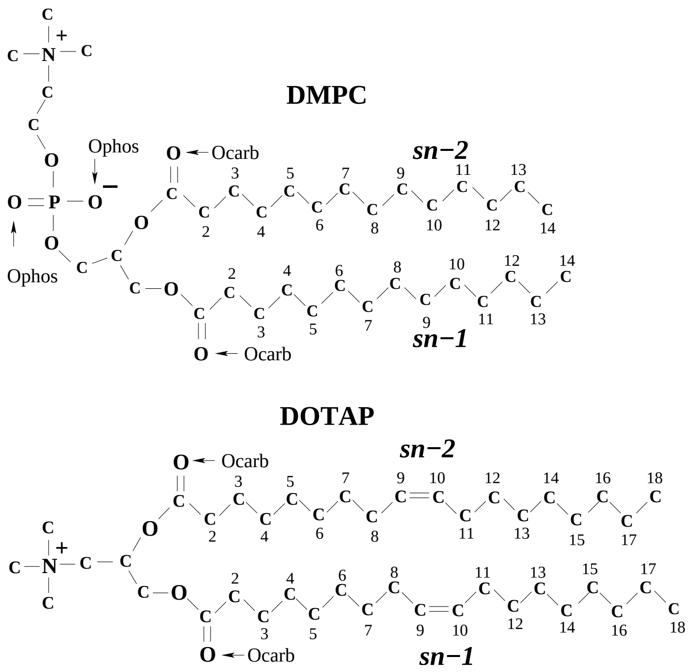

Figure 4.3: Chemical structures of the two lipids considered in this work: dimyristoylphosphatidylcholine (DMPC) and dioleoyloxytrimethylammonium propane (DOTAP).

about DMPC/DMTAP bilayers [152]. The force field of the DOTAP lipid is available at www.softsimu.org/downloads.shtml. For each system, energy minimization based on steep descent algorithm [46] was performed to release the internal constraints. Then a 10 ps run in the NVT ensemble was performed to remove unphysical voids due to structural modifications. After that, the simulations were performed for 50 ns for all systems. The first 10 ns trajectories were for pre-equilibration and the last 40 ns trajectories were for data analysis.

4.3.3 Simulation results and discussion

System dimensions

Area per lipid is one of the most fundamentally characteristic properties of membranes that can be measured via experimental techniques [157]. It is closely related to other physical quantities of membranes such as ordering of hydrocarbon chains and dynamic behavior of membrane lipids. In this study, area per lipid was also employed as an indicator of equilibration of all bilayer systems.

Figure 4.4a shows the area per lipid of all systems as a function of DOTAP fraction. The average area per lipid in a pure DMPC bilayer was taken from a previous study about DMPC/DMTAP bilayers, where the same force field parameters for DMPC were used. The value $\langle A \rangle = 0.656 \pm 0.008\,\mathrm{nm}^2$ is in good agreement with experimental observations [158]. The average area per lipid in a pure DOTAP bilayer was found to be $\langle A \rangle = 0.734 \pm 0.010\,\mathrm{nm}^2$. The experimental measurements of area per lipid in pure DOTAP and DMPC/DOTAP mixture bilayers, to our knowledge, are still lacking. In a recent experimental study [159], the area per lipid in a pure DOTAP bilayer was assumed to be $0.65\,\mathrm{nm}^2$ based on that of a DOPE bilayer and molecular modeling. However, considering a previous molecular dynamics study of cationic lipids [152] and our results, we suggest that this could be an under-estimation.

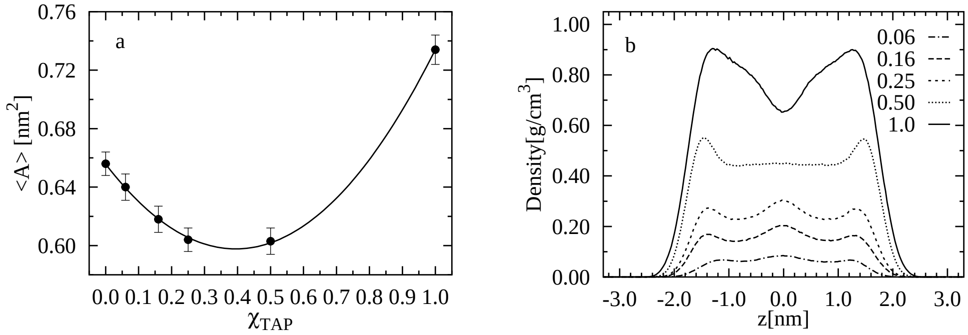

Figure 4.4: (a) Average area per lipid as a function of the DOTAP fraction (left). All the errors estimations in this study are calculated as standard deviation unless otherwise indicated. (b) Mass density profile of DOTAP for all simulated systems.

In Fig. 4.4a, we can easily observe a parabolic behavior of area per lipid as a function of cationic lipid fraction. Similar phenomenon was also obtained in a molecular dynamics study [152] as well as in experiments [160]. This lateral compression of the bilayers at modest amounts of cationic lipids, as suggested by a recent theoretical study [161], is due to the close packing of neutral lipids around cationic lipids resulting from the electrostatic attractions between the dipolar P-N vectors in DMPC lipids and the cationic DOTAP headgroups. At higher percentage of cationic lipids, the area per lipid expands because of the electrostatic repulsions between cationic lipids. This mechanism has been confirmed by our data analysis, as shown below.

Figure 4.4b shows the mass density profile of DOTAP lipids in all bilayers, where interdigitation [162] of DOTAP was observed, i.e., DOTAP lipids in one leaflet penetrate into another (see Fig 4.5). As one can see, this kind of interdigitation is more striking at lower TAP (from now on, TAP refers to DOTAP) fraction. This is due to the fact that the hydrocarbon chains of TAP lipids are four carbons longer than those of PC (from now on, PC refers to DMPC) lipids. At low TAP fractions, the effect of the global electrostatics is to confine the cationic TAP deep in the bilayer. As a result, the lipids, especially PCs on opposite leaflet, are repelled outward. This has been confirmed by the interdigitation analysis of PCs (data not shown). At higher TAP fraction, the interdigitation becomes weaker due to the repulsively entropic interactions between hydrocarbon core of bilayers. As revealed in our analysis, the total mass density at the bilayer center was well conserved and independent of the TAP fraction (data not shown)

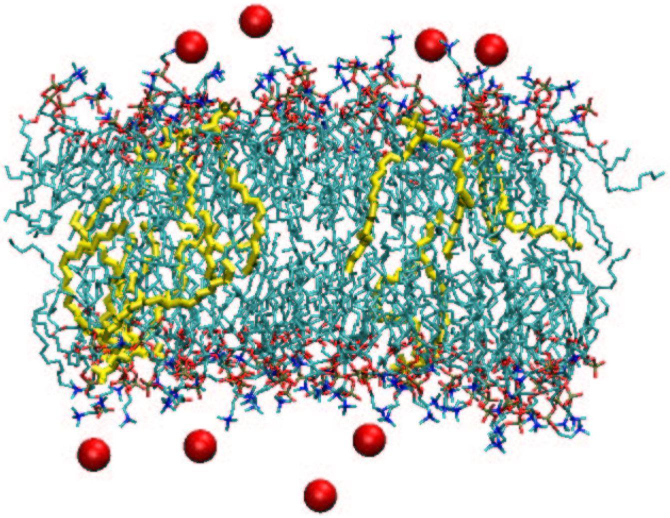

Figure 4.5: A snapshot of the DMPC/DOTAP lipid bilayer at TAP fraction of 0.06, where strong interdigitation of DOTAP lipids is shown. DOTAP lipids are shown in yellow. Cl^- are shown in red. Water molecules are not shown for clarity.

Figure 4.6a shows the evolution of vertical positions of different characteristic atoms with respect to the center of the lipid bilayers as a function of TAP fraction. We can see the average position of TAP nitrogen atoms exhibits an increase at higher TAP fraction due to less interdigitation of TAPs. The PC phosphorus atoms show an increase in their vertical positions which indicates changes of PC interdigitation. The PC nitrogen atoms go much higher and the distance between PC nitrogen atoms and TAP nitrogen atoms remains almost constant. With the increase in TAP fraction, the Cl^- ions move toward the membrane surface. As we can see, on average, the membrane/water interface moves toward the water phase at higher percentage of

TAP. This is due to, on one hand, the existence of longer TAP hydrocarbon chains. On the other hand, the cationic TAP headgroups strongly polarize the P-N vectors which reorientate upward to the water phase. Figure 4.6b shows the local protrusions of TAP lipids with respect to their PC neighbors at low TAP fraction (0.06), where the vertical positions of glycerol backbone are used for characterizing the vertical positions of PCs and TAPs. As one can see, the TAP lipids are located deeper than their PC neighbors. This is in agreement with experimental observations [159]. On the other hand, it also can be derived that the nearest PCs around TAPs are also located deeper compared to other PCs, since the relative vertical positions of TAPs go deeper when more neighboring lipids are considered. This observation has not been reported before.

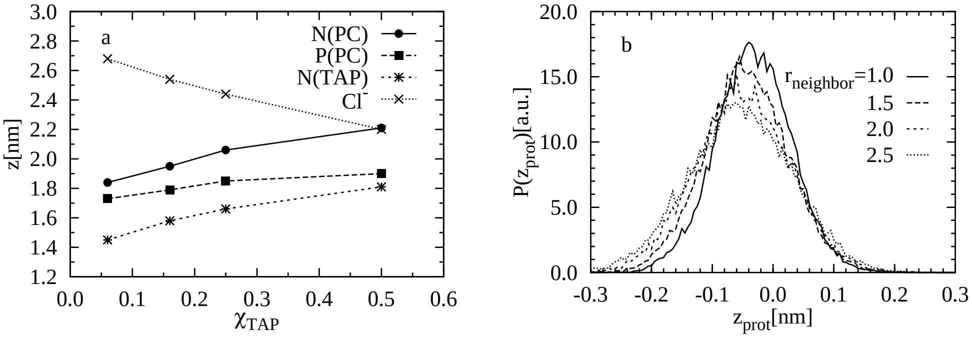

Figure 4.6: (a) Maxima of the density profiles for different characteristic atoms are shown as functions of TAP fraction. (b) Relative protrusions of TAPs with respect to neighboring PCs with different radii for neighbor searching, calculated at TAP fraction of 0.06.

Ordering of lipid acyl chains

Consistent with the behavior observed for the area per lipid, the order parameter of DMPC tails increases as the DOTAP fraction increases, i.e., a compression of the membrane is accompanied by enhanced ordering of non-polar acyl chains. The pure DOTAP bilayer shows the lowest ordering of all systems (not shown).

Compared to DMPC/DMTAP [152], the $|S_{\mathrm{CD}}|$ values of the hydrocarbon tails of DMPC, for DMPC/DOTAP system at same concentration of cationic lipids, are slightly lower throughout the whole chain. This is, probably, due to the unsaturated DOTAP hydrocarbon chains, whose two *cis* double bonds disturb the ordering of hydrocarbon core of the bilayers.

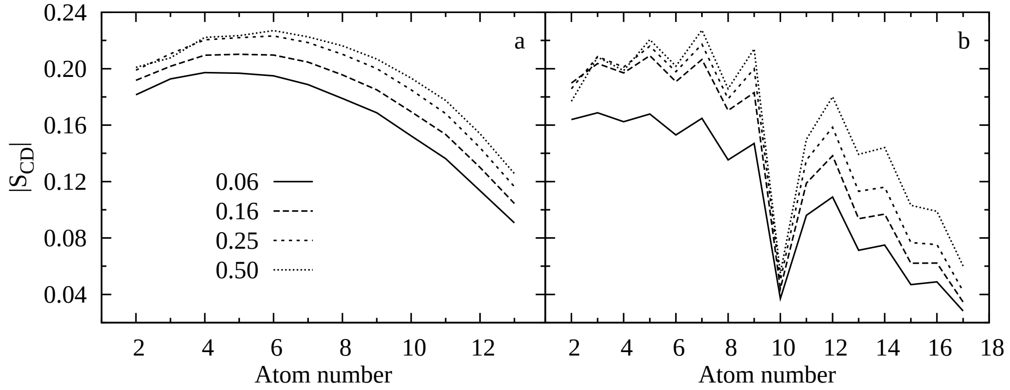

Figure 4.7: (a) Deuterium order parameter $|S_{\mathrm{CD}}|$ averaged over sn−1 and sn−2 chains for DMPC for all systems (left). (b) Deuterium order parameter $|S_{\mathrm{CD}}|$ averaged over the DOTAP sn−1 and sn−2 as a function of DOTAP fraction (right). For numbering of acyl chain atoms in DMPC and DOTAP, see Fig. 4.3.

Electrostatic interactions of PC and TAP headgroups

The headgroups of PC molecules possess dipole moments along the P-N vectors (see Fig. 4.3), the overall orientation of which greatly contributes to electrostatic potential across the bilayer [152]. In pure PC lipid bilayers, the dipolar headgroups form PC-PC charge pairs via electrostatic attraction between choline methyl groups of one PC molecule and phosphate or carbonyl oxygen atoms of another molecule [163]. Therefore, in pure PC bilayers, the headgroups align themselves almost parallel to the membrane/water interface. As cationic TAPs were introduced into the bilayer systems, a pronounced reorientation of the P-N vectors was found. As shown in Fig. 4.8a, the P-N vectors point outward to the water phase as the TAP fraction is increased. Moreover, the rotational motions of the P-N vectors are more constrained at higher TAP fraction, as indicated by measurements of the rotational autocorrelation functions of the P-N vectors (see Fig. 4.8b). This reorientation and constrained dynamics of the P-N vectors results from the strong electrostatic interaction between the P-N vectors and positively charged TAP groups, denoted as TAP-PC pairs (see Fig. 4.9a and 4.9b). In analysis, a PC-PC or TAP-PC charge pair is said to form if a PC or TAP nitrogen stay in the first coordination shell of a PC phosphorus atom.

Compared to the PC-PC charge pairs, the TAP-PC charge pairs are more energetically preferable, as suggested by the radial distribution functions of PC and TAP nitrogen atoms around PC phosphorus atoms, as shown in

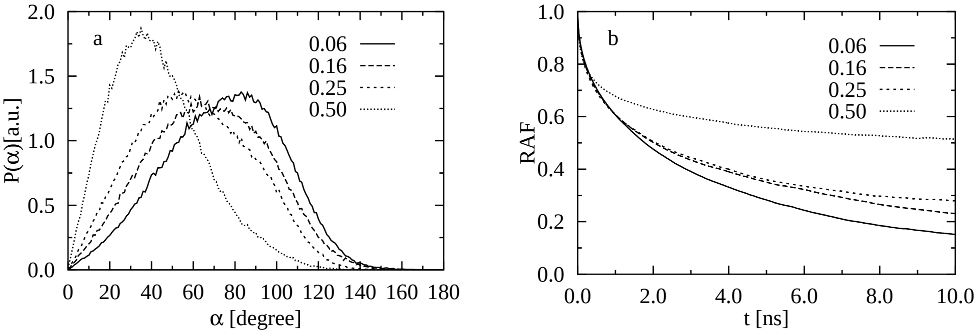

Figure 4.8: (a) Probability distribution function of the angle α between the P-N vector (PC) and the bilayer normal. (b)Rotational autocorrelation functions of the first Legendre polynomial for P-N vectors in the PC molecules at different TAP fractions.

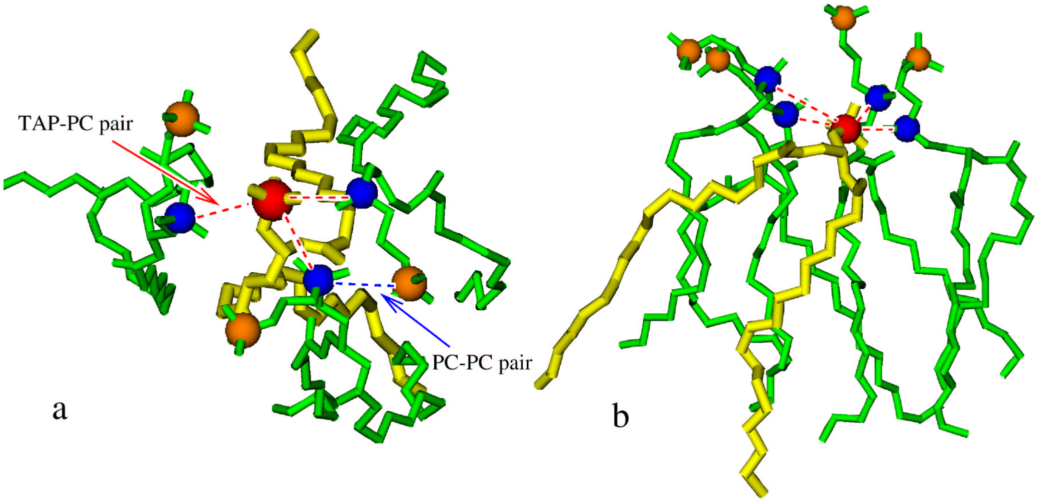

Figure 4.9: (a) A snapshot of a TAP forming charge pairs with three PCs. (b) A snapshot of a TAP lipid forming charge pairs with four PCs. The TAP nitrogen atoms are shown in red, while those in PC are shown in orange. The phosphorus atoms are shown in blue.

Fig. 4.10a. In a theoretical model, Levadny *et al.* suggested that, in mixed cationic bilayers at low TAP fraction, there should be PC clusters around individual TAP lipids and within these clusters, lipids are also suggested to pack closer to each other, which leads to the lateral compression of the bilayers.

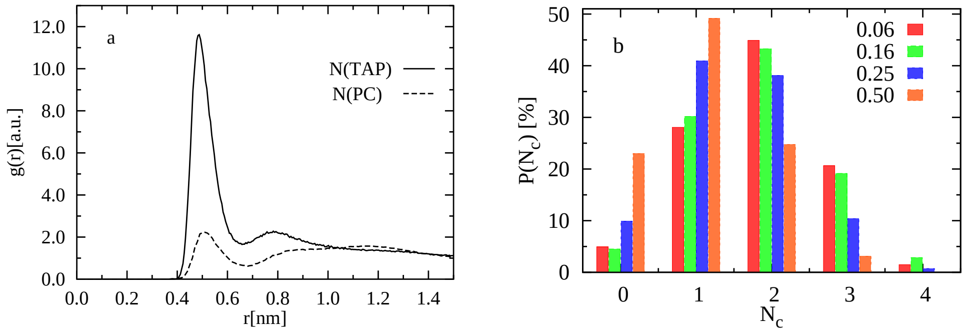

Figure 4.10: (a) Radial distribution functions of PC and TAP nitrogen atoms around PC phosphorus atoms at TAP fraction of 0.50. (b) Coordination number distribution of DMPC phosphorus atom around DOTAP nitrogen atom at different TAP fractions.

However, this model proposed by Levadny *et al.*, according to our observations, probably over-estimated the strength of the TAP-PC pairs (denoted as PC-TAP bond in their study) although they qualitatively or even quantitatively predicted the lateral compression of the bilayers as functions of TAP fraction. In their model, the TAP headgroup and its neighboring P-N vectors align in line, and, in low TAP fraction ($\chi_{\mathrm{TAP}} < 0.17$) PCs pack around TAP in hexagonal arrangement (i.e., coordination number of PC around TAP is 6). This is, however, not a proper scenario, according to our analysis of distribution of coordination number of PCs around TAPs, as shown in Fig. 4.10b. As one can see, even in a low TAP fraction of 0.06, where there is much excess of PCs, a majority of TAPs form charge pairs with one, two, and three PCs. Clusters containing five or more PCs are never found in all trajectories. This suggests that there exist a number of "small" clusters centered on TAPs, containing two or three PCs. Moreover, the TAP headgroups and their neighboring P-N vectors are not aligned in line even at very short distance. In our analysis, the average distance between PCs and TAPs is found to be shorter than that between PCs, as indicated by two-dimensional radial distribution functions between center of mass of lipids (see Fig. 4.11a). However, our data do not support existence of large number of PC clusters centered by TAPs at low TAP fraction.

This disagreement of the model with our results is due to a simplifica-

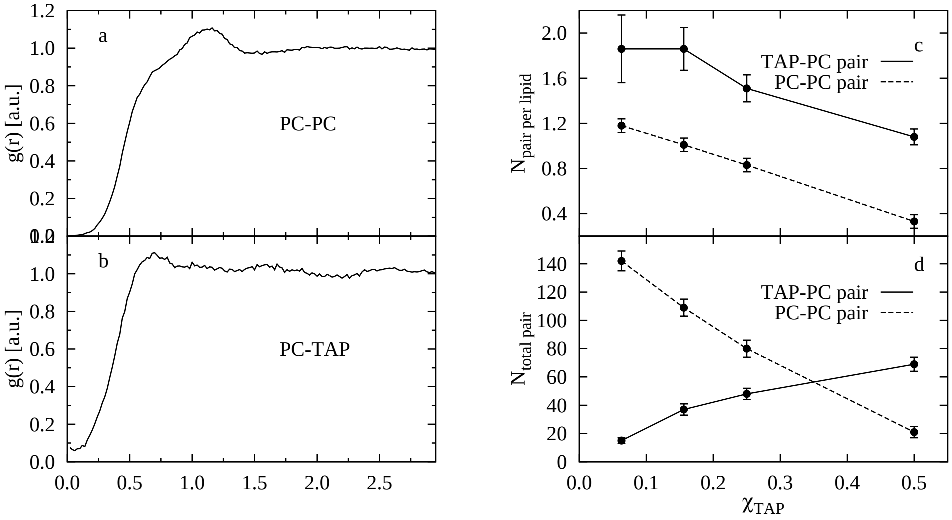

Figure 4.11: (a) Two-dimensional radial distribution functions of the center-of-mass positions between PC lipids at TAP fraction of 0.16. (b) Two-dimensional radial distribution functions of the center-of-mass positions between PC and TAP lipids at TAP fraction of 0.16. (c) Number of TAP-PC (per TAP) and PC-PC pair (per PC) as functions of DOTAP concentration. (d)Total number of TAP-PC and PC-PC pair as functions of TAP fraction.

tion of their theoretical description of bilayer systems, in which the effect of the aqueous solution was considered through a dielectric constant. In fact, at membrane/water interface, the water molecules are highly polarized by the membrane surfaces and greatly screen the direct electrostatic interactions between the TAP and PC headgroups. In the meantime, the negative charged counterions are not explicitly considered in their model, which could be another important factor that leads to large deviation from our molecular description.

In Fig. 4.10, we can see that the PC phosphorus atoms prefer to interact with TAP nitrogen atoms. Moreover, the second peak in the RDF of TAP nitrogen atoms suggests the existence of indirect interactions between PC phosphorus atoms and TAP nitrogen atoms such as those via water bridges [163]. We also calculated the total charge pair number and charge pair per lipid in all bilayers. Figure 4.11d shows the total charge pair number as a function of TAP fraction. We observed that the PC-PC charge pairs are replaced by the TAP-PC charge pairs gradually when TAP fraction is increased. This is due to not only the drop of PC fraction but also the ability of each PC to form charge pairs decreased at higher TAP fraction, as shown in Fig. 4.11c.

However, the ability for TAP to form TAP-PC charge pairs exhibits a non-monotonic decrease. We argue that this is probably due to the fact that the TAPs move upwards at higher TAP fractions (see Fig. 4.6a), leading to closer contacts between the TAP and PC headgroups. To verify this, we calculated the coordination number of phosphodiester (O_{phos}) and carbonyl oxygen atoms (O_{carb}) of PC around TAP nitrogen atoms. As shown in Fig. 4.12b, the coordination number of O_{phos} exhibits an increase at TAP fraction of 0.16 while the coordination number of O_{carb} decreased monotonically (see Fig. 4.12a). This observation indicates that the properties of hydrocarbon chains of lipids do affect the electrostatics at the membrane/water interface.

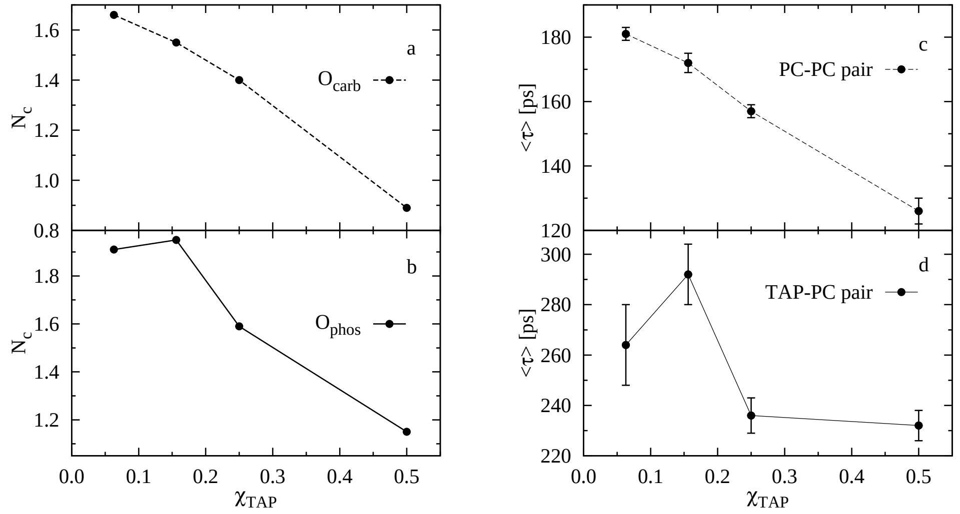

Figure 4.12: (a) Average coordination numbers of TAP nitrogen atoms with PC phosphodiester oxygen atoms (O_{phos}). (b)Average coordination numbers of TAP nitrogen atoms with PC carbonyl oxygen atoms (O_{carb}) as a function of the TAP fraction. (c) Average lifetimes of PC-PC charge pairs as a function of TAP fraction. (d) Average lifetimes of TAP-PC charge pairs as a function of TAP fraction. The errors are calculated as standard error estimates.

We also measured the average lifetimes of the PC-PC and TAP-PC charge pairs. In our analysis, short breaks of less than 20 ps were ignored. The results for the PC-PC and TAP-PC charge pairs are shown in Fig. 4.12c and Fig. 4.12d, respectively. It can be seen that the average lifetimes of the TAP-PC charge pairs are longer than those of the PC-PC pairs. In comparison with the lifetimes of the PC-PC charge pairs, which become shorter at higher

TAP fractions, those of the TAP-PC exhibit an increase at TAP fraction of 0.16. This observation is in agreement with the previous discussion about the closer contacts between the TAP and PC headgroups at TAP fraction of 0.16. The lifetime of the PC-PC charge pairs at TAP fraction of 0.06 is shorter than that in pure PC bilayer measured in a previous study [163]. However, we suggest this is due to the different definition and measuring criteria applied in their analysis.

In all DMPC/DOTAP mixture bilayers, the Cl^- ions are found to preferentially interact with the PC choline groups rather than those of TAPs. This is because, as also argued in the previous study of DMPC/DMTAP [152], the PC headgroups become more and more vertically oriented to the water phase, which makes the PC choline groups more accessible to the choline groups. Meanwhile, since the TAPs are located deeper in the bilayer, the negatively charged PC phosphate groups act as a screening barrier which partially prevents the Cl^- ions from approaching the TAP headgroups.

Electrostatic potential and water ordering

The electrostatic potentials across the bilayers are shown in Fig. 4.13. As the concentration of the cationic TAPs is increased, the electrostatic potential becomes more negative, accompanied by the disappearance of the bump located in the inner membrane/water interface. Similar behavior has been found in DMPC/DMTAP bilayers [152].

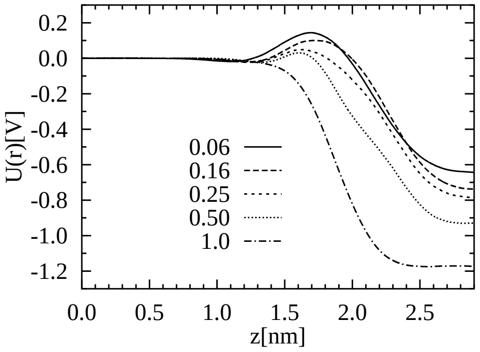

Figure 4.13: Electrostatic potential $V(z)$ across bilayers at different TAP fractions.

To analyze further the electrostatic potential across the lipid bilayer, we divided the potential into three parts: that induced by PCs, TAPs together with chloride ions, and water, respectively. In all DMPC/DOTAP mixture systems, positive values (5.3, 6.4, 6.6, and 5.8 V for systems at TAP fraction of 0.06, 0.16, 0.25, 0.50) were observed for the contributions of DMPC to the electrostatic potential. This property arises from the fact that the P-N vectors point out to the water phase on average.

The electrostatic potentials produced by the DOTAPs and Cl^- ions were found to be negative. In a pure TAP lipid bilayer, this potential was found to be $-5.9\,V$. In the mixture bilayer at TAP fraction of 0.5, this value was found to be 8.8 V, which is bigger than that in pure TAP bilayer. This is due to the fact that the Cl^- ions and TAP headgroups fall apart on average, due to the existence and reorientation of the P-N vectors of PCs.

The electrostatic potentials due to water is almost a mirror image of the lipid (together with Cl^- ions) potentials for all system and whether they are positive or negative depends on the constituents of the lipid bilayer (see Fig. 4.14a). This means that the charge density relating to the lipids and the Cl^- ions is almost completely compensated by the opposite net charge density due to the orientation of the water dipoles, as is to be expected from high dielectric medium [164].

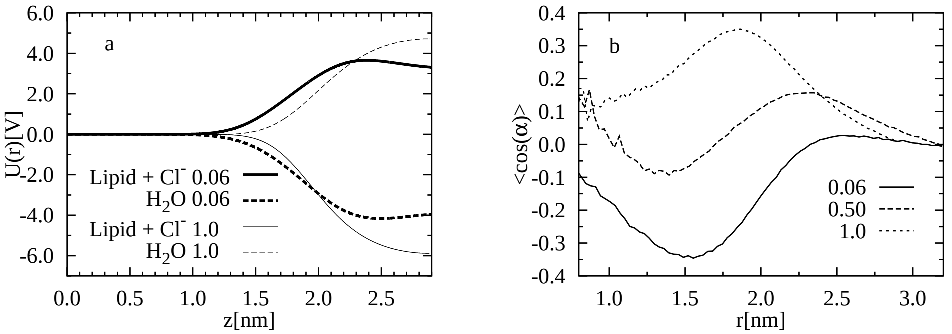

Figure 4.14: (a) Electrostatic potential $V(\mathrm{z})$ across bilayers at different DOTAP fractions due to lipid (together with Cl^- ions), and water. (b) Projection of the average water dipole onto the interfacial normal, where $z = 0$ corresponds to the center of the bilayers.

In a pure DMPC system [152], the overall negative value is found for the average water dipole due to the P-N vectors pointing outward to the water phase. With the introduction of cationic TAPs, a positive bump shows up on the water dipole curve due to the existence of a diffuse double layer formed by TAPs and Cl^- ions (see Fig. 4.14b). In the pure DOTAP bilayer, overall positive value is found for the average orientation of water dipoles, which has been discussed previously [152].

4.3.4 Summary and conclusion

In this study, we have performed atomistic molecular dynamics simulations to study the electrostatic and structural properties of mixed lipid bilayers consisting of cationic DOTAP and zwitterionic DMPC. We studied the electrostatic interactions within the membrane/water interface, mainly focusing on charge pairs between DOTAP and DMPC lipids. In all DMPC/DOTAP mixture bilayers, a great number of TAP-PC and PC-PC charge pairs are found, which break and re-form dynamically. These charge pairs lead to the existence of some lipid clusters containing DMPCs around DOTAP at low TAP fraction. However, in comparison with the theoretical model proposed by Levadny*et al.*, our results suggest much weaker electrostatic interactions between the PCs and TAPs, as indicated by the size and occurrences of the clusters. We argue that this discrepancy arises from the fact that their model is actually based on a mean field description of the membrane/water interface.

We also analyze the evolution of system dimensions of bilayer systems as a function of the TAP fraction. A strong interdigitation of the DOTAPs is found for all DMPC/DOTAP mixture bilayers. This results from the electrostatics within the membrane/water interfacial region, which confine the longer acyl chains of DOTAPs deep inside the bilayers. On the other hand, the constituents of lipid acyl chains, in reverse, affect the interfacial electrostatics, which has been confirmed by the effects of the longer acyl chains of DOTAPs on the life-time of the TAP-PC charge pairs.

The introduction cationic DOTAP lipids into DMPC bilayer membrane is suggested ,by our analysis, to lead to changes of elastic properties of the membrane. This is because, first, the longer and unsaturated hydrocarbon chains of DOTAP greatly disturb the more ordering hydrocarbon core of the DMPC bilayer, as suggested by our analysis about the order parameters and interdigitation of lipids. On the other hand, the attractive interactions between the cationic TAPs and PCs is observed to induce some local dimensional changes (see Fig. 4.6b). These two factors are supposed to induce changes in elastic properties of the bilayers. However, the microscopic boundary sizes of our systems limit us to performing such an investigation based on the Helfrich free energy calculations. In a recent study [70], molecular dynamics simulations, based on a simple coarse-graining model, were performed for a mixed bilayer consisting of neutral lipids, and observed the chain length effects on the elastic properties of membranes. Similarly, further computational studies based on coarse-graining models could possibly reveal the chain length effects on the elastic properties of charged membrane systems.

Next, we will report our computational study about an anionic POPG membrane.

4.4 Anionic POPG membrane

4.4.1 Introduction

Phosphatidylglycerols (PGs) are among the most abundant lipids in nature. In higher plants, they constitute about 20 – 30% of lipids [165]. They are also one of the major constituents of bacterial membranes [166]; mixed phosphatidylglycerol/phosphatidylethanolamine (PE) lipid bilayers have been used as models for bacterial membranes [167–170]. It is also noteworthy that phosphatidylglycerols constitute up to 80 % of membrane lipids of *Staphylococcus aureus*, a common human pathogen with its methicillin-resistant strain (MRSA) – the so-called hospital bacteria – being a serious problem in hospitals around the world. In contrast, the concentration of PG lipids in animal cell membranes is low. In red blood cells PGs constitute about 2 % of all phospholipids [171]. While being less common in animal membranes, they are present in mitochondria and some tissues [166]. From the physical point of view, phosphatidylglycerols, together with phosphatidylserine (PS) and cardiolipin, are anionic, the former two carrying a unit negative charge, while the latter being divalent under physiological conditions.

The non-zero net charge of PGs makes them different from commonly studied zwitterionic (neutral) lipids. Since direct electrostatic interactions between charged species are rather strong, PGs, as well as other charged lipids, are considered as membrane stabilizers and destabilizers [172] and are believed to play an important role in controlling membrane-peptide/protein interactions. For this reason, PGs have been suggested as one of the possible components in immunoliposomes, generic drug delivery vehicles [173].

Given the abundance of phosphatidylglycerols in nature, it is somewhat surprising that, to the best of our knowledge, there has been only one atomistic computational study of pure PG lipid bilayers [174] focusing on the hydrogen bonding between the lipids. All related simulation studies to date have dealt with mixtures of PGs with other lipids [167, 170] or with PG monolayers at the air/water interface [175]. On the experimental side, pure POPG bilayers, or POPG mixed with PC at high concentrations, have been studied (to our knowledge) only by Cowley *et al.* [176] in the 1970's and more recently by Pozo-Navas *et al.* [177, 178]. The phase behavior [179, 180] and various aspects of the structure-function relationship of POPGs in phosphatidylethanolamine bilayers [172, 181–184] have been experimentally characterized, though.

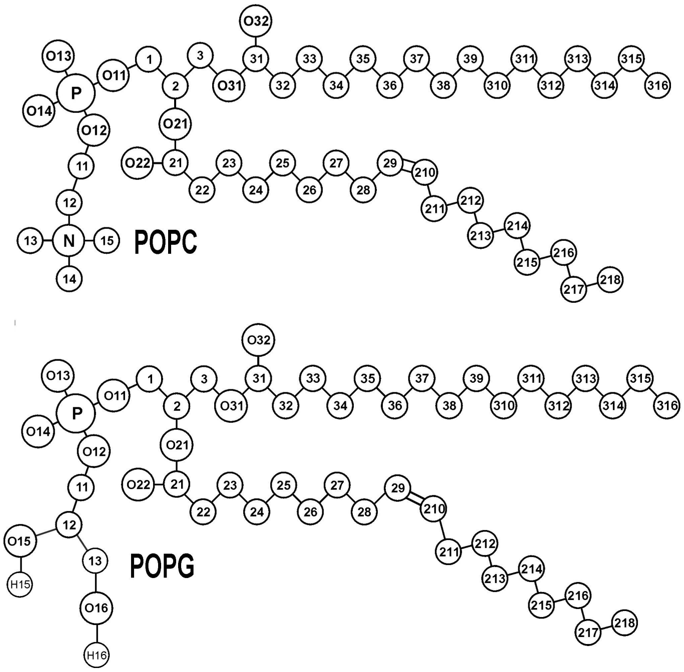

Figure 4.15: Chemical structures and the numbering of atoms of POPC and POPG lipids used in this study.

In this work we employ atomistic MD simulations to gain a thorough understanding of the properties of PG-rich membranes through a systematic comparison with corresponding PC bilayers. We focus on the structural and electrostatic properties of single-component palmitoyloleoylphosphatidylglycerol (POPG) lipid membranes. This is needed to establish the fundamental molecular and atomistic level physical origin of the observed phenomena. This knowledge should be useful also in interpreting experimental findings and it offers a possible explanation as to why nature has chosen to use charged lipids structures such as bacterial membranes.

4.4.2 System preparation

The starting structure of a POPG bilayer was prepared using an equilibrated POPC bilayer [156]: the choline moieties of POPC lipids were replaced with the glycerol groups. Since the PG headgroup exhibits chirality with C12 [185, 186] (see Fig. 4.15 for atom labeling) as a chiral center, equal numbers of *D*- and *L*-POPG lipids were created, leading to a lipid bilayer system with neutral chirality (racemic). To ensure charge neutrality, sodium ions were introduced by replacing a number of water molecules by sodium ions such that the system became charge neutral. After initial energy minimization, a short 10 ps run in the NVT ensemble was performed to remove unphysical voids. The resulting POPG system was simulated for 150 ns. By analyzing the time evolution of the area per lipid and the coordination of Na^+ counterions with lipids and water, we concluded that the system had equilibrated within 70 ns, see Fig. 4.16. The time range from 70 to 150 ns was therefore used for analysis.

4.4.3 Simulation results

Area per lipid

The average area per lipid, $\langle A \rangle$, is perhaps the most widely used quantity to characterize lipid bilayer systems, since it affects a variety of physical processes such as lateral diffusion, membrane elastic properties, and permeation. The time evolution of the area per lipid is shown in Fig. 4.16. The long equilibration time visible in the figure is mainly due to the slow kinetics associated with the binding of counterions with the charged POPG lipids, and in part due to hydrogen bond formation among the lipids. Similar findings have also been made in simulations of anionic phosphatidylserine bilayers [187] and in bilayer simulations under the influence of salt [153,188–190]. For the average area per lipid in a POPG bilayer we obtained $\langle A_{\mathrm{POPG}} \rangle = 0.530 \pm 0.006\,\mathrm{nm}^2$. This is a remarkably small number compared to typical values in corresponding zwitterionic lipid systems. For example, for a POPC bilayer studied in this work we found $\langle A_{\mathrm{POPC}} \rangle = 0.658 \pm 0.009\,\mathrm{nm}^2$ at the same temperature. Sphingomyelin bilayers in turn have yielded average areas per lipid of the order of $0.52\,\mathrm{nm}^2$, and the lipid hydrocarbon chains in these systems are

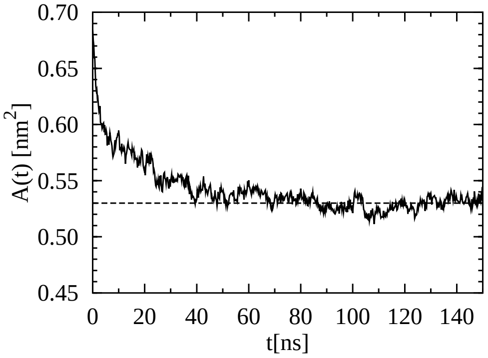

Figure 4.16: Time evolution of the area per lipid for the POPG bilayer. Dashed line shows the average value in equilibrium, $\langle A \rangle$.

known to be highly ordered. Similar enhanced ordering is therefore expected for POPG too (not shown).

To our knowledge, there are no experimental estimates for the average area per lipid in single-component POPG bilayers. A comparison to previous related simulations is possible. Murzyn *et al.* [170] used the Voronoi tessellation technique to extract the average area per lipid from simulations of a POPE / POPG mixture. They reported a value of $0.628 \pm 0.003\,\mathrm{nm}^2$ for the average area per POPG, which is considerably larger than the value found in our work. One has to note, however, that the result by Murzyn *et al.* cannot be directly compared to our findings. This stems from the fact that they applied the Voronoi tessellation technique to a binary system, in which there is no unique way to decompose the free area (volume) among the different lipid components. Hence the areas of two-dimensional Wigner-Seitz cells in binary systems do not correspond to the area per lipid measured in single-component lipid bilayers. This issue has been extensively discussed in computational studies of cholesterol in phospholipid bilayers [191–194] and also in experiments on mixtures of non-sterol natural lipids [195].

A better, but also indirect comparison can be provided by MD simulations of pure phosphatidylserine (POPS) bilayers [187]. Although headgroups of POPG and POPS lipids have different chemical structures, both of these lipids are anionic under physiological conditions. Mukhopadhyay *et al.* obtained $0.55 \pm 0.01\,\mathrm{nm}^2$ for the average area per POPS under simulation conditions similar to those employed in the present study – close to $0.53\,\mathrm{nm}^2$ found here for a POPG bilayer. These findings are also in agreement with Cowley *et al.* [176] who studied PC/PG bilayers at different concentrations under varying hydration conditions.

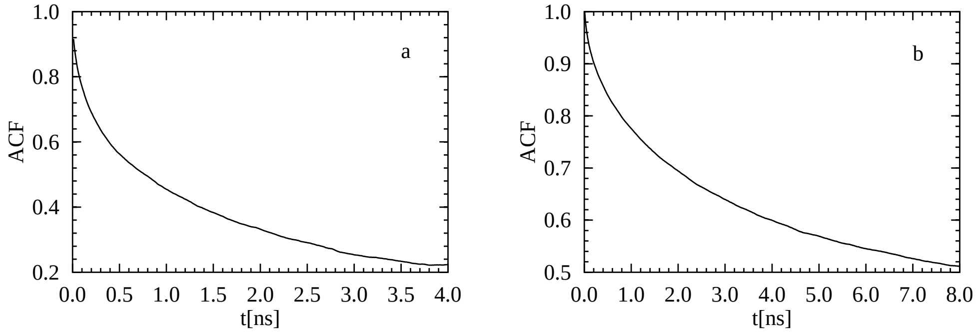

Figure 4.17: (a) Autocorrelation function for individual POPC Voronoi areas. (b) Autocorrelation function for individual POPG Voronoi areas.

We also computed the autocorrelation function to measure the characteristic time scales for area fluctuations of POPGs, as shown in Fig. 4.17b. As expected on the basis of the above discussion, they turned out to be much longer than those observed for POPC bilayers [156] shown in Fig. 4.17a. The above observation indicates that an anionic POPG bilayer is less fluid than one would naïvely expect [179]: its densely packed structure, which seems to be counterintuitive at first sight, is caused by tight binding of anionic lipids through relatively stable ion bridges, which we will discuss in detail below.

Density profiles

The maxima of the mass or electron density profiles are often used to estimate the thickness of the bilayer [170, 196, 197]. The density profiles of the present system are shown in Fig. 4.18a. As in previous studies [197], we considered the distance between the average positions of phosphorus atoms in the two leaflets of a lipid bilayer. That distance computed from the electron density profile yielded 4.39 ± 0.02 nm for the phosphorus-phosphorus distance $d_{\mathrm{P-P}}$. The result is in line with $d_{\mathrm{P-P}} = 4.26 \pm 0.06$ obtained in a previous simulation study of a POPG bilayer at 310 K [174].

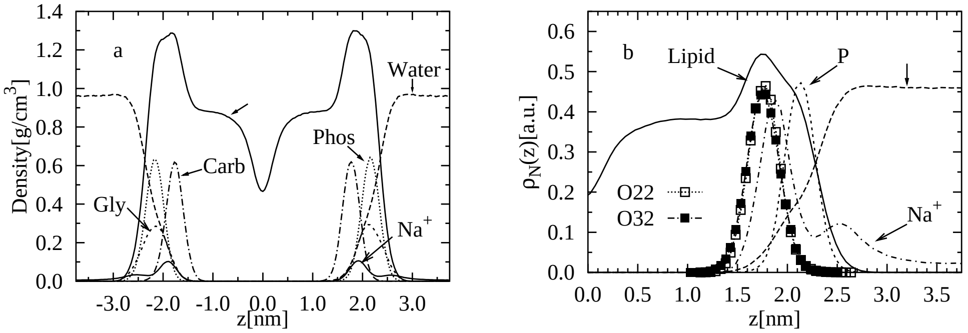

Figure 4.18: (a) Component-wise density profiles across the bilayer as a function of distance from the membrane center ($z = 0$). Gly: the glycol group (H16, O16, C13, C12, O15, H15); Phos: the phosphate group (O11, O12, O13, O13, P); and Carb: the carbonyl ester group (C21, O21, O22, C31, O31, O32). (b) Scaled number densities for various constituents of the POPG system. The number density of lipids was not scaled, whereas the densities of water, phosphorus atoms, O22, O32, and Na^+ ions were scaled by dividing them by 70, 10, 10, 10, and 7, respectively. The bilayer center was at $z = 0$.

The maximum of the mass density profile of POPG lipids turns out to be located at the average position of the ester groups instead of the phosphate groups as has been found for phosphatidylcholine bilayers [156]. The most remarkable feature is the distribution of Na^+ ions characterized by two peaks in the interface region, see Fig. 4.18b. The first (main) peak is located at ≈ 1.9 nm from the bilayer center and overlaps with the peak due to the POPG carbonyl ester groups. Elmore has recently made a similar observation [174] in his simulation. The second, much smaller peak is at ≈ 2.65 nm. Further analysis shows that this peak corresponds to Na^+ ions mainly located in the water phase, close to the membrane but beyond the phosphate groups, although the distribution of Na^+ is strongly affected by the surface potential of the negatively charged surface of the POPG bilayer. Hence the positively charged sodium ions tend to avoid being in close contact with the negatively charged phosphate groups, and instead prefer interactions with the ester groups.

The peaks of the density profiles of phosphodiester oxygen atoms (O13, O14), hydroxyl oxygen atoms O16, and O15 (see Fig. 4.18a) are located at $\approx$ 2.2 nm, 2.05 nm, and 2.0 nm, respectively. When these numbers are compared to the distribution of Na^+ ions, they suggest that sodium ions interact more favorably with ester groups rather than phosphodiester moieties. Meanwhile, sodium ions corresponding to the second, smaller peak of the distribution ($\approx$ 2.65 nm) are not bound to lipids. We will return to this issue and discuss it in detail below. Due to strong electrostatic interactions, all the Na^+ ions stay near lipid headgroups and interact with various oxygen atoms. Yet the mutual electrostatic repulsion between the Na^+ ions, together with their thermal motion, and energy compensation from hydration, competes with the tendency of the sodium ions to reside close to the headgroups. The two effects together lead to the existence of the broad second peak in the distribution of the Na^+ ions.

Hydrogen bonding

Experimental observations have suggested that the hydroxyl group of a phosphatidylglycerol lipid has the potential to form both intra- and inter-molecular hydrogen bonds [198].

On average, we found that O16 forms ~ 0.15 intra-molecular and ~ 0.47 inter-molecular hydrogen bonds with various lipid oxygen atoms per POPG molecule. The inter-molecular hydrogen bonds between the O16-H16 groups and carbonyl groups are the most abundant hydrogen bonds found in our study. We will discuss this issue in more detail below. Table 4.1 summarizes the average numbers of intra- and inter-molecular hydrogen bonds.

Interactions of Na^+ ions with /membrane/water interface

a. Radial distribution functions and coordination numbers

H-donor	H-acceptor	Inter-molecular	Intra-molecular
O15	O12	-	1.00 ± 0.01
O16	O11	0.06 ± 0.02	-
O16	O12	0.01 ± 0.01	0.02 ± 0.01
O16	O13, O14	0.07 ± 0.02	-
O16	O15	0.05 ± 0.02	0.05 ± 0.02
O16	O16	0.02 ± 0.01	-
O16	O21	0.07 ± 0.01	0.04 ± 0.01
O16	O22	0.14 ± 0.02	0.02 ± 0.01
O16	O31	0.01 ± 0.01	0.01 ± 0.01
O16	O32	0.05 ± 0.02	0.01 ± 0.01

Table 4.1: Average number of inter-molecular and intra-molecular hydrogen bonds in a POPG lipid. The errors given were standard error estimates. See Fig. 4.15 for atom labeling.

Figure 4.19a shows the radial distribution functions (RDFs) of various oxygen atoms (including inter-molecular and intra-molecular parts) with the hydrogen atom H16 in the POPG headgroup. The results for H15 are not shown since it forms intra-molecular hydrogen bonds with the phosphoether oxygen atoms. In Fig. 4.19a, the first minima in the RDF for all the carbonyl and phosphodiester oxygen atoms are located at $\sim 0.24\,\mathrm{nm}$, indicating hydrogen bonding with H16 hydrogen atoms. This confirms inter-molecular hydrogen bonding in the POPG bilayer.

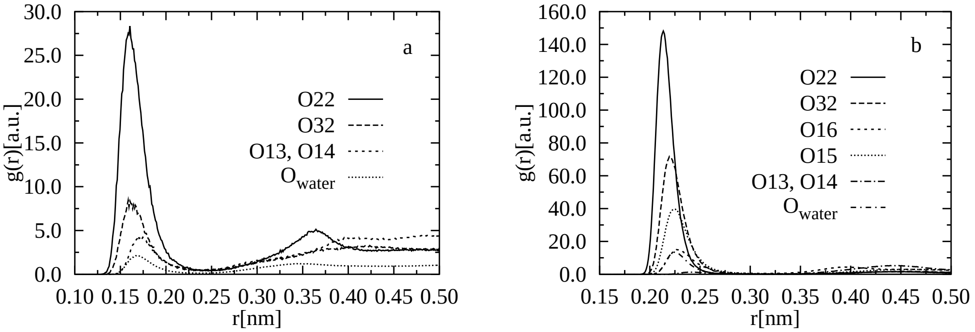

Figure 4.19: (a) Radial distribution functions of various oxygen atoms with the hydroxyl hydrogen H16. (b) Radial distribution functions of various oxygen atoms with Na^+ ions. See Fig. 4.15 for atom labeling.

The distribution of Na^+ in Fig. 4.19b suggests that a large amount of sodium ions are located in the ester region of the membrane/water interface, rather than in the phosphate region. Similar behavior has been found in POPS bilayer [199] and POPC bilayer [188] simulations in presence of NaCl. Clearly, there are prominent peaks with oxygen atoms O22 and O32 associated with the ester bonds, followed by O15 in the glycerol part of the headgroup. The remaining peaks related to O16 (also part of the glycerol group) and oxygen atoms O13 and O14 in the phosphate group are considerably less significant. This is in agreement with the coordination number analysis about different types of oxygen atoms around Na^+ ions, as shown in Tab. 4.2.

Oxygen type	N_c
O22	0.91
O32	0.60
O15	0.40
O16	0.19
O13, O14	0.04
O_{water}	3.36

Table 4.2: Coordination number of different types of oxygen atoms around Na^+ ions. O_{water} denotes water oxygen atoms.

To get a more detailed view on how Na^+ ions interact with different charged groups, in Fig. 4.20a we show the coordination numbers of Na^+ ions with various oxygen atoms as a function of the distance from the bilayer center.

The total coordination number shows a small increase, from ≈ 5.0 deep inside the lipid bilayer to ≈ 5.7 in the aqueous phase. The coordination numbers of Na^+ ions with lipid oxygen atoms show a maximum in the ester region of the membrane/water interface, indicating strong interactions between Na^+ ions and carbonyl groups. Due to the binding of sodium ions to the membrane, water molecules are squeezed out from the first coordination shell.

In previous discussion, we indicated that the density profile of sodium ions was characterized by two peaks in the membrane-water interfacial region. Figure 4.20b elucidates the origin of that behavior: the first peak in the density profile of sodium ions around $z \approx 1.9$ nm is due to ions bound to lipid oxygen atoms, and especially those bound to the oxygen atoms in the ester groups. The second peak at $z \approx 2.65$ nm, in turn, arises from those sodium ions that are not bound to any lipid oxygen atoms but rather are confined to water molecules in the vicinity of the membrane-water interface.

b. Ion bridges and ion-lipid clusters

Next, we will study the binding of Na^+ ions with lipids, and how ions may connect two or more lipids to each other by an “ion bridge”. This mechanism

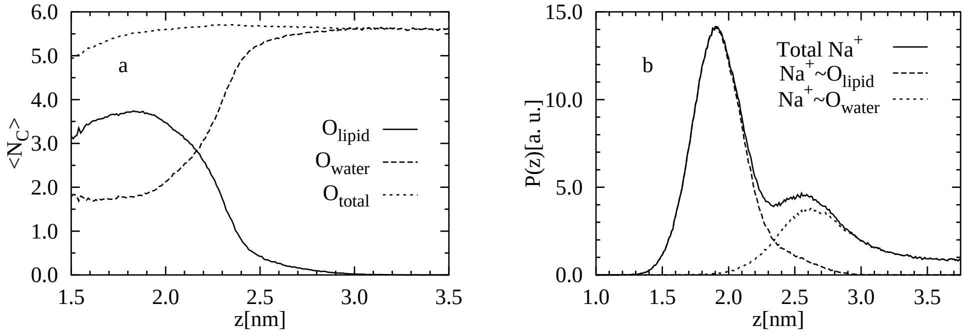

Figure 4.20: (a) Average coordination numbers of Na^+ ions with various lipid oxygen atoms, water oxygen atoms, as well as the total coordination numbers (including contributions from all oxygen atoms in POPG) as a function of the distance from the bilayer center. (b) Distributions of Na^+ bound and unbound to lipid oxygen atoms as functions of distance from the bilayer center.

enables cluster formation which increases stability and rigidity of the bilayer. The term "ion bridge" refers to the case in which two lipids bind to each other via a Na^+ ion. To characterize the existence of ion bridges, we define an ion-lipid bond to occur when the carbonyl oxygen is within a distance of 0.33 nm from a Na^+ ion, which is the radius of the first shell of Na^+ ions.

Here, we only define lipid carbonyl oxygen atoms (O22, O32) instead of all lipid oxygen atoms as binding sites available for ion bridges [200]. This is justified since the bonding between Na^+ ions and carbonyl oxygen atoms is much stronger compared to the interactions between Na^+ ions and other lipid oxygen atoms. These ion bridges constitute the majority of all interactions between Na^+ ions and lipids.

When analyzing the trajectory, we found, on average, 193 ± 5 ion-lipid bonds (in the present model of 128 PGs and 128 sodium ions), involving 63 % of Na^+ ions and 97 % of lipids. The distribution functions of lipids around Na^+ ions and Na^+ ions around lipids are shown in Figs. 4.22a and 4.22b.

As we can see, the majority of Na^+ ions bind to two or three lipids while most of the lipids bind to one or two Na^+ ions with almost equal probabilities (see Figs. 4.22a and 4.22b). We observed that, although each lipid has two binding sites for ion-bridging, the cases with an individual Na^+ ion binding to two carbonyl oxygen atoms within the same lipid are rare.

As seen above, an ion often binds to more than one lipid. That makes it possible for the lipids to form larger connected clusters in which the lipids are linked to each other by ion bonds. We define such a continuous and connected

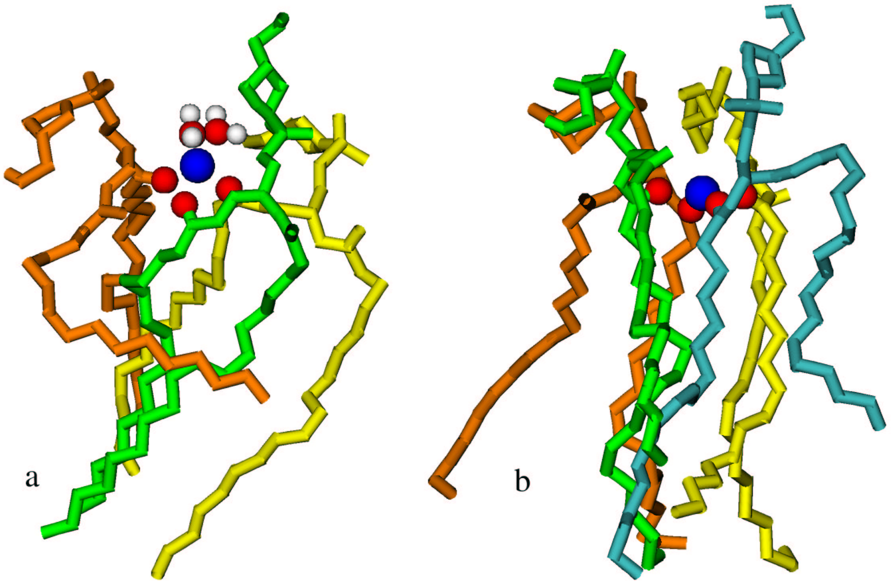

Figure 4.21: Snapshots of lipids binding to Na^+ ions. The cases shown here correspond to the binding of (a) three lipids and two water molecules with a Na^+ion and (b) four lipids with a Na^+ ion.

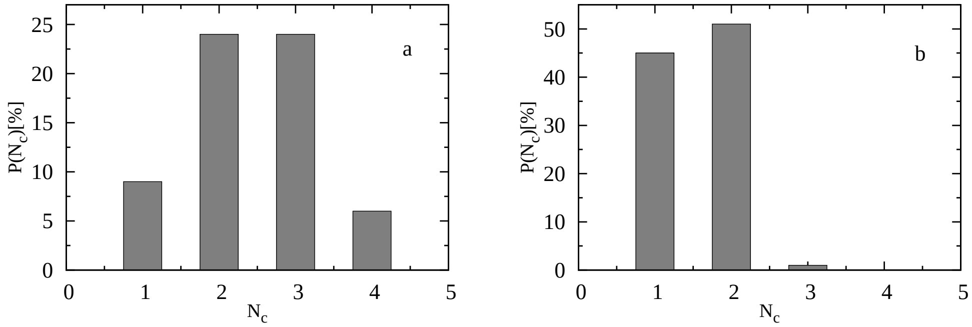

Figure 4.22: (a) Distribution of coordination number of lipids around Na^+ ions. (b) Distribution of coordination number of Na^+ ions around lipids. Only carbonyl oxygen atoms in lipids are considered in the calculation of coordination between lipids and Na^+ ions.

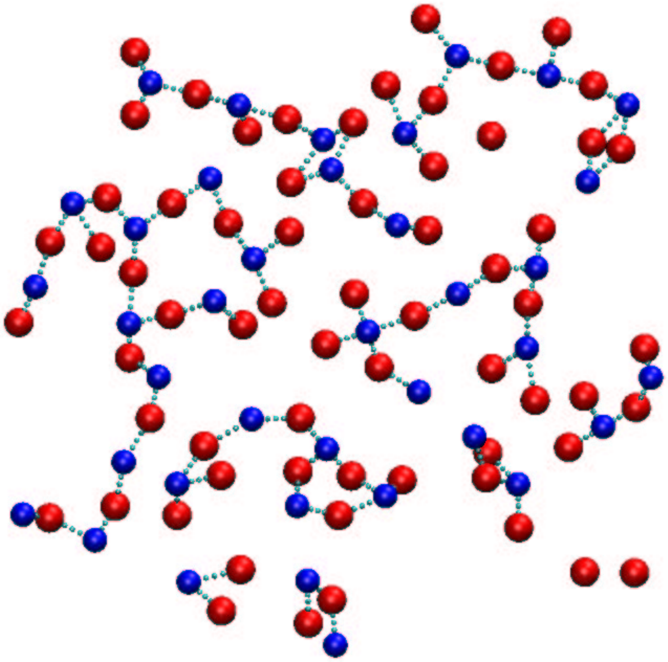

Figure 4.23: A snapshot of a typical configuration (one leaflet) demonstrating the existence of clusters. Each lipid (red) is represented by the average position of its two carbonyl oxygen atoms. An ion-lipid bond (green dots) appears between a lipid and a Na^+ ion (blue).

network as an *ion–lipid cluster.* Figure 4.23 shows a typical configuration of an ion–lipid cluster. We also studied the distribution of the cluster sizes as shown in the inset in Fig. 4.24. Although smaller clusters appear frequently, most of the lipids belong to larger clusters. It can be easily imagined that the existence of clusters has an effect on the dynamics of the whole bilayer since the robust ion bridges force the lipids to move collectively. This suggestion is supported by the strong correlation between the evolution of the area per lipid and the number of clusters. That is shown in Figs. 4.16 and 4.24. The slow process of the formation and breaking of the ion-lipid bonds is likely to be the key factor that makes the equilibration of the POPG bilayer slow.

Water orientation

The orientation of water dipoles as a function of the distance from the bilayer center is presented in Fig. 4.25a. Due to the negative surface charge of the POPG bilayer, interfacial water is highly polarized and distinctly different from the POPC case. While in POPC there is a single minimum in the inter-

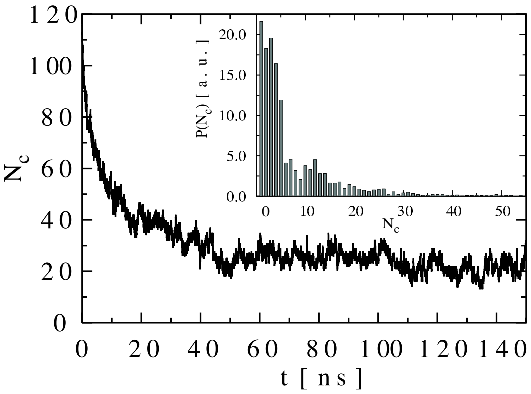

Figure 4.24: Time evolution of the number of clusters during the whole simulation. Inset: Size distribution of clusters. The cluster size is defined by the number of lipids it contains, e.g, a cluster of size 1 may or may not contain a Na^+ ion, while clusters of size more than 1 always contain Na^+ ions.

facial region, the ordering of water within the POPG bilayer is characterized by a rather deep minimum around 2.4 nm and a broad maximum around 1.9 nm. The water orientation profile reflects the total charge density profile of the POPG/water/ion system shown in Fig. 4.25b.

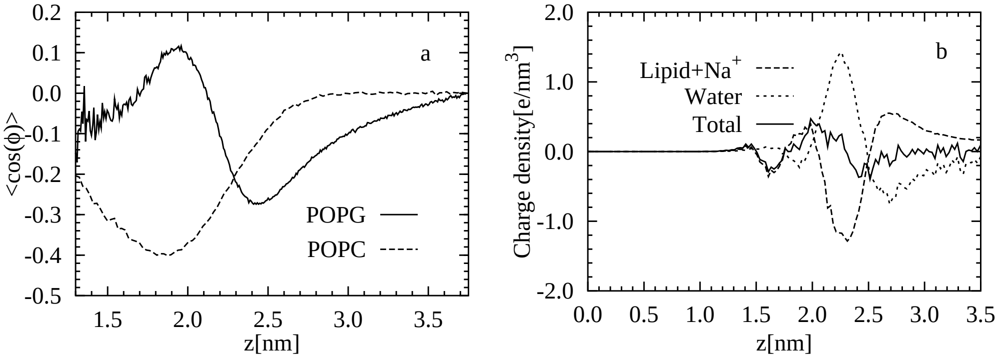

Figure 4.25: (a) The average cosine of the angle ϕ between the water dipoles and the outward bilayer normal. (b) Charge density profiles due to POPG with Na^+ ions, water, and the total charge density profile. The profiles are shown as functions of the distance from the bilayer center.

As Fig. 4.25b shows, ordering of water compensates the excess local charge carried by lipids and Na^+ ions. This is in agreement with observations for an anionic POPS lipid bilayer [201].

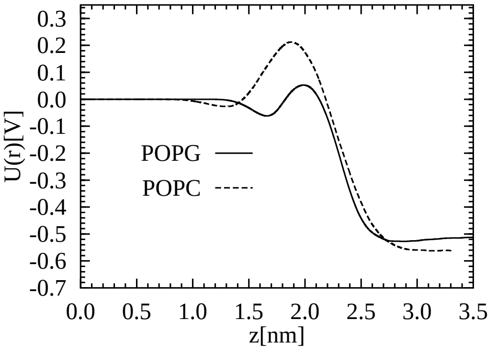

Figure 4.26: Electrostatic potential across the bilayer as a function of distance from the bilayer center.

Electrostatic potential

To a large extent, the electrostatic potential determines the permeability of ionic solutes through the lipid bilayer [202]. In our analysis, the electrostatic potential across the bilayer is calculated using the method introduced before.

Figure 4.26 shows that the electrostatic potentials for POPG and POPC bilayers differ especially in the inner side of the interface region. The potential barrier in POPG is much lower which means that it is easier for a positively charged ion to migrate across the interface zone. This difference is expected to arise from a number of factors related to the charge density profiles of a POPG bilayer, which are shown in Fig. 4.25b. First, for a POPG bilayer, the net negative charge carried by the phosphate group, along with the positive charge carried by the non-uniformly distributed Na^+ ions, resulting in a strong surface potential, plays an important role. The dipole potential due to the orientation of ester carbonyls, is another potential source. Furthermore, the oriented water also gives an important contribution.

4.4.4 Discussion

We have presented results from an extensive molecular dynamics study of a negatively charged POPG lipid bilayer. A zwitterionic POPC bilayer has been used as a reference. Thus far, to our knowledge, previous computational studies of PG systems [170, 174, 175] have been rather limited in scope and focused on hydrogen bonding [174], mixtures of PG with POPE [170] or studies of PG molecules in monolayers [175]. Here, we have presented a systematic study of the structural properties of a POPG bilayer with a special attention to the role of electrostatics in PG bilayers.

Our studies revealed that PG headgroups have a rather weak intra-molecular hydrogen bonding ability. We observed hydrogen bonds mainly between the hydroxyl-1 (O16-H16) groups and carbonyl groups. This is in agreement with infrared spectroscopy analysis [198]. Existence of this hydrogen bonding was suggested to prevent the interactions between hydroxyl-1 O16-H16 groups and Na^+ ions. The fact that the PG headgroup is not strongly hydrogen bonding is emphasized by the observation that in a mixture with POPE [170], the number of intra-molecular bonds is three times smaller than what we have observed here. That is mainly due to competition for hydrogen bonding sites with the strongly hydrogen bonding PE group [170].

It seems that the weakening of hydrogen bonding of the PG headgroup is due to the strong direct electrostatic interactions caused by the negative charge within the POPG headgroup. A similar conclusion has been suggested for anionic POPS bilayers [187]. On the other hand, the hydroxyl-2 (O15-H15) group is involved with high affinity in intra-molecular hydrogen bonds with the phosphate oxygen O12. The existence of the intra-molecular hydrogen bond O15-H15-O12, however, has not been reported in experimental studies thus far (to our knowledge). Infrared spectroscopy studies would be useful to investigate the existence and stability of this hydrogen bond.

The main finding in our study is that while the inter-molecular hydrogen bonds are rare, the strong and frequent interaction between ions and PG carbonyl oxygen atoms seems to be the most important factor determining the order of hydrocarbon chains and membrane surface area. About 60 % of Na^+ ions are involved in inter lipid interactions in terms of ion-bridges between the lipids. The resulting interaction network where lipids are connected through ion-bridges, results in ion-lipid clusters whose sizes range from a few to $\sim$50 lipids. These inter lipid interactions are stable, some of them persisting over the whole trajectory for analysis ($70 - 150$ ns). Consequently, also the ion-lipid clusters are rather stable implying that the lipids involved in a cluster form entities that act in a concerted fashion. It is likely that this plays a role in the structural as well as the dynamical properties of the bilayer, including, e.g., the movement of lipids in the plane of the bilayer, and the possible formation of small-scale domains of PG-ion rich regions in many-component membranes.

Further, the strength and stability of positively charged ions and negatively charged headgroups provide a possible molecular level explanation for the action of PGs in bacterial membranes under the influence of organic solvents. These highly polar interactions create a high free energy barrier for hydrophobic molecules such as benzene, thus it may give one reason as to why nature uses charged lipids in these structures that have to adjust quickly to external changes.

PG headgroups also strongly modify the orientation of water near the bilayer. Two peaks of opposite sign in the interfacial region of the POPG bilayer related to the local water dipole order were observed (Fig. 4.25a). Correlation of the position of these peaks with the position of the two peaks of opposite sign on the charge density (Fig. 4.25b) along the bilayer normal suggests that the ordering of water molecules originates from shielding of local charges by water dipoles.

The snapshot of a Na^+ ion coordinated with PG oxygen atoms and water molecules which is additionally hydrogen bonded with a phosphate oxygen (Fig. 4.21a) illustrates well the origin of the first peak. The second peak is due to water molecules hydrogen bonded with phosphate and glycerol oxygen atoms from the side of the water phase. In the case of PCs, water is ordered by the phosphate groups in a manner similar to PGs but the positively charged choline group does not act in the same way as a PG (which has no positive charge around) and the Na^+ ions around the choline group create a clathrate like structure. Thus the lack of ordering relative to the bilayer normal.

The long-range polarization of the water molecules throughout the simulation box suggests that the amount of interlayer water in our model is too low for comparisons with unilamellar vesicles. That means that there is an additional repulsive interaction through the water phase between headgroups of opposite layers which potentially can influence the structure and dynamics of simulated bilayers. This is in agreement with experimental studies of charged lipids which show continuous swelling with water added between lamellae up to a certain threshold at which two phases are formed, a fully hydrated unilamellar vesicle with bulk water [203]. However, the exact amount of inter-lamellar water for POPG is not known. Despite that, we can exclude the possibility that the increase of the order and decrease of the surface area observed in our studies are additionally facilitated by a too small number of inter-bilayer water molecules. Similar increase for the order of PG acyl chains was observed in mixed PE-PG bilayers [170] and PG monolayers [175], and thus it is unlikely that it can influence our conclusions.

In the next section, a POPE/POPG mixture bilayer, which serves as a model of bacterial membranes, will be discussed in detail. After that, properties of water within membrane/water interface in different bilayer systems will be studied in the last section.

4.5 Model membrane for bacteria

4.5.1 Introduction

In addition to the much studied PCs, PEs and PGs are among the most common lipids in nature. PEs are present in both eukaryotic and procaryotic membranes participating in a multitude of tasks such as determining fusion, vesiculation and curvature of bilayers [204–207]. PEs also influence permeation [208], and even processes such as cell division [209].

As mentioned in the previous section, PGs, as well as other charged lipids, function both as membrane stabilizers and destabilizers [172] controlling membrane peptide/protein interactions. Furthermore, bacteria are able to adjust the relative concentrations of PEs and PGs when subjected to toxic organic solvents [210, 211]. Such an alteration in headgroup composition seems to be a means to change membrane permeability, and to preserve stability. Molecular mechanisms responsible for these changes are not known, however.

Here we studied a mixed POPE/POPG bilayer in proportion 3:1. This proportion was chosen as it models bacterial membranes [167, 212]. Our results suggest that the stability of bacterial membranes significantly increases due to the presence of PGs. PGs also decrease protrusions of PE molecules and reduce their motion along the bilayer normal. These changes occur due to strong ion-mediated electrostatic interactions, and an increase in inter-lipid hydrogen bonds.

The rest of this section is organized as follows: we first describe the system preparation and simulation conditions; then we present the results, and we finish with discussion and summary.

4.5.2 System preparation

A lipid bilayer consisting of 96 POPEs, 32 POPGs, and 3623 water molecules was prepared based on a pre-equilibrated POPC bilayer [156]. 32 Na^+ counterions were added for charge neutrality. A pure POPE bilayer made of 128 POPEs and 3655 waters was studied as a reference system. The temperature of the POPE/POPG system is kept at 310 K. The resulting POPE/POPG (POPE) bilayer system was simulated for 100 (150) ns; the time range from 30 to 100 (30 to 150) ns was used in data analysis.

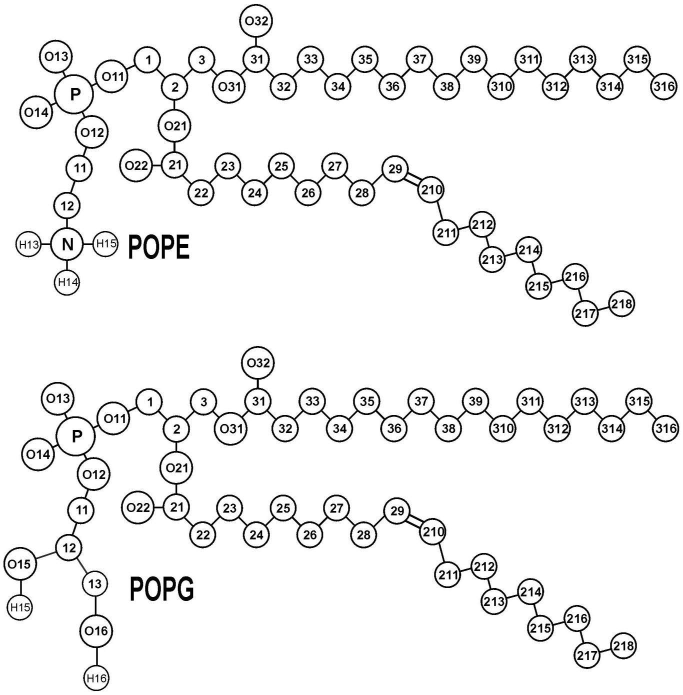

Figure 4.27: Chemical structures and the labeling of atoms of POPE and POPG lipids.

4.5.3 Simulation results

Headgroup orientation and rotation

'The orientations of the P-N vectors of PE (from now on, PE refers to POPE and PG refers POPG) lipids are influenced by the Na$^+$ ions which bind to the carbonyl oxygen O22 in the POPE/POPG system. To demonstrate this, PEs were divided into two categories: those bound to a sodium and those not. We define a PE $-$ Na$^+$ pair bond if the lifetime of the 'bond' exceeds half of the whole trajectory. We found that about 1/3 of PEs were bound during the simulation run. The average angle between the bilayer normal and the P-N vectors of bonded PEs was 87 ± 4^{o} and 96 ± 2 for non-bonded, i.e., binding to an ion reorients the P-N vector toward the water phase. The orientation of the P-N vectors in the pure PE system was found, within error bars, to be the same as in the PE/PG system. That may be the result of the balance between ion bonding and hydration of the POPE headgroups since we found that the coordination number of water around the PE nitrogen was 1.34 in the PE/PG system, and 1.69 in the pure PE bilayer. In comparison, the effects of Na$^+$ ions on the orientation of the PG headgroup are negligible.

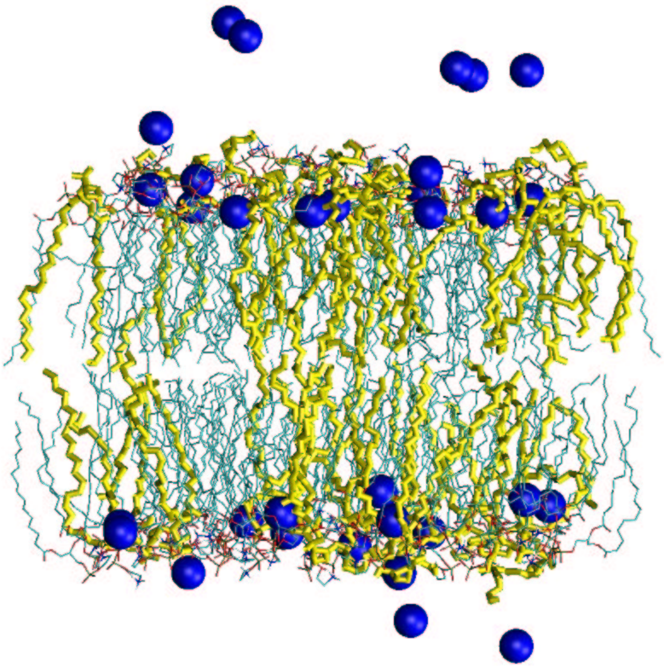

Figure 4.28: Snapshot of the structure of the POPE/POPG bilayer. The POPG lipids are shown in yellow, Na^+ ions in blue, and water is not shown for clarity.

To examine the effect of ion bonding on headgroup rotation, we calculated the reorientational autocorrelation function (RAF) of the P-N vectors of the ion-bonded and nonbonded PE headgroups both in the mixed PE/PG and the pure PE bilayers. As can be seen in Fig. 4.29, the rotation of PE headgroups is slower in the mixed bilayer including both bonded and nonbonded PEs. However, the dynamics of the bonded headgroups is more influenced than those of nonbonded. We can conclude that headgroup rotation is influenced both by ion bonding and hydrogen bonds.

Interactions with ions

In the PE/PG system, Na^+ ions interact actively with the carbonyl oxygen atoms, especially with the PG ones.

According to coordination number analysis shown in Tab. 4.3, Na^+ ions clearly prefer to interact with the PG carbonyl oxygen atoms since the ratio between PE and PG is 3 : 1 and there is no big difference between their coordination numbers around Na^+ ions. The hydroxyl oxygen O15 (PG)

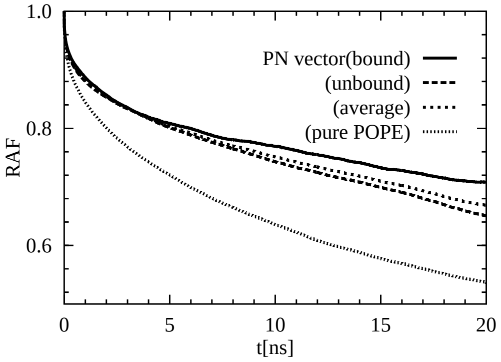

Figure 4.29: Rotational autocorrelation function of the first Legendre polynomial for the P-N vectors in the PE lipids in the PE and PE/PG bilayers.

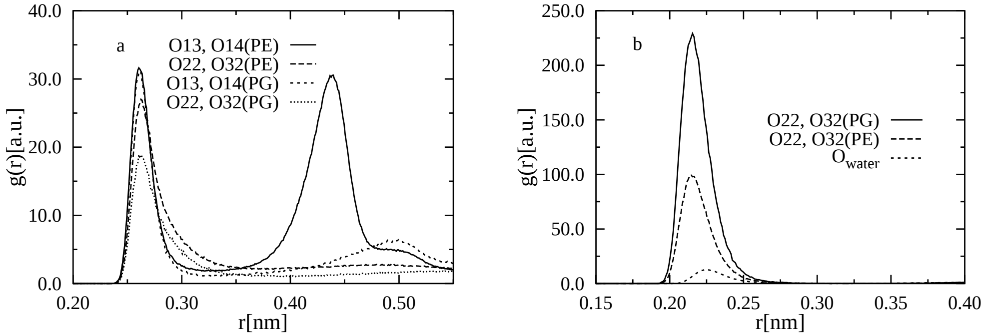

Figure 4.30: (a) Radial distribution functions (RDF) of phosphodiester and carbonyl oxygen atoms of PE and PG with (a) PE nitrogen atoms and (b) Na^+ ions in the PE/PG system. The second peak of O13, O14 (PE) around PE nitrogen, shown in (a), is the intra-molecular contribution.

Oxygen type	N_c around Na^+
O22, O32 (PE)	1.1
O22, O32 (PG)	0.80
O13, O14 (PE)	0.06
O13, O14 (PG)	0.01
O15 (PG)	0.11
O16 (PG)	0.03
O_{water}	3.28

Table 4.3: Coordination number of different types of oxygen atoms around Na^+ ions. O_{water} denotes water oxygen atoms.

interacts more with Na^+ ions than the hydroxyl oxygen O16 (PG), which could be due to their deeper location. This is also observed in pure PG system. Also, two carbonyl oxygen atoms of both PE and PG show different occurrence around Na^+ ions. The coordination numbers of O22 and O32 of PE around a Na^+ ion are found to be 0.70 and 0.39. For PG, the relative coordination numbers are 0.58 and 0.22.

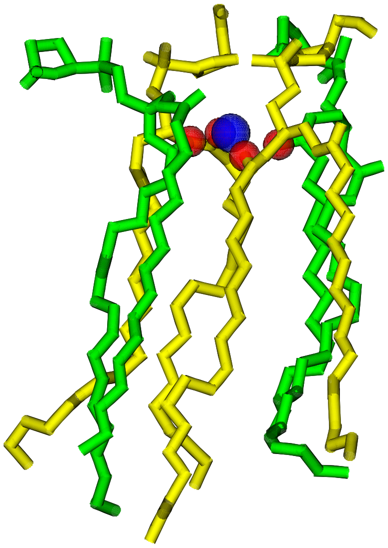

Figure 4.31: A snapshot of four lipids bonding to a Na^+ ion. PE lipids are shown in green and PG lipids are shown in yellow. The Na^+ ion is shown in blue and its bonded carbonyl oxygen atoms are shown in red.

Ions can link two lipids together by forming 'bridges'. We define an ion bridge to exist when a carbonyl oxygen (O22, O32) is within the first

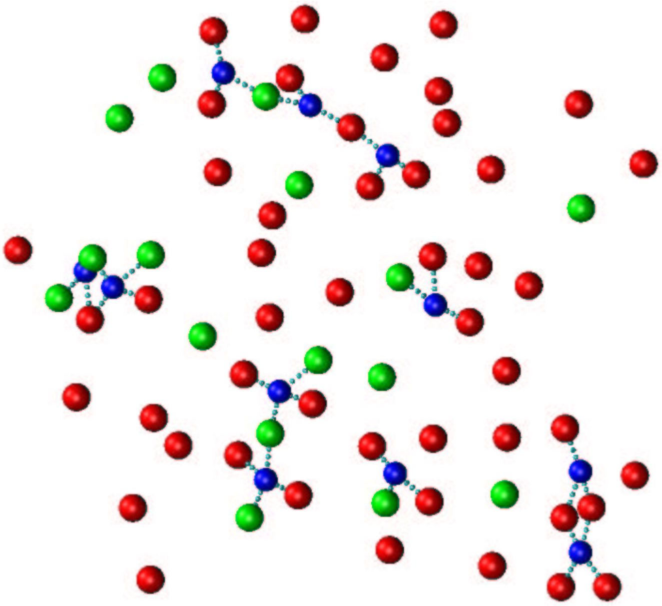

Figure 4.32: Configuration of the upper leaflet after 100 ns. Each lipid is represented by the average position of its two carbonyl oxygen atoms. The ion-lipid bonds are represented by green dots. Color scheme: red: PEs, green: PGs, blue: Na^+ ions.

hydration shell (0.33 nm) of a Na^+ ion. We chose this definition since the bonding between Na^+ ions and carbonyl oxygen atoms is more stable and frequent compared to interactions between Na+ ions and other lipid oxygen atoms. It is also possible to consider all lipid oxygen atoms as binding sites available for ion bridges [200]. We found 60 ± 6 ion-lipid pairs, which lead to the formation of 13 ± 1 ion-lipid clusters. A snapshot of a cluster (viewed from the water side) is shown in Fig. 4.32. As compared to PE, there are more PGs which bond to two Na^+ ions. Majority of Na^+ is found to interact with three or four lipids. A snapshot of four lipids bonded to one Na^+ is shown in Fig. 4.31.

In conclusion, the introduction of PGs and related counterions to a PE bilayer gives rise to strong bonding and formation of stable ion-lipid clusters, this will be discussed in detail below.

Lipid-lipid and lipid-water hydrogen bonding

On average, a PE lipid was found to participate in 1.27 hydrogen bonds (0.79 with other PE and 0.48 with PG) in mixed PE/PG bilayer and only in 0.95 in pure PE bilayer (see Tabs. 4.4 and 4.5). Also, a PG lipid participates in

1.55 hydrogen bonds (1.44 with PE and 0.11 with PG)

Lipids also hydrogen bond with water molecules. PE carbonyl oxygen atoms (O22 and O32) hydrogen bond 1.35 water molecules in mixed PE/PG bilayer and 1.78 in pure PE bilayer, thus in this region of bilayer we observed dehydration likely due to ion bonding. PG bond in carbonyl region 0.97 water molecules in mixed bilayer and 0.63 in pure PG bilayers. Other oxygen atoms of lipids bound similar number of water in mixed and pure bilayers.

H donor	H acceptor	Inter-molecular	Intra-molecular
N (PE)	O12 (PE)	-	1.00 ± 0.00
N (PE)	O13, O14 (PE)	0.49 ± 0.04	-
N (PE)	O22 (PE)	0.24 ± 0.03	0.13 ± 0.03
N (PE)	O32 (PE)	0.06 ± 0.02	0.03 ± 0.01
N (PE)	O13, O14 (PG)	0.16 ± 0.03	-
N (PE)	O15 (PE)	0.10 ± 0.02	-
N (PE)	O16 (PE)	0.03 ± 0.02	-
N (PE)	O22 (PE)	0.08 ± 0.01	-
N (PE)	O32 (PE)	0.03 ± 0.01	-
O15 (PG)	O12 (PG)	-	1.00 ± 0.00
O16 (PG)	O11 (PG)	-	0.02 ± 0.02
O16 (PG)	O12 (PG)	-	-
O16 (PG)	O13, O14 (PG)	0.01± 0.01	-
O16 (PG)	O15 (PG)	0.01 ± 0.01	0.04 ± 0.03
O16 (PG)	O16 (PG)	0.01± 0.01	-
O16 (PG)	O21 (PG)	-	0.03 ± 0.01
O16 (PG)	O22 (PG)	0.06± 0.03	0.01± 0.01
O16 (PG)	O31 (PG)	-	-
O16 (PG)	O32 (PG)	0.02 ± 0.02	0.01± 0.01
O16 (PG)	O13, O14 (PE)	0.03 ± 0.03	-
O16 (PG)	O22 (PE)	0.16 ± 0.05	-
O16 (PG)	O32 (PE)	0.05 ±0.04	-

Table 4.4: Average number of inter-molecular and intra-molecular hydrogen bonds in a PG lipid. The errors given are standard deviation estimates. See Fig. 4.27 for atom labeling.

In conclusion, the introduction of PGs and related counterions to a PE bilayer leads to an increase in inter-molecular hydrogen bonding (34% more hydrogen bonds per PE) and to a decrease in hydration in the carbonyl region of the bilayer. This may also have other consequences as the area per lipid

H donor	H acceptor	Inter-molecular	Intra-molecular
N (PE)	O13, O14 (PE)	0.63 ± 0.05	-
N (PE)	O22 (PE)	0.26 ± 0.03	0.18 ± 0.03
N (PE)	O32 (PE)	0.07 ± 0.02	0.01 ± 0.01

Table 4.5: Average number of inter-molecular and intra-molecular hydrogen bonds in a PG lipid. The errors given are standard deviation estimates. See Fig. 4.27 for atom labeling.

of a mixed PC/PG bilayer has been shown to depend on hydration (together with the mixing ratio) [213].

Protrusions characterized by PE glycerol backbone

The distribution of the nitrogen atoms in the two systems is shown in Fig. 4.33a. It has a slightly narrower distribution in the mixed bilayer as compared with the pure PE bilayer. This suggests that the protrusions in the mixed bilayer are suppressed as compared with the pure bilayer. Figure 4.33b shows the autocorrelation functions for the positions of the glycerol groups along the bilayer normal with respect to their neighborhood, where we can observe a slower motion in the direction of the bilayer normal in the mixed bilayer.

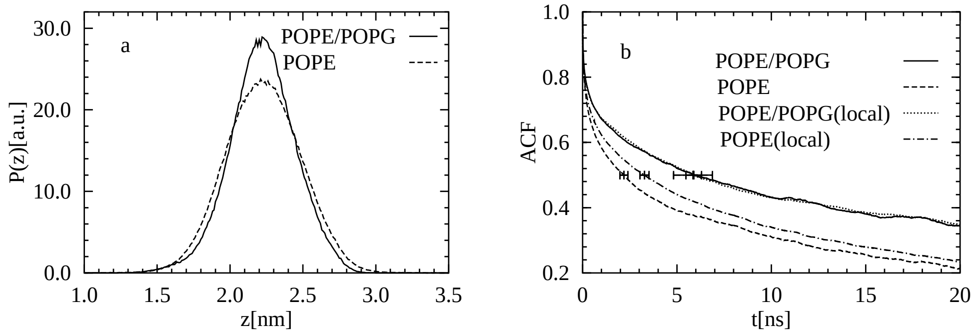

Figure 4.33: (a) Partial densities of the nitrogen atoms (bilayer is centered at 0 nm). (b) Autocorrelation functions of the vertical positions of the glycerol group for the pure PE and mixed PE/PG bilayers. The neighborhood was defined as molecules with their centers of mass at a distance ≤1 nm. The z-position was then calculated with respect to the average z-position of the neighborhood.

4.5.4 Discussion and summary

We have studied the properties of POPE/POPG bilayers to elucidate the role of charged PG lipids on the stability of bacterial membranes. Key results of this study are shown in Figs. 4.33a and 4.33b. The distribution of nitrogen atoms is sharper in the mixed bilayer than in the pure PE system (Fig. 4.33a); that indicates a more compact bilayer interfacial region and less lipid protrusions into the water phase. Decrease in protrusions is associated with slower dynamics in the interface as shown in Fig. 4.29 and 4.33b. Both phenomena contribute to increased membrane stability by preventing lipid desorption from the membrane, for example, under the influence of an organic solvent, thus preventing the membrane from disintegrating. A more compact and less dynamic structure of the interface should also decrease membrane permeability. To our knowledge such a mechanism of stabilizing bacterial membranes by PG has not been previously proposed.

Our data suggests that the atomic level mechanism responsible for the decrease of protrusions and the dynamics of headgroups is related to the strong bonding between PEs and PGs. This is realized through hydrogen bonds and ion bridges. As for hydrogen bonds, the PE ammonium group preferentially hydrogen bonds with the PG phosphodiester oxygen atoms. Due to this, the total number of hydrogen bonds created by the ammonium groups is increased by about 30% in comparison with the pure POPE bilayer. Additionally, PEs are hydrogen bonded with POPGs via the PG hydroxyl groups. Similar hydrogen bonding and water mediated bonding (water bridges) between PE and PG has been shown in a previous study of a POPE/POPG bilayer [212].

The second mechanism responsible for the decrease of protrusions is due to ion binding and the formation of ion bridges between PEs and PGs. Figure 4.28 shows that most of the ions are bonded in the interface. That causes local dehydration as water bridges are replaced by much stronger ion links. The lifetime of ion links is much longer than that of water bridges (of the order of 100-200 ps). Many ions were bonded for more than half of the simulation time, some of them even for the whole simulation (70 ns).

In the next section, we will discuss the dynamics of water molecules within different bilayer systems.

4.6 Structural and dynamical properties of water near membranes

4.6.1 Introduction

Water is a key element in determining and controlling a variety of structural and functional properties of biological membranes [214]. For example, the very formation of membrane bilayers depends on water. Water also regulates and mediates membrane-membrane and membrane-protein interactions. Due to this, water-membrane interactions have been a subject of intense research. Milhaud, and Pratt and Pohorille provide recent reviews [215, 216].

It is firmly established that biological macromolecules and assemblies modify the properties of the neighboring water molecules [217]. Similarly, any hydrophilic surface, such as a membrane or a micelle, affects properties such as rotational, translational and vibrational motions of water [218]. Studies on PC bilayers at low and full hydration suggest that translational motion of water near the membrane surface is restricted [219, 220]. The self-diffusion coefficient of water in the first hydration layer has been reported to be as much as 5 times smaller than in bulk [221].

As discussed in Chapter 2, the network of hydrogen bonds in interfacial region is perturbed and the probability of water molecules hydrogen bonding with neighboring molecules is increased, but due to a decrease in the number of neighbors, the total number of hydrogen bonds actually decreases. In the interfacial region water is also hydrogen bonded with lipid headgroups; lifetime of such bonding is much longer than that of water-water hydrogen bonds [88]. Water dipoles also become ordered in the interfacial region up to 1 nm away from the membrane surface [85].

Water dynamics at the membrane surface has been a subject of few molecular dynamics simulation studies. In previous MD simulation studies on water dynamics near POPC membrane surface, it was shown that translational and rotational motions of water on 100 ps time scale near the membrane surface are restricted [222]. The effect was the strongest for water molecules that were hydrogen bonded to the phosphate and carbonyl oxygen atoms as well as those clathrating choline groups of POPC. Both the translational and rotational motions of water that was hydrogen bonded to carbonyl oxygen were slower than the motions of those bonded to phosphate oxygen. It was also observed that water clathrating the POPC choline group was less affected than phosphate and carbonyl hydrogen bonded water, and that translational diffusion of all membrane water was faster along the membrane plane than along the membrane normal.

In another study Åman *et al.* showed that bonded water in the interfacial region may be described by two regions characterized by different structure and dynamics [223]. It was shown that the slow component of the reorientational correlation function of bonded water molecule is due to exchange between free and bonded water. This component was not observed over long (i.e., nanosecond) time scales. Bhide and Berkowitz performed comparative studies on water dynamics on neutral PCs and negatively charged PSs [224]. Sega *et al.* analyzed diffusion of intralamellar water in a ganglioside bilayer, i.e., in a confined geometry, and clearly demonstrated the importance of boundary effects [225].

In this work, we have investigated the dynamic behavior of water molecules within bilayer systems composed of two lipids, PE and PG, in comparison with a PC bilayer system. Our studies show, somewhat unexpectedly, that the three different headgroups (PE, PG and PC) modify water dynamics in the interfacial region in a similar way despite the fact that the strongly hydrogen bonding amine group of PE and the glycerol group of PG slow down bonded water much more than the choline group of PC. The weaker effect in the case of PC is compensated by the much higher number of water molecules bonded in the clathrate-like structure around this group (about 11) rather than hydrogen bonded with amine and glycerol groups ($1-2$ molecules).

Next, we will give a brief introduction to the system preparation and methods for analysis. Then we will present the simulation results and complete this section with discussion and summary.

4.6.2 System preparation

MD simulations of three different lipid bilayers, consisting of 128 POPC, POPE, and POPG lipids, were performed. All three bilayers were hydrated with about 3600 water molecules. A pure water system consisting of 1000 water molecules (no lipids) was used as a reference system. The initial configurations of these three bilayer systems were taken from pre-equilibrated systems studied in Sec. 4.4 and Sec. 4.5. The simulations were performed for 1 ns storing data at very short intervals (details below). Those fragments are analyzed in this article to capture the details of interfacial water with high sampling resolution in equilibrium.

4.6.3 Data analysis

To calculate the mean square displacement and the reorientational autocorrelation function the last 1 ns of each trajectory was sampled at every 50 fs. This 1 ns was further divided into five 200 ps fragments - the results presented

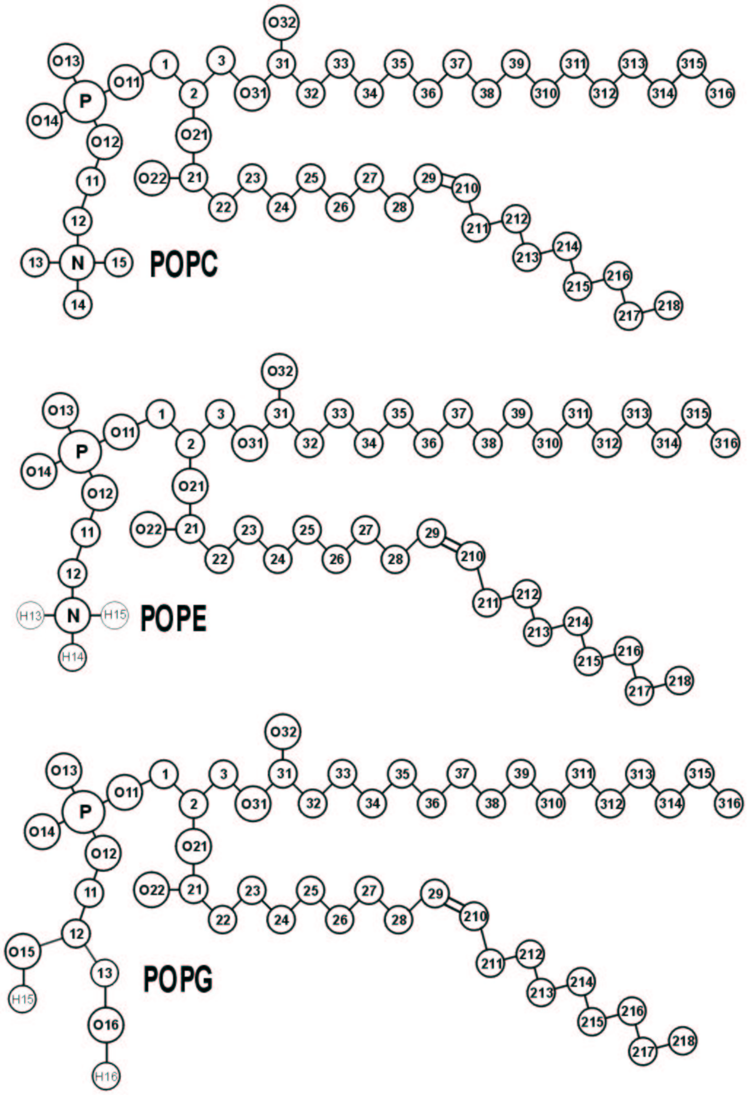

Figure 4.34: Chemical structures and the labeling of atoms of POPC, POPE, and POPG lipids used in this study.

below are averaged over these 200 ps fragments. To calculate the velocity autocorrelation functions and the angular velocity autocorrelation functions, 100 ps fragments of each trajectory were sampled at every 2 fs. The data analysis was performed with the Molecular Modeling Tool Kit library and the nMoldyn program [226, 227].

To study the effect of membrane surface on the dynamics of water, the water molecules were classified into six groups following the convention used in a previous study [222]. The first group consisted of water molecules that were not further than 0.4 nm from any membrane atom. We call these water molecules neighboring water. The number of water molecules in this group was approximately 1000. The second group consisted of water molecules within a layer between 0.4 and 1.2 nm from any membrane atom (called intermediate water) and consisted typically of 1000 – 1800 water molecules, and the third group was made up of water molecules that were not closer than 0.7 nm from any membrane atom (far water). That group had about 500 water molecules in the POPC bilayer and about 1000 in the other bilayers.

Using the above criteria it is possible for a water molecule to belong to both intermediate and far water. The overlap was about 30%. It is also worth noticing that the thickness of the water shell is lower in the POPC bilayer due to much larger area per lipid. This results in a smaller size of the far water group and larger overlap between this group and intermediate water. The next three groups consisted, respectively, of water molecules that were hydrogen bonded to phosphate oxygen atoms (OP water), carbonyl oxygen atoms (OC water), the amine group of POPE (AM water), the glycerol group of POPG (GL water), and those clathrating choline groups of POPC (CHOLINE water). A hydrogen bond between an OH group of a water molecule and an oxygen or a nitrogen atom of PC is judged to be formed when the O – O distance r is 0.325 nm and the angle between the O – O vector and the OH bond (the O – O H angle) is 35 °. The distance 0.325 nm is the position of the first minimum in the radial distribution function (RDF) of the water oxygen atoms (OW) relative to an oxygen atom of a PC [228]. A water molecule clathrating a choline group is defined when a water molecule oxygen atom is within 0.475 nm from the N-CH3 group. The distance 0.475 nm is the position of the first minimum of the RDF of the OWs relative to a N-CH_3 group [228]. Other groups consisted of a smaller number of molecules: AM, GL, OC water of 50 – 100 molecules, OP of 150 molecules, and CHOLINE of 800 water molecules.

A water molecule was determined to belong to one of the above groups if it fulfilled the given criteria for at least 70% of the analyzed time (200 ps selection was performed independently for each trajectory fragments). The criterion of 70% was used because of dynamics of hydrogen bonding during

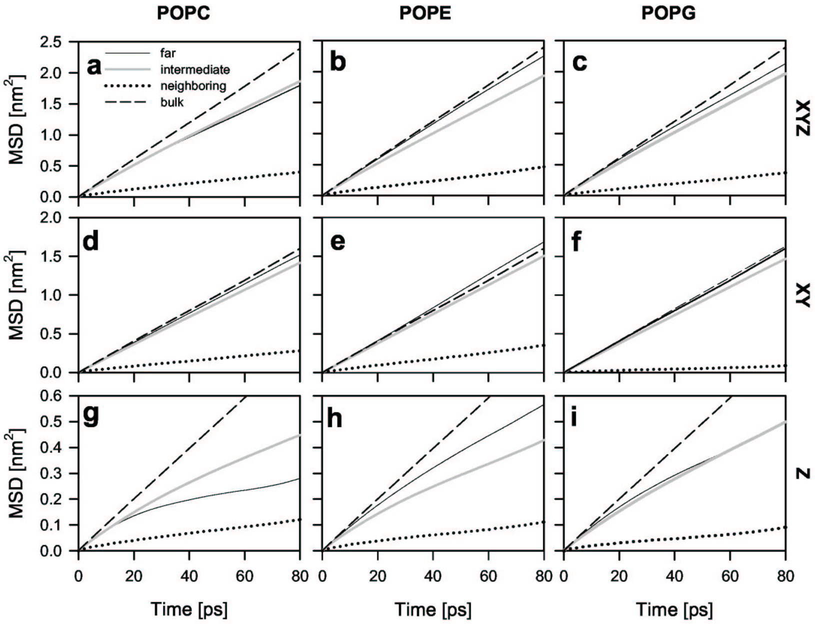

Figure 4.35: Mean-square displacement (MSD) of the neighboring water (dotted line), intermediate water (gray line), far water (solid line), and bulk water (dashed line) in PC (a, d, g), PE (b, e, h), and in PG (c, f, i). In the membrane (a, b, c), in the membrane plane (d, e, f), and along the bilayer normal (g, h, i).

a hydrogen bond lifetime. Short bonding and nonbonding intervals are observed thus using stronger criterion would lead to an unnaturally small group not reflecting actual bonding.

4.6.4 Simulation results

Translational motion

Figures 4.35 and 4.36 show the mean square displacement (MSD) curves of water molecules belonging to selected groups. The diffusion coefficients were obtained by fitting to the linear part of MSD curves between 20 and 80 ps (Table 1).

As observed in experiments [219] as well as in previous MD simulation studies [222–224], translational diffusion of neighboring water is significantly slower than that of far water. This is observed both along the membrane plane and along the bilayer normal. Similar effects are observed for all three bilayers. However, the reduction in translational diffusion seems to be greater

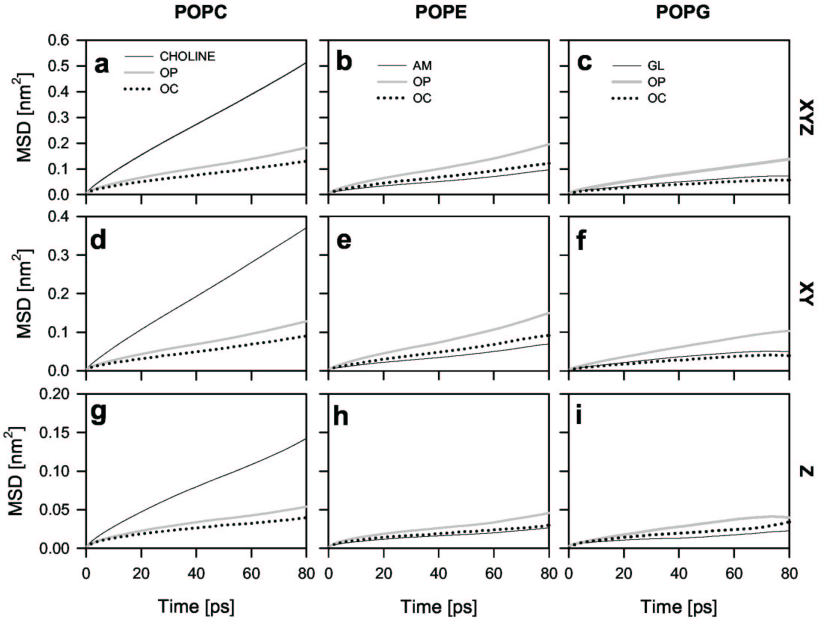

Figure 4.36: Mean-square displacement (MSD) of the OC water (dotted line), OP water (gray line), choline/AM/GL water (solid line), in PC (a, d, g), PE (b, e, h), and PG (c, f, i). In the membrane (a, b, c), in the membrane plane (d, e, f), and along the bilayer normal (g, h, i).

in the case of the PE (from now on, PC, PE and PG refer to POPC, POPE, POPG, respectively) and PG than in the case of the PC bilayer. The influence of membrane surface is also apparent for intermediate water for PC and PE bilayers - the effects in these bilayers are the opposite. In the case of the PC bilayer, the diffusion of intermediate water along the bilayer normal is faster than of far water while in the PE bilayer it is slower. In PG bilayer we do not observe differences in the rate of translational diffusion between intermediate and far water. The translational diffusion of far water is slightly slower than that of bulk water, due to the reduction of translational diffusion along the membrane normal, while diffusion in the membrane plane is, within error, equal to the diffusion of bulk water.

As shown in Fig 4.36, the choline group has the weakest effect on water translational diffusion. In all bilayers OC water is more affected than OP water. Amine and glycerol groups modified water translational diffusing to the same degree as carbonyl groups.

Table 4.6 summarizes the results for translational diffusion. Anisotropy in translational diffusion is apparent: it is slower along the membrane normal than in the membrane plane. Diffusion in bulk water is isotropic, as expected. Our results support the analysis of Sega *et al.* and Liu *et al.* but we could not determine whether the in-plane and out-of-plane dynamics are completely decoupled [225, 229].

Rotational motion

In Figs. 4.37 and 4.38 reorientational correlation function (RCF) curves of water molecules belonging to the selected groups in PC, PE and PG bilayers are shown. RCF was calculated according to the algorithm given in Ref. [227] for a coefficient set 1, 0, 0. This set of coefficients represents rotational motions measured by optical spectroscopy [230]. The RCF curves could not be satisfactorily fitted to a sum of exponentials, and thus the results are only qualitative.

As shown in Fig. 4.37, we observed that rotation is strongly affected by vicinity of the membrane surface in all bilayers. Small effect is also observed for intermediated water in case of the PG bilayer. This result is in agreement with the observation that in PG bilayers water dipoles remain ordered for a long distance away from the interface (see Sec. 4.4) The choline group had the weakest effect on water rotation while the carbonyl groups had the strongest. The amine and glycerol groups had a stronger effect than the phosphate groups.

The RCF curves of water molecules belonging to selected groups are compared in Fig. 4.38. We do not observe differences between near and interme-

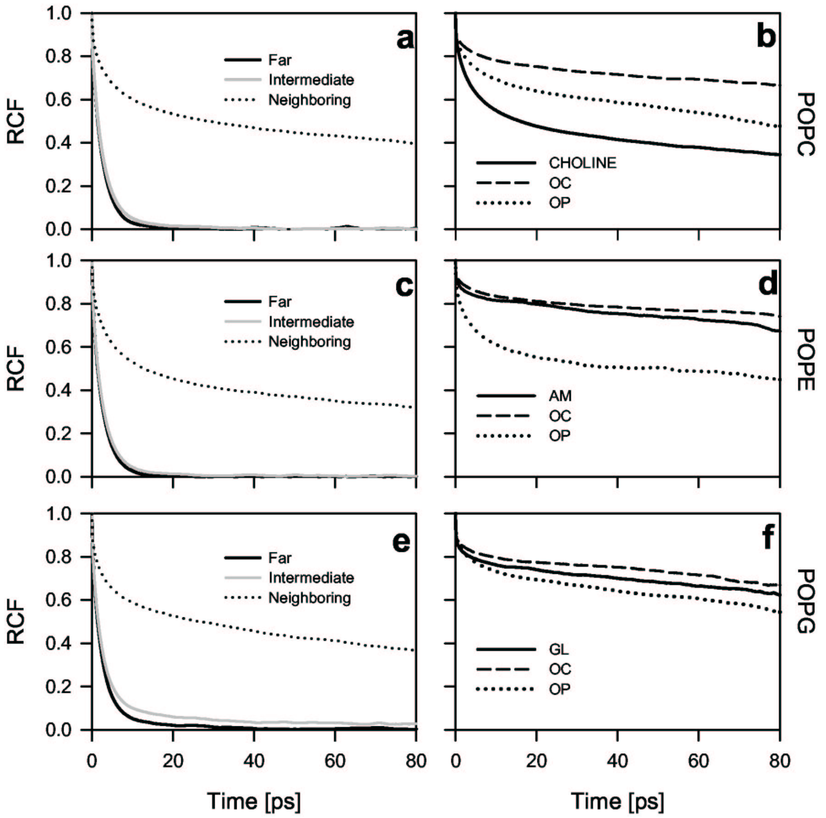

Figure 4.37: Reorientational correlation function (RCF) of the neighboring water (dotted line), intermediate water (gray line), and far water (black line) (a, c, e); choline/AM/GL water (solid line), OP water (dotted line), and OC water (dashed line) (b, d, f). In PC (a, b), PE (c, d), and PG (e, f) bilayers.

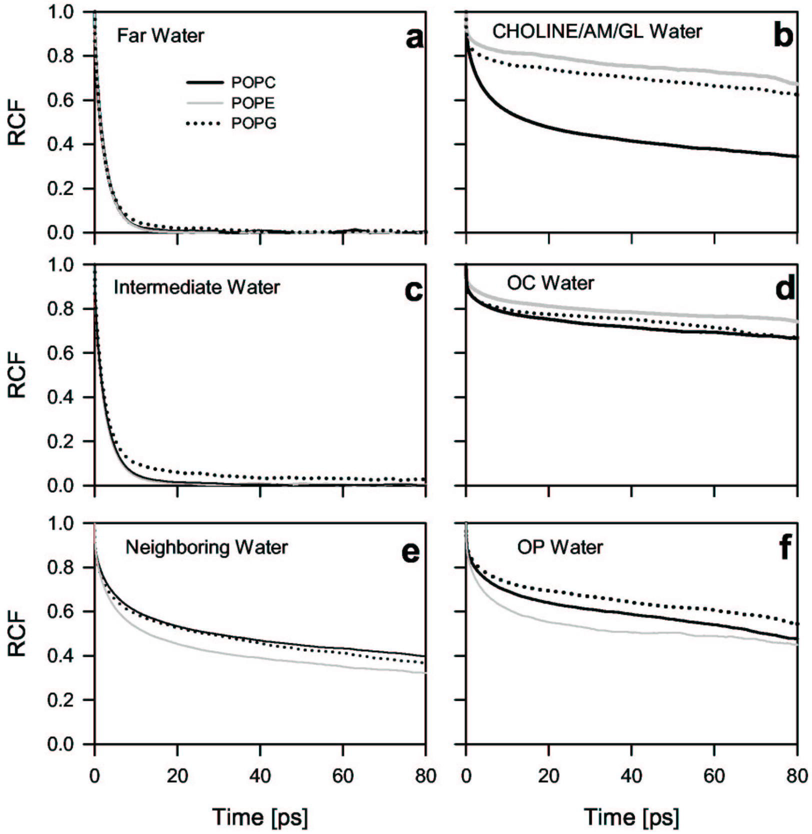

Figure 4.38: Reorientational correlation function (RCF) of the far water (a), intermediate water (c), neighboring water (e), choline/AM/GL water (b), OC water (d), and OP water (f) in the PC (solid line), PE (gray line), and PG (dotted line) bilayers.

System	Group	D_1	$D_\perp$	$D_{\|\|}$
Water box	-	0.50 ± 0.02	0.50 ± 0.02	0.50 ± 0.02
PC	Far	0.36 ± 0.02	0.47 ± 0.03	0.12 ± 0.02
	Intermediate	0.36 ± 0.02	0.44 ± 0.02	0.24 ± 0.01
	Neighboring	0.08 ± 0.01	0.08 ± 0.01	0.07 ± 0.01
	Choline	0.10 ± 0.01	0.11 ± 0.01	0.08 ± 0.01
	OP	0.035 ± 0.005	0.035 ± 0.005	0.030 ± 0.005
	OC	0.02 ± 0.005	0.025 ± 0.005	0.017 ± 0.005
PE	Far	0.47 ± 0.02	0.53 ± 0.02	0.33 ± 0.03
	Intermediate	0.40 ± 0.02	0.47 ± 0.02	0.24 ± 0.02
	Neighboring	0.09 ± 0.01	0.11 ± 0.02	0.06 ± 0.01
	AM	0.02 ± 0.01	0.02 ± 0.01	0.01 ± 0.01
	OP	0.04 ± 0.01	0.05 ± 0.01	0.02 ± 0.01
	OC	0.02 ± 0.01	0.03 ± 0.01	0.01 ± 0.01
PG	Far	0.44 ± 0.02	0.51 ± 0.02	0.27 ± 0.02
	Intermediate	0.40 ± 0.03	0.46 ± 0.02	0.28 ± 0.02
	Neighboring	0.08 ± 0.01	0.08 ± 0.02	0.06 ± 0.01
	GL	0.01 ± 0.01	0.02 ± 0.01	0.01 ± 0.01
	OP	0.03 ± 0.01	0.03 ± 0.01	0.02 ± 0.01
	OC	0.008 ± 0.002	0.009 ± 0.003	0.006 ± 0.002

Table 4.6: Self-diffusion coefficients in three dimensions (D_1), in the membrane plane ($D_\perp$), and along the membrane normal ($D_{||}$) obtained from fitting to the MSD curves of water molecules belonging to the selected groups. Unit: [10^{-8}cm^2/s].

diate water for the PC and PE bilayers, while for the PG bilayer rotation is slightly affected. For neighboring water, rotation is similar in the PC and PG bilayers, while in PE bilayer it is less affected.

Velocity autocorrelation functions

Figure 4.39 shows the velocity autocorrelation function (VACF) of water molecules belonging to the selected groups in PC, PE and PG bilayers. In Fig. 4.39a VACF for neighboring, intermediate and far water in PC bilayer are shown. As can be seen intermediate, far and bulk water are indistinguishable. Similar results were obtained for PE and PG bilayer. Thus in further analysis we concentrate only on neighboring water.

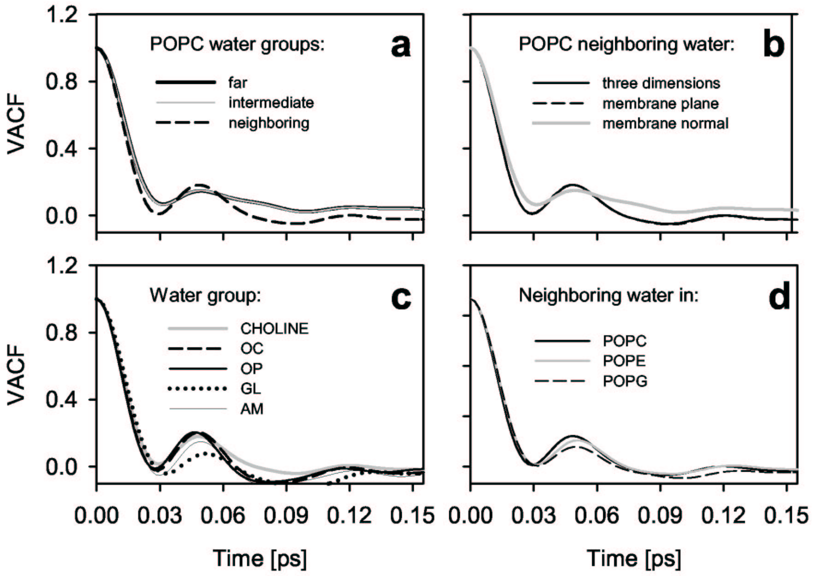

Figure 4.39: Velocity-autocorrelation function (VACF) of neighboring (dashed line), intermediate (gray line), and far (solid line) water in the PC bilayer (a); neighboring water in three dimensions (solid line), in the membrane plane (dashed line) and along the bilayer normal (gray line) in the PC bilayer (b); OC (dashed line), OP (thick line), and choline (gray line) water in the PC bilayer; AM (thin line) water in the PE bilayer, and GL water in the the PG bilayer (dotted line) (c); neighboring water in the PC (solid line), PE (gray line) and PG (dashed line) bilayers (d).

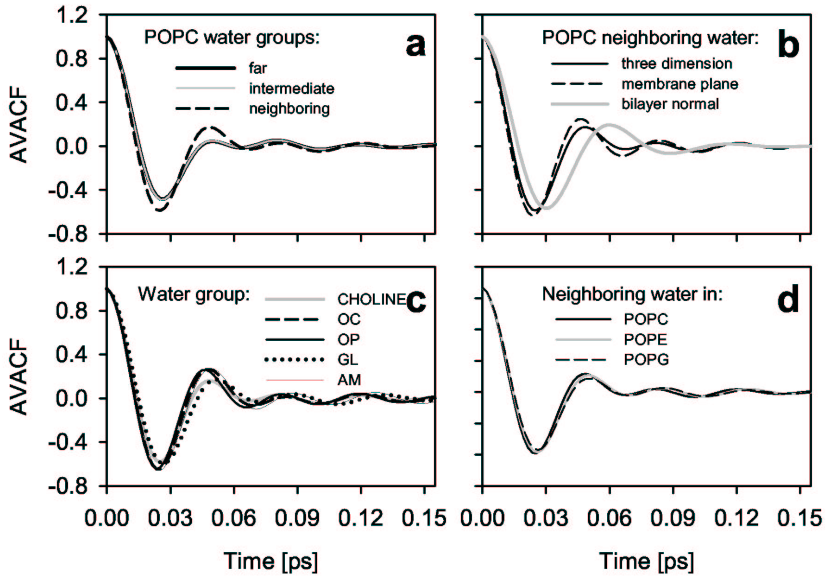

Figure 4.40: Angular velocity-autocorrelation function (AVACF) of neighboring (dashed line), intermediate (gray line), and far (solid line) water in the PC bilayer (a); neighboring water in three dimensions (solid line), in the membrane plane (dotted line), and along the bilayer normal (gray line) in the PC bilayer (b); OC (dashed line), OP (thick line), CHOLINE (gray line) water in the PC bilayer. AM (thin line) water in the PE bilayer, and GL water in the PG bilayer (dotted line) (c); neighboring water in the PC (solid line), PE (gray line), and PG (dashed line) bilayers (d).

Angular velocity autocorrelation functions

Figure 4.40 shows the angular velocity autocorrelation function (AVACF) of water molecules belonging to the selected groups in PC, PE and PG bilayers. In Fig. 4.40a AVACF for neighboring, intermediate and far water in PC bilayer are shown. As can be seen intermediate, far and bulk water are almost indistinguishable. Similar results were obtained for PE and PG bilayers, and thus in further analysis we concentrate only on neighboring water. Comparison of AVACF of neighboring water in PC bilayer in three dimensions, along the bilayer normal and in the bilayer plane is shown in Fig. 4.40b. The correlations in angular motions persist longer along the bilayer normal than in the bilayer plane. Similar results were obtained for PE and PG bilayers. Comparison of water bound to the various polar groups of lipids show similar behavior of AVACF (Fig. 4.40c). The results are very similar in all three bilayer systems as are the results for near water in different bilayers (Fig. 4.40d).

4.6.5 Discussion and conclusion

In this study we have analyzed interface effects of three different lipid bilayers - POPC, POPE and POPG on water dynamics. Using a simple criterion, we selected three groups of water: neighboring water, intermediate water and far water. In agreement with our previous studies, we observed a strong effect on neighboring water dynamics in all three bilayers. Interestingly, we did not observe any pronounced effects due to the headgroup structure on the translational diffusion of neighboring water (see Tab. 4.6), and only a small effect on the rotational motion (in PE bilayer neighboring water rotation is less restricted than in PC and PG bilayers).

The above results are surprising when we compare how the lipid groups interact with water molecules. The choline group of PC affects water rotation less effectively than the equivalent amine group in PE and the glycerol group in PG molecules, thus we should expect a stronger effect of PE and PG headgroups on water dynamics compared to PC. The reason for these ambiguous results is the differing number of water molecules involved in interactions with different groups. Choline group binds about 11 water molecules in clathrate while amine and glycerol groups binds $1-2$ water molecules. In case of PG bilayer, a presence of counterions strongly adsorbed at the bilayer interface (see Sec. 4.4) slows down water dynamics in the interfacial region comparing to the PE bilayers.

Bhide and Berkowitz used an alternative definition for water molecules on the basis of the water density profile corrected for the membrane roughness

[224]. They selected three regions of water: region 1 water in carbonyl groups region, region 2 water in phosphatidylcholine or phosphatidylserine group region, and region 3 far water. They observed that the translational motions in region 1 were slowed down by a factor of 100 and in region 2 by a factor of 6 in the case of a DPPC bilayer. Results obtained for region 2 correspond to choline water (slowed down by factor 3.6) and OP water (slowed down by the factor 10) in our case; these groups are equivalent to region 2 of Ref. [224]. Slowing down observed for region 1 was higher than for our OC group (slowed down by a factor of 25) likely because our definition potentially includes water molecules from region 2, and does not include water molecules not hydrogen bonded with PC but buried in the membrane core, which can obviously affect the results significantly. Another alternative approach to the selection of water groups was presented by Åman and co-workers [223]. They based their selection on the profile of the water order parameter along the bilayer normal. In spite of different selection procedures both studies showed qualitatively similar effects on the translational motion of water.

In a previous study [222], an analysis of water dynamics in POPC bilayers was performed using the same water-group definition and simulation conditions, but different force fields for water (TIP3P water model [105]) and lipids (OPLS forcefield [231]). Using the current parameter set (which is commonly used by other research groups as well), translational diffusion slowed down much more than in the previous study. This is a consequence of the stronger effects of the phosphate, carbonyl, and choline groups, as well as the higher number of water molecules in clathrate around the choline group (11 water molecules in the present parameterization and six in the previous one per PC molecule). Both effects seem to result from higher partial charges in the choline methyl groups (for partial charges, see Ref. [116]) and stronger van der Waals interactions between water and lipid atoms (for this point see Ref. [232]). These stronger interactions also influence water dynamics in the intermediate and far water groups, which are slower than in bulk water. The difference between bulk and far water was less pronounced in the previous parameterization.

As a conclusion, we found that hydrogen bonding amine group of PE and the glycerol group of PG slows water motion more than the equivalent choline group of PC. Nevertheless, the overall effect of membrane surface vicinity is similar in all three bilayers. This is possibly due to the much higher number of water molecules interacting with the choline group than hydrogen bonded with glycerol or amine group.

Chapter 5

Conclusions

The theme of this thesis is computer simulations of charged membrane/water systems using the classical molecular dynamics method. It is known that electrostatics plays a crucial role in biomembranes. For example, conformation, folding, and biological function of membrane proteins are sensitively dependent on the overall or local electrostatic membrane properties [77]. In addition, charged membrane systems are widely applied in various industrial fields. For example, the DOTAP lipid is the most widely used cationic lipid in designing cationic liposomes for gene delivery systems [149]. Therefore, it is of great importance to understand the structural and electrostatic properties of charged membrane systems. In this thesis, we mainly studied two representative kinds of charged bilayer membrane systems: cationic and anionic bilayer systems. According to the content of specific research focus, this thesis can be divided into four separate case studies, as summarized below.

In the first part, we focused on cationic DMPC/DOTAP lipid bilayer systems at different fraction of cationic DOTAP lipid. This is the first molecular dynamics study of cationic mixture bilayers composed of neutral and cationic lipids of different chain length and saturation. In this study, we investigated the average as well as the dynamic behavior of the electrostatic interactions within the membrane/water interface, along with analysis of both the global and local dimensions of the bilayers. Along with comparisons to previous MD and theoretical studies, we revealed that the compositions of the hydrocarbon chains have an effect on the interfacial electrostatics.

In the second part, we studied a pure anionic POPG bilayer in the presence of positively charged counterions. The key observation in this study is that the majority of counterions penetrate into the carbonyl region of the bilayers and together with the lipids form a great number of ion-lipid bonds. This is different from the previous case study, in which the membrane surface and the counterions form a diffuse double layer structure. Due to the existence of these ion-lipid bonds, POPG lipids link to each other via ion-bridges which constrain the dynamic behavior of the lipids. This leads to a smaller area per lipid of the pure POPG lipid bilayer despite the mutual electrostatic repulsion between the like-charged lipids.

Third, based on the second part, we studied an anionic POPE/POPG mixture bilayer which serves as a model of the inner plasma membrane of bacteria. In this study, we mainly focused the electrostatic interactions such hydrogen bonding and interactions between ions and lipids. We found that hydrogen bonds contribute considerably to the interfacial properties of the POPE/POPG bilayer. Another important observation is the formation of ion-lipid bridges and lipid clusters, which have not been reported before. We propose this as a possible mechanism of how bacteria may be able to control their permeability against organic solvents.

The fourth project is the study of the dynamic behavior of water molecules at different lipid bilayer surfaces. In this work, we analyzed the interface effects of three different lipid bilayers-POPC, POPE, and POPG on water dynamics. The effects on water dynamics by different part of headgroups in lipid bilayers are analyzed in details. We found that the hydrogen bonding between the lipid headgroups and water molecules greatly affects the dynamic behavior of the interfacial water. To our surprise, the effect of a POPC bilayer surface on water dynamics is found to be similar to that of POPE and POPG bilayers. We suggest that this is due to the much higher hydration level (more interacting water molecules) of POPC at choline groups region compared to the with amine or glycerol groups of POPE and POPG.

In conclusion, we have performed molecular modeling of charged membrane systems. Our aim has been to understand better the structural and dynamic phenomena in these systems at microscopic length scales. Our results suggest also some possible directions for future studies, as already mentioned in connection of each study case. For example, the dependence of elastic properties on the constituents of charged membranes is an interesting subject since the phase behavior of biosystems involving charged membranes depends on their elastic properties [69]. Also, coarse-graining of charged membranes is an interesting and challenging field, which, to best of the author's knowledge, has not been done in published literature. Finally, our results suggest that the behavior of membrane systems is very sensitive to the choices of force field parameters. However, polarization effects have not been included in most of the current force fields for biomolecules and ions. This could be a task to be performed in the future.

Appendix A

Legendre Transform

The basic idea of the *Legendre transform* can be considered as a process of variable transform which can be illustrated as below.

Consider a convex function $f(x)$ in 2D and its derivative:

$$y = f'(x) = \frac{df}{dx} \equiv g(x), \tag{A.1}$$

where defines a variable transform from x to y. However, one can not describe function $f(x)$ in terms of the variable y alone. As shown in Fig. A.1, for a given point x_0, one can not determine the value of the function $f(x_0)$ given only $f'(x_0)$, since the function $f(x_0) + c$ for any constant c will have the same value of $f'(x_0)$.

However, the value $f'(x_0)$ can be determined uniquely if we define the slope of the tangent to $f(x)$ at x_0, i.e., $f'(x_0)$ and the f-intercept $b(x_0)$ of this tangent. Then at x_0, we have

$$f(x_0) = x_0 f'(x_0) + b(x_0). \tag{A.2}$$

Extend this relation to all the points on $f(x)$, one obtain:

$$f(x) = x f'(x) + b(x). \tag{A.3}$$

Note that $y = f'(x)$, and $x = g^{-1}(y)$, where g^{-1} is the functional inverse of g. Solving for $b(x) = b(g^{-1}(y))$ gives:

$$b\left(g^{-1}(y)\right) = f\left(g^{-1}(y)\right) - y g^{-1}(y) \equiv \phi(y), \tag{A.4}$$

where $\phi(y)$ is said to be the *Legendre transform* of $f(x)$.

Equation A.4, defining the Legendre transform from $f(x)$ to $\phi(y)$, is usually written as:

$$\phi(y) = f(x) - xy. \tag{A.5}$$

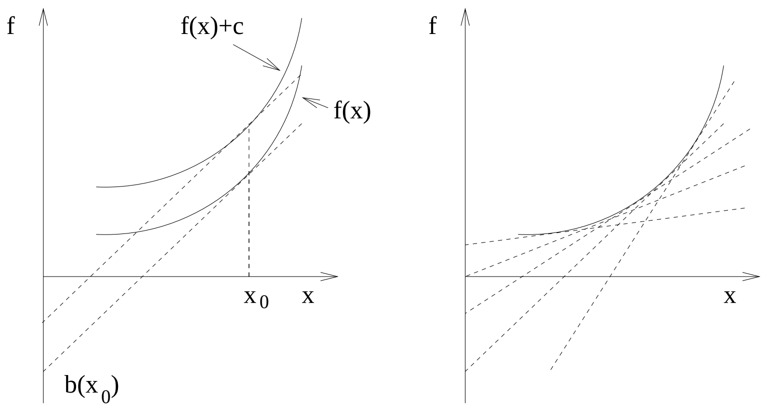

Figure A.1: Schematic illustration of Legendre transform in two-dimension space.

For a strictly convex function, the Legendre transform can be interpreted as a mapping between the graph of the function and the collection of tangents of the graph, as shown in Fig. A.1.

In thermodynamics, the fundamental equation for the internal energy U may include a number of terms related to different types of work and involves only differentials of extensive variables. In addition to the terms from the combined first and second laws for system involving PV work, the internal energy may include terms for chemical work, work of electric transport, elongation work, surface work, etc. For these complex situation, the fundamental equations for the other thermodynamic potentials can be obtained using the Legendre transforms that define these other thermodynamic potentials in terms of U minus conjugate pairs of intensive and extensive variables. Through the Legendre transform, one can study the thermodynamics of the specific ensemble at different thermodynamic states that involving desired set of thermodynamic variables.

Appendix B

The mean and Gaussian curvatures of a smooth surface

As shown in Fig. B.1, a two-dimensional surface in three-dimensional space can be locally be characterized by its two principal curvatures [233]

$$c_1 = \frac{1}{R_1}, \tag{B.1}$$

$$c_2 = \frac{1}{R_2} \tag{B.2}$$

where R_1, R_2 are the curvature radii of the intersections of the surface with two mutually perpendicular planes containing the normal to the surface.

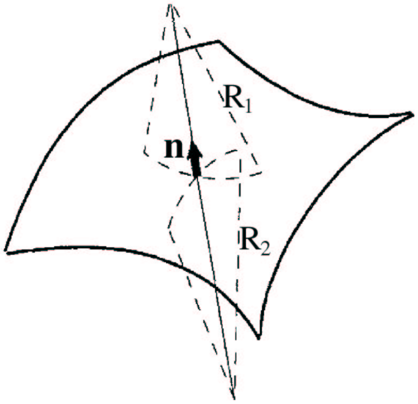

Figure B.1: Local curvature on a two-dimensional surface. The length scales R_1 and R_2 denote the radii of the local curvature The figure is made based on a structure in Ref. [86]

Then the mean curvature H and the Gaussian curvature K are given by

$$H = c_1 + c_2, \tag{B.3}$$

$$K = c_1 c_2. \tag{B.4}$$

The curvatures H and K have simple geometrical interpretations [59]. Consider a small portion S of the surface, and let A be its area. Construct now a new surface $S^{'}$ by moving each point of S by some distance δ along the normal in the direction of positive h. The new surface will have the area

$$\triangle A^{'} = \triangle A \, (1 + \delta H + \delta^2 K + o(\delta^2)). \tag{B.5}$$

In the spontaneous curvature model, Eq. B.5 was employed in deriving the elastic free energy of membrane surface [59].

Bibliography

[1] D. L. Nelson and M. M. Cox, in *Lehninger Principles of Biochemistry*, 4 ed. (W. H. Freeman, New York, 2004).

[2] D. L. Nelson and M. M. Cox, in *Lehninger Principles of Biochemistry*, 3 ed. (Worth Publishers, New York, 2000).

[3] S. J. Singer and G. L. Nicolson, Science **175**, 720 (1972).

[4] D. J. Cram and J. M. Cram, Science **183**, 803 (1974).

[5] J. I. Schroeder, K. Raschke, and E. Neher, Proc. Natl. Acad. Sci. **84**, 4108 (1987).

[6] R. Mackinnon and C. Miller, J. Gen. Physiol. **91**, 335 (1988).

[7] R. Mackinnon *et al.*, Science **280**, 106 (1998).

[8] B. M. Denker, B. L. Smith, F. P. Kuhajda, and P. Agre, J. Biol. Chem. **263**, 15634 (1988).

[9] K. Murata *et al.*, Nature **407**, 599 (2000).

[10] P. D. Boyer, Bioscience Reports **18**, 97 (1998).

[11] S. Maruyama, T. Hata, H. Matsuki, and S. Kaneshina, Biochim. Biophys. Acta **1325**, 272 (1997).

[12] R. B. Gennis, in *Biomembranes-Molecular Structure and Function* (Springer-Verlag, New York, 1989).

[13] R. A. Lerner, Proc. Natl. Acad. Sci. **94**, 13375 (1997).

[14] S. A. Susin *et al.*, Nature **397**, 441 (1999).

[15] R. Hooke, *Micrographia, or, Some physiological descriptions of minute bodies made by magnifying glasses* (John Martyn and James Allestry, London, 1665).

[16] D. Brandon, Proc. Natl. Acad. Sci. **55**, 1048 (1966).

[17] D. Brandon, Phil. Trans. Roy. Soc. London B **261**, 133 (1971).

[18] J. D. Robertson, J. Biophys. Biochem. Cytol. **3**, 1043 (1957).

[19] L. D. Frye and M. Edidin, J. Cell Sci. **7**, 319 (1970).

[20] K. Jacobson, E. D. Sheets, and R. Simson, Science **268**, 1441 (1995).

[21] M. Edidin, M. C. Zuniga, and M. P. Sheetz, Proc. Natl. Acad. Sci. **91**, 3378 (1994).

[22] S. Damjanovich *et al.*, Proc. Natl. Acad. Sci. **92**, 1122 (1995).

[23] J. Hwang, A. L. Gheber, L. Margolis, and M. Edidin, Biophys. J **74**, 2184 (1998).

[24] K. Simons and W. L. C. Vaz, Ann. Rev. Biophys. Biomol. Struct. **33**, 269 (2004).

[25] G. Vereb *et al.*, Proc. Natl. Acad. Sci. **100**, 8053 (2003).

[26] J. Israelachvili, *Intermolecular and surface forces*, 2nd ed. ed. (Academic Press, San Diego, CA, 1991).

[27] A. Blume, in *Phospholipid Handbook* (Marcel Dekker, New York, 1993), Chap. Dynamics properties.

[28] in *Phospholipid Handbook*, edited by G. Cevc and J. M. Sedden (Marcel Dekker, New York, 1993), pp. 351–454.

[29] B. Alberts *et al.*, *Molecular biology of the cell* (Garland Science, New York, 2002).

[30] A. Kõiv and P. K. J. Kinnunen, Chem. Phys. Lipids **72**, 77 (1994).

[31] B. F. Cravatt *et al.*, Science **268**, 1506 (1995).

[32] M. Edidin, Ann. Rev. Biophys. Biomolec. Structure **32**, 257 (2003).

[33] Y. A. Hannun, Science **275**, 1855 (1996).

[34] T. Lian and R. J. Y. Ho, J. Pharm. Sci. **90**, 667 (2001).

[35] N. P. Patel, J. M. Zielinski, J. Samseth, and R. J. Spontak, Macro. Chem. Phys. **205**, 2409 (2004).

[36] J. O. Rädler, I. Koltover, T. Salditt, and C. R. Safinya, Science **275**, 810 (1997).

[37] A. S. Ulrich, Bioscience Reports **22**, 129 (2002).

[38] J. O. Rädler, I. Koltover, T. Salditt, and C. R. Safinya, Science **275**, 810 (1997).

[39] P.-G. de Gennes, Physica A **274**, 1 (1999).

[40] K. Ewert *et al.*, Curr. Med. Chem. **11**, 133 (2004).

[41] G. H. Mickisch, World J. Urol. **13**, 178 (1995).

[42] T. Schlick, *Molecular Modeling and Simulation* (Springer, New York, 2002).

[43] B. Alder and T. Wainwright, J. Chem. Phys. **27**, 1208 (1957).

[44] I. Vattulainen and M. Karttunen, in *Handbook of Theoretical and Computational Nanotechnology*, edited by M. Rieth and W. Schommers (American Scientific Publishers, Stevenson Ranch, CA, 2006), Chap. 29.

[45] D. Frenkel and B. Smit, *Understanding molecular simulation: From algorithms to applications, 2nd edition* (Academic Press, San Diego, 2002).

[46] A. R. Leach, *Molecular Modeling: Principles and Applications* (Longman, Harlow, UK, 1996).

[47] W. Shinoda, N. Namiki, and S. Okazaki, J. Chem. Phys. **106**, 5731 (1997).

[48] K. Kremer and F. Müller-Plathe, Mater. Res. Bull. **26**, 169 (2001).

[49] L. Saiz and M. L. Klein, Accounts of Chemical Research **35**, 482 (2002).

[50] S. J. Marrink, A. H. de Vries, and A. E. Mark, J. Phys. Chem. B **108**, 750 (2004).

[51] K. Huang, *Statistical Mechanics*, 2nd ed. (John Wiley & Sons Inc., New York, 1987).

[52] R. K. Pathria, *Statistical Mechanics*, *International Series in Natural Philosophy* (Pergamon, Oxford, UK, 1985).

[53] J. Katsaras, Biophys. J **75**, 2157 (1998).

[54] M. J. Janiak, D. M. Small, and G. G. Shipley, J. Biol. Chem. **254**, 6068 (1979).

[55] B. D. Ladbrooke and D. Chapman, Chem. Phys. Lipids **3**, 304 (1969).

[56] G. S. Smith, E. B. Sirota, C. R. Safinya, and N. A. Clark, Phys. Rev. Lett. **60**, 813 (1988).

[57] J. Katsaras and V. A. Raghunathan, in *Lipid bilayers, structure and interactions*, edited by J. Katsaras and T. Gutberlet (Springer, Berlin, 2000), Chap. Aligned lipid-water systems.

[58] F. David and S. Leibler, J. Phys. II France **1**, 959 (1991).

[59] L. Peliti, in *Fluctuating Geometries in Statistical Mechanics and Field Theory*, edited by F. David, P. Ginsparg, and J. Zinn-Justin (Elsevier, Amsterdam, 1994).

[60] R. Lipowsky, Nature **349**, 475 (1991).

[61] E. Evans and W. Rawicz, Phys. Rev. Lett. **64**, 2094 (1990).

[62] P. B. Canham, J. Theor. Biol. **26**, 61 (1970).

[63] W. Helfrich, Z. Naturforschung C. **28**, 693 (1973).

[64] L. Miao, U. Seifert, M. Wortis, and H. G. Dobereiner, Phys. Rev. E **49**, 5389 (1994).

[65] F. L. H. Brown, Technical report, Department of Chemistry and Biochemistry, UCSB (unpublished).

[66] F. Brochard and J. F. Lennon, J. Phys. France **36**, 1035 (1975).

[67] W. Helfrich, J. Phys. France **46**, 1263 (1985).

[68] L. Peliti and L. Leibler, Phys. Rev. Lett. **54**, 1690 (1985).

[69] S. May, J. Chem. Phys. **105**, 8314 (1996).

[70] A. Imparato, J. C. Shillcock, and R. Lipowsky, Europhys. Lett. **69**, 650 (2005).

[71] P.-G. de Gennes and C. Taupin, J. Phys. Chem. **86**, 2294 (1982).

[72] J. A. Reynolds, D. B. Gilbert, and C. Tanford, Proc. Natl. Acad. Sci. USA **71**, 2925 (1974).

[73] R. Lipowsky and S. Grotehans, Europhys. Lett. **23**, 599 (1993).

[74] G. Gompper, D. M. Kroll, and R. Lipowsky, Phys. Rev. B **42**, 961 (1990).

[75] E. Lindahl, Ph.D. thesis, Royal Institute of Technology, 2001.

[76] S. W. Hui *et al.*, Biophys. J **71**, 590 (1996).

[77] G. Cevc, Biochim. Biophys. Acta **1031**, 311 (1990).

[78] L. Pauling, J. Am. Chem. Soc. **53**, 1367 (1931).

[79] D. Chandler, Nature **437**, 640 (2005).

[80] M. Pasenkiewicz-Gierula *et al.*, Biophys. J. **76**, 1228 (1999).

[81] D. Andelman, in *Handbook of Biological Physics*, edited by R. Lipowsky and E. Sackmann (Elsevier Science B.V., Amsterdam, 1995), Vol. 1, Chap. 12, pp. 602–642.

[82] H. Wennerström and E. Sparr, Pure Appl. Chem. **75**, 905 (2003).

[83] S. Marcelja and N. Radic, Chem. Phys. Lett. **42**, 129 (1976).

[84] J. Israelachvili and H. Wennerström, J. Chem. Phys. **96**, 520 (1992).

[85] S. J. Marrink, M. Berkowitz, and H. J. C. Berendsen, Langmuir **9**, 3122 (1993).

[86] A. A. Gurtovenko, M. Patra, M. Karttunen, and I. Vattulainen, Biophys. J **86**, 3461 (2004).

[87] M. Gutman, E. Nachliel, and S. Moshiach, Biochemistry **28**, 2936 (1989).

[88] S. Balasubramanian, S. Pal, and B. Bagchi, Phys. Rev. Lett. **89**, 115505 (2002).

[89] M. P. Allen and D. J. Tildesley, *Computer Simulation of Liquids* (Clarendon Press, Oxford, 1987).

[90] R. Iftimie, P. Minary, and M. E. Tuckerman, Proc. Natl. Acad. Sci. **102**, 6654 (2005).

[91] A. Rahman, Phys. Rev. **136A**, 405 (1964).

[92] A. Rahman and F. H. Stillinger, J. Chem. Phys. **55**, 3336 (1971).

[93] J. McCammon, B. Gelin, and M. Karplus, Nature **267**, 585 (1977).

[94] D. H. Mackay, P. H. Berens, K. R. Wilson, and A. T. Hagler, Biophys. J **46**, 229 (1984).

[95] E. Egberts and H. J. C. Berendsen, J. Chem. Phys. **89**, 3718 (1988).

[96] T. B. Woolf and B. Roux, Proc. Natl. Acad. Sci. **91**, 11631 (1994).

[97] D. P. Tieleman and H. J. C. Berendsen, Biophys. J. **74**, 2786 (1998).

[98] E. Tajkhorshid *et al.*, Science **296**, 525 (2002).

[99] M. Ø. Jensen, E. Tajkhorshid, and K. Schulten, Biophys. J. **85**, 2884 (2003).

[100] S. Lifson and A. Warshel, J. Chem. Phys. **49**, 5116 (1968).

[101] A. T. Hagler, E. Huler, and S. Lifson, J. Am. Chem. Soc. **96**, 5319 (1977).

[102] C. J. Burnham and S. S. Xantheas, J. Chem. Phys. **116**, 1479 (2002).

[103] J. D. Bernal and R. H. Fowler, J. Chem. Phys. **1**, 515 (1933).

[104] B. Guillot, J. Mol. Liq. **101**, 219 (2002).

[105] W. L. Jorgensen *et al.*, J. Chem. Phys. **79**, 926 (1983).

[106] W. L. Jorgensen and J. D. Madura, Mol. Phys. **56**, 1381 (1983).

[107] M. W. Mahoney and W. L. Jorgensen, J. Chem. Phys. **112**, 8910 (2000).

[108] H. J. C. Berendsen, J. P. M. Postma, W. F. van Gunsteren, and J. Hermans, in *Intermolecular Forces*, edited by B. Pullman (Reidel, Dordrecht, 1981), pp. 331–342.

[109] H. J. C. Berendsen, J. R. Grigera, and T. P. Straatsma, J. Phys. Chem. **91**, 6269 (1987).

[110] I. M. Svishchev, P. G. Kusalik, J. Wang, and R. J. Boyd, J. Chem. Phys. **105**, 4742 (1996).

[111] U. Niesar *et al.*, J. Phys. Chem. **94**, 7949 (1990).

[112] A. D. MacKerell *et al.*, in *The Encyclopedia of Computational Chemistry*, edited by P. v. R. Schleyer et al. (John Wiley & Sons, Chichester, 1998), Chap. The Energy Function and Its Parameterization with an Overview of the Program, pp. 271–277.

[113] S. Y. Reddy, F. Leclerc, and M. Karplus, Biophys. J **84**, 1421 (2003).

[114] E. Lindahl, B. Hess, and D. van der Spoel, Journal of Molecular Modeling **7**, 306 (2001).

[115] D. P. Tieleman and H. J. C. Berendsen, J. Chem. Phys. **105**, 4871 (1996).

[116] O. Berger, O. Edholm, and F. Jahnig, Biophys. J. **72**, 2002 (1997).

[117] D. Case *et al.*, J. Comp. Chem. **26**, 1668 (2005).

[118] L. Verlet, Phys. Rev. **159**, 98 (1967).

[119] D. Beeman, J. Comp. Phys. **20**, 130 (1976).

[120] M. Tuckerman, B. J. Berne, and G. J. Martyna, J. Chem. Phys. **97**, 1990 (1992).

[121] L. S. Schulman, *Techniques and Applications of Path Integration* (John Wiley & Sons, Inc., New York, 1981).

[122] H. J. C. Berendsen, in *Computational Molecular Dynamics: Challenges, Methods*, Vol. 4 of *Lecture Notes in Computational Science and Engineering*, edited by P. D. hard *et al.* (Springer-Verlag, Amsterdam, 1998), pp. 3–36.

[123] H. J. C. Berendsen *et al.*, J. Chem. Phys. **81**, 3684 (1984).

[124] L. V. Woodcock, Chem. Phys. Lett. **10**, 257 (1971).

[125] H. C. Andersen, J. Chem. Phys **72**, 2384 (1980).

[126] J. A. Izaguirre, D. P. Catarello, J. M. Wozniak, and R. D. Skeel, J. Chem. Phys. **114**, 2090 (2001).

[127] P. Nikunen, M. Karttunen, and I. Vattulainen, Computer Phys. Comm. **153**, 407 (2003).

[128] C. P. Lowe, Europhys. Lett. **47**, 145 (1999).

[129] S. D. Bond, B. J. Leimkuhler, and B. B. Laird, J. Comp. Phys. **151**, 114 (1999).

[130] M. Parrinello and A. Rahman, J. Appl. Phys. **52**, 7182 (1981).

[131] B. Hess, H. Bekker, H. J. C. Berendsen, and J. G. E. M. Fraaije, J. Comp. Chem. **18**, 1463 (1997).

[132] J. P. Ryckaert, G.Ciccotti, and H. Berendsen, J. Comp. Phys. **23**, 327 (1977).

[133] S. Miyamoto and P. A. Kollman, J. Comp. Chem. **13**, 952 (1992).

[134] M. Patra *et al.*, J. Phys. Chem. B **108**, 4485 (2004).

[135] T. Darden, D. York, and L. Pedersen, J. Chem. Phys. **98**, 10089 (1993).

[136] U. Essman *et al.*, J. Chem. Phys. **103**, 8577 (1995).

[137] N. Karasawa and W. A. Goddard, J. Phys. Chem. **93**, 7320 (1989).

[138] R. W. Hockney and J. W. Eastwood, *Computer simulations using particles* (McGraw-Hill, New York, 1981).

[139] M. Deserno and C. Holm, J. Chem. Phys. **109**, 7678 (1998).

[140] M. Deserno and C. Holm, J. Chem. Phys. **109**, 7694 (1998).

[141] O. Berger, O. Edholm, and F. Jahnig, Biophys. J. **72**, 2002 (1997).

[142] J. P. Ryckaert and A. Bellemans, Chem. Phys. Lett. **30**, 123 (1975).

[143] J. P. Ryckaert and A. Bellemans, Chem. Phys. Lett. **66**, 95 (1978).

[144] J. F. Nagle and M. C. Wiener, Biochim. Biophys. Acta **942**, 1 (1988).

[145] S. W. Chiu *et al.*, Biophys. J. **69**, 1230 (1995).

[146] W. Shinoda and S. Okazaki, J. Chem. Phys. **109**, 1517 (1998).

[147] N. Zuidam and Y. Barenholz, Biochim. Biophys. Acta **1368**, 115 (1998).

[148] R. Zantl, F. Artzner, G. Rapp, and J. O. Rädler, Europhys. Lett. **45**, 90 (1998).

[149] D. Simberg, S. Weisman, Y. Talmon, and Y. Barenholz, Critical Review in Theropeutic Drug Carrier Systems **21**, 257 (2004).

[150] D. Felnerova, J.-F. Viret, R. Glück, and C. Moser, Curr. Opin. Biotech. **15**, 518 (2004).

[151] S. May, D. Harries, and A. Ben-Shaul, Biophys. J **78**, 1681 (2000).

[152] A. A. Gurtovenko, M. Patra, M. Karttunen, and I. Vattulainen, Biophys. J. **86**, 3461 (2004).

[153] A. A. Gurtovenko, M. Miettinen, M. Karttunen, and I. Vattulainen, J. Phys. Chem. B **109**, 21126 (2005).

[154] S. Bandyopadhyay, M. Tarek, and M. L. Klein, Phys. Chem. B **103**, 10075 (1999).

[155] S. Kitagawa, M. Kasamaki, and M. Hyodo, Chem. Pharm. Bull. **52**, 451 (2004).

[156] M. Patra *et al.*, Biophys. J **90**, 1121 (2006).

[157] J. F. Nagle and S. Tristram-Nagle, Biochim. Biophys. Acta **1469**, 159 (2000).

[158] H. I. Petrache, S. W. Dodd, and M. F. Brown, Biophys. J. **79**, 3172 (2000).

[159] N. Zuidam and Y. Barenholz, Biochim. Biophys. Acta **1329**, 211 (1997).

[160] R. Zantl *et al.*, J. Phys. Chem. B **103**, 10300 (1999).

[161] V. Levadny and C. Yamazaki, Langmuir **21**, 5677 (2005).

[162] L. Löbbcke and G. Cevc, Biochem. Biophys. Acta **1237**, 59 (1995).

[163] M. R. Gierula *et al.*, Biophys. J. **76**, 1228 (1999).

[164] S.-J. Marrink, D. P. Tieleman, A. R. van Buuren, and H. J. C. Berendsen, Faraday Discuss. **103**, 191 (1996).

[165] J. F. Mead, R. B. Alfin-Slater, D. R. Howton, and G. Popják, *Lipids - chemistry, biochemistry and nutrition* (Plenum Press, New York, 1986).

[166] W. Dowhan, Ann. Rev. Biochem **66**, 199 (1996).

[167] M. Pasenkiewicz-Gierula, K. Murzyn, T. Róg, and C. Czaplewski, Acta Biochim. Pol. **47**, 601 (2000).

[168] K. J. Hallock *et al.*, Biophys. J. **83**, 1004 (2002).

[169] S.-Y. Lee and R. MacKinnon, Nature **430**, 232 (2004).

[170] K. Murzyn, T. Róg, and M. Pasenkiewicz-Gierula, Biophys. J. **88**, 1091 (2005).

[171] S. Uran, A. Larsen, P. B. Jacobsen, and T. Skotland, J. Chrom. B **758**, 265 (2001).

[172] A. Tari and L. Huang, Biochemistry **28**, 7708 (1989).

[173] K. Maruyama, Biosci. Rep. **22**, 251 (2002).

[174] D. E. Elmore, FEBS Lett. **580**, 144 (2006).

[175] Y. N. Kaznessis, S. Kim, and R. G. Larson, Biophys. J. **82**, 1731 (2002).

[176] A. C. Cowley, N. L. Fuller, R. P. Rand, and V. A. Parsegian, Biochemistry **17**, 3163 (1978).

[177] B. Pozo-Navas *et al.*, Phys. Rev. Lett. **91**, 028101 (2003).

[178] B. Pozo-Navas *et al.*, Biochim. Biophys. Acta. **1716**, 40 (2004).

[179] T. Wiedmann, A. Salmon, and V. Wong, Biochim. Biophys. Acta **1167**, 14 (1993).

[180] R. Koynova, Chem. Phys. Lipids **89**, 67 (1997).

[181] R. Wohlgemuth, N. Waespe-Sarcevic, and J. Seelig, Biochemistry **19**, 3315 (1980).

[182] I. Pascher, M. Lundmark, P.-G. Nyholm, and S. Sundell, Biochim. Biophys. Acta **1113**, 339 (1992).

[183] P. Garidel and A. Blume, Eur. Biophys. J. **28**, 629 (2000).

[184] K. Lohner, A. Latal, G. Degovics, and P. Garidel, Chem. Phys. Lipids **111**, 177 (2001).

[185] I. Pascher, S. Sundell, K. Harlos, and H. Eibl, Biochem. Biophys. Acta **896**, 77 (1987).

[186] K. Murzyn and M. Pasenkiewicz-Gierula, Acta Biochim. Pol. **46**, 631 (1999).

[187] P. Mukhopadhyay, L. Monticelli, and D. P. Tieleman, Biophys. J. **86**, 1601 (2004).

[188] R. A. Böckmann, A. Hac, T. Heimburg, and H. Grubmüller, Biophys. J. **85**, 1647 (2003).

[189] R. A. Böckmann and H. Grubmüller, Angew. Chem. Int. Edn. **43**, 1021 (2004).

[190] A. A. Gurtovenko, J. Chem. Phys. **122**, 244902 (2005).

[191] S. W. Chiu, E. Jacobsson, R. J. Mashl, and H. L. Scott, Biophys. J. **83**, 1842 (2002).

[192] C. Hofsäß, E. Lindahl, and O. Edholm, Biophys. J. **84**, 2192 (2003).

[193] E. Falck *et al.*, Biophys. J. **87**, 1076 (2004).

[194] O. Edholm and J. F. Nagle, Biophys. J. **89**, 1827 (2005).

[195] A.-S. Andersson, R. A. Demel, L. Rilfors, and G. Lindblom, Biochim. Biophys. Acta **1369**, 94 (1998).

[196] R. S. Armen, O. D. Uitto, and S. E. Feller, Biophys. J. **75**, 734 (1998).

[197] M. Patra *et al.*, Biophys. J. **84**, 3636 (2003).

[198] A. Dicko, H. Bourque, and M. Pézolet, Chem. Phys. Lipids **96**, 125 (1998).

[199] P. Mukhopahyay, L. Monicelli, and D. Tieleman, Biophys. J. **86**, 1601 (2004).

[200] S. A. Pandit, D. Bostick, and M. L. Berkowitz, Biophys. J. **84**, 3743 (2003).

[201] J. J. L. Cascales, J. D. L. Torre, S. Marrink, and H. Berendsen, J. Chem. Phys. **104**, 2713 (1996).

[202] R. B. Gennis, *Biomembranes. Molecular Structure and Function*, *Springer Advanced Texts in Chemistry* (Springer, New York, NY, 1989).

[203] J. M. Boggs, Biochim. Biophys. Acta **906**, 353 (1987).

[204] R. Birner, M. Bürgermeister, R. Schneiter, and G. Daum, Mol. Biol. Cell **12**, 997 (2001).

[205] K. A. Dill and D. Stigter, Biochemistry **27**, 3446 (1988).

[206] H. Nikaido, Microbiol. Mol. Biol. Rev. **67**, 596 (2003).

[207] E. E. Williams, J. A. Cooper, W. Stillwell, and L. J. Jenski, Mol. Membr. Biol. **17**, 157 (2000).

[208] K. Iwamoto *et al.*, Genes to Cells **9**, 891 (2004).

[209] K. Emoto and M. Umeda, J. Cell Biol. **149**, 1215 (2000).

[210] S. Isken and J. A. M. de Bont, Extremophiles **2**, 229 (1998).

[211] F. J. Weber and J. A. M. de Bont, Biochim. Biophys. Acta **1286**, 225 (1996).

[212] K. Murzyn, T. Róg, and M. Gierula, Biophys. J. **88**, 1091 (2005).

[213] T. Wiedmann, A. Salmon, , and V. Wong, Biochim. Biophys. Acta **1167**, 14 (1993).

[214] R. M. Daniel, J. L. Finney, and M. Stoneham, Phil. Trans. R. Soc. Lond. B **359**, 1143 (2004).

[215] J. Milhaud, Biochim. Biophys. Act **1663**, 19 (2004).

[216] L. R. Pratt and A. Pohorille, Chem. Rev. **102**, 2671 (2002).

[217] B. Bagchi, Chem Rev. **105**, 3197 (2005).

[218] M.-C. Bellissent-Funel, J. Mol. Liq. **78**, 19 (1998).

[219] B. König *et al.*, J. Chem. Phys. **100**, 3307 (1994).

[220] U. Kaatze, A. Dittrich, K.-D. Göpel, and R. Pottel, Chem. Phys. Lipids **35**, 279 (1984).

[221] J. Fitter, R. E. Lechner, and N. A. Dencher, J. Phys. Chem. B **103**, 8036 (1999).

[222] T. Róg, K. Murzyn, and M. Pasenkiewicz-Gierula, Chem. Phys. Lett. **352**, 323 (2002).

[223] K. Åman *et al.*, Biophys. J **84**, 102 (2003).

[224] S. Y. Bhide and M. L. Berkowitz, J. Chem. Phys. **123**, 224702 (2005).

[225] M. Sega, R. Vallauri, and S. Melchionna, Phys. Rev. E **72**, 041201 (2005).

[226] K. Hinsen, J. Comp. Chem. **21**, 79 (2000).

[227] T. Róg, K. Murzyn, K. Hinsen, and G. Kneller, J. Comp. Chem. **24**, 657 (2003).

[228] K. Murzyn *et al.*, Biophys. J. **81**, 170 (2001).

[229] P. Liu, E. Harder, and B. Berne, J. Phys. Chem. B **108**, 6595 (2005).

[230] G. R. Kneller, V. Keiner, M. Kneller, and M. Schiller, Comp. Phys. Commun. **91**, 191 (1995).

[231] W. Jorgensen and J. Tirado-Rives, J. Am. Chem. Soc. **110**, 1657 (1988).

[232] C. Anézo *et al.*, J. Phys. Chem. B **107**, 9424 (2003).

[233] A. Gray, in *Modern Differential Geometry of Curves and Surfaces with Mathematica*, 2 ed. (CRC Press, Boca Raton, 1997), Chap. 17, pp. 398–401.